Measurement of the B-Meson Inclusive Semileptonic Branching Fraction and Electron-Energy Moments

A THESIS

PRESENTED TO THE FACULTY OF THE GRADUATE SCHOOL

OF THE UNIVERSITY OF MINNESOTA

BY

Christopher John Stepaniak

IN PARTIAL FULFILLMENT OF THE REQUIREMENTS

FOR THE DEGREE OF

DOCTOR OF PHILOSOPHY

Ronald A. Poling, Advisor

May 2004

© Christopher John Stepaniak 2004

ALL RIGHTS RESERVED

Measurement of the B-Meson Inclusive Semileptonic Branching Fraction and Electron-Energy Moments

by Christopher John Stepaniak

Under the supervision of Professor Ronald A. Poling

ABSTRACT

We report a new measurement of the B-meson semileptonic decay momentum spectrum that has been made with a sample of 9.4 fb^{-1} of e^+e^- data collected with the CLEO II detector at the $\Upsilon(4S)$ resonance. Electrons from primary semileptonic decays and secondary charm decays were separated by using charge and angular correlations in $\Upsilon(4S)$ events with a high-momentum lepton and an additional electron. We determined the semileptonic branching fraction to be $\mathcal{B}(B \to Xe^+\nu_e) = (10.91 \pm 0.09 \pm 0.24)\%$ from the normalization of the electron-energy spectrum. We also measured the moments of the electron energy spectrum with minimum energies from 0.6 GeV to 1.5 GeV.

To my parents, Richard and Teresa.

ACKNOWLEDGEMENTS

There are many people who have given me invaluable help and support getting through the past six years. I guarantee that I am going to forget someone who deserves mentioning; I apologize to them in advance.

I couldn't have asked for a better advisor than Ron Poling. The enthusiasm and curiosity with which he tackles problems are inspirational. He was always there to guide me back on the right path when I started wandering off into the wilderness during this analysis (no small task). His sense of humor and his patience were greatly appreciated during some of the rougher periods of my graduate career. It was a pleasure learning to do physics under his tutelage.

The rest of the folks in the Minnesota group were equally as enjoyable to work with. Alex Smith has been a great mentor and an even better friend. Working with him on the RICH gas system taught me much about hardware design and troubleshooting. From barbecues to concerts to just listening to me gripe, he's always been there when I needed support. Stefan Anderson was a great guide to both Ithaca and CLEO when I first arrived there, and continued to be a guiding influence through my thesis writing and job hunt, as well as a good friend. Tim Riehle showed the patience of a saint while teaching a computing neophyte the ropes of UNIX. Selina Li and Kaiyan Gao was always there to play ping-pong and talk about just about anything. Brian Lang, Justin Hietala, Tim Klein, and Alexander Scott provided many lively, stimulating,

and time-consuming discussions on nearly every topic under the sun.

The people I met in Ithaca deserve special thanks for keeping me sane. There are simply not enough people in the world like Gregg and Jana Thayer. Pete Zweber and Adie Gloor were always happy to have bonfires at their shack, step out for a beer, or head to the Sport's Club to watch the Vikings. I want to thank Pete, Gregg, Stefan, and Christine Crane for the numerous road trips and the stories that resulted from them; I also want to thank Adie and Jana for not killing us all after hearing some of those stories. I thank anyone who ever participated in a CLEO poker night or a night at the Chanticleer. And to Jean Dubosq, Alan Magerkurth, Mike Weinberger, Lauren Hsu, Tom Meyer, and Véronique Boisvert, thanks each of you for your part in making Ithaca bearable.

My friends in Minnesota have been a great source of fun and support. The trips to Ben Speakman's and Siri Rea's cabin are the stuff of legend. Emily Maher and Carolyn Erickson made my trips to the printer last much longer than they should. Kristin Brusegard has been a good friend through many many things. Cari McCollor was always there to keep life interesting.

And finally, I thank my family for their love and support over the twenty-five years of my education. My brother Nicholas probably understands me better than anyone out there, and never fails to make me laugh until I can't breathe. And I simply don't have the words to express the importance that my parents have had on my life, nor how much they mean to me. They made this thesis possible, and it is dedicated to them.

Thank you all.

TABLE OF CONTENTS

1 Introduction **1**
1.1 Particles and Forces . . . 4
1.1.1 Leptons . . . 5
1.1.2 Quarks . . . 5
1.1.3 Particle Interactions and Force Mediators . . . 6
1.1.4 Gravitation and Electromagnetism . . . 8
1.1.5 The Weak Force . . . 9
1.1.6 The Strong Force . . . 12
1.2 Why Semileptonic B-Meson Decay? . . . 14

2 The Theory of Semileptonic B Decay **16**
2.1 Calculation of the Semileptonic Rate . . . 18
2.1.1 Phase Space . . . 18
2.1.2 The Matrix Element . . . 20
2.1.3 The Free-Quark Calculation of the Rate . . . 22
2.2 The Operator Product Expansion . . . 23
2.2.1 Quark-Hadron Duality . . . 25
2.3 Heavy Quark Effective Theory . . . 26
2.3.1 The HQET Hamiltonian . . . 27
2.3.2 HQET parameters . . . 29
2.4 Measurements of HQET . . . 31
2.4.1 The Semileptonic Branching Ratio . . . 31
2.4.2 Moments . . . 33

3 CESR and CLEO **35**
3.1 CESR - The Cornell Electron Storage Ring . . . 36
3.2 The CLEO Detector . . . 40
3.2.1 A Few Words About Tracking . . . 43
3.2.2 The Inner Tracking System: PT, VD, and SVX . . . 44
3.2.3 The Central Drift Chamber . . . 47
3.2.4 The Time-of-Flight Counters . . . 52
3.2.5 The Electromagnetic Calorimeter . . . 53
3.2.6 The Magnetic Field . . . 56
3.2.7 The Muon Chambers . . . 56

3.2.8 The Trigger and Data Acquisition System 58
3.2.9 Event Reconstruction 60
3.3 Physics Simulation 60

4 Measuring The Lepton Energy Spectrum 62
4.1 Strategy For Extracting the $B \to X_c e\nu$ Spectrum 62
4.1.1 Diagonal Cut 64
4.1.2 $B^0\bar{B}^0$ Mixing 66
4.2 Data Samples and Event Selection 68
4.2.1 Monte Carlo Samples 69
4.3 Lepton Identification 70
4.3.1 Track Quality 70
4.3.2 Muon Identification 71
4.3.3 Electron Identification 72
4.3.4 Physics Vetoes 76
4.3.5 Raw Spectra 78
4.4 Background Corrections to Raw Spectra 79
4.4.1 Fake Leptons 82
4.4.2 Veto and Diagonal-Cut Leakage 87
4.4.3 Nonvetoed Backgrounds 89
4.5 Efficiency Corrections 90
4.5.1 Tracking and Electron Identification Efficiency 92
4.5.2 The Embedding Study 94
4.5.3 Other Efficiencies and Detector Bremsstrahlung 102
4.6 Primary Spectrum Extraction 102
4.6.1 Correction to Secondary Spectrum 104
4.6.2 Solving the Equations 107
4.7 Cross-Checks of the Semileptonic Spectra 108
4.7.1 Analyzing Monte Carlo as Data 108
4.7.2 MC as Data Study of Same-B Secondaries 110
4.7.3 MC as Data Study of Opposite-B Secondaries 111
4.7.4 Consistency Checks: Splitting the Data Sample 113

5 Systematic Errors 119
5.1 Veto-Leakage Corrections 119
5.2 Diagonal Cut Leakage Correction 120
5.3 Non-Vetoed Background Corrections 120
5.4 Fake Muon Tag Correction 122
5.5 Electron Identification Systematic Errors 122
5.6 Tracking Efficiency 128

5.7 Diagonal Cut Efficiency 131
5.8 Veto Efficiency 131
5.9 $\Delta(p)$ and $B^0\bar{B}^0$ Mixing 134
5.10 Summary of Sources of Systematic Uncertainty 134

6 Results: Semileptonic Branching Ratio 137
6.1 Effective Number of Tags 137
6.1.1 Corrections To Raw Tag Count 138
6.1.2 Event Selection Efficiency Correction 138
6.2 Fraction Below 600 MeV/c 144
6.3 The Branching Ratio 148

7 Results: Lepton Energy Moments 153
7.1 $B \to X_u e\nu$ Correction 154
7.2 Boost Correction 157
7.3 Electroweak Correction 157
7.4 Moments 158
7.4.1 Errors and Correlations on the Moments 158

8 Interpretation and Conclusions 172
8.1 Branching Ratio 172
8.1.1 The Semileptonic Rate 174
8.2 Moments, HQET Parameters, and $|V_{cb}|$ 175
8.2.1 Results in the Bauer Formulation 177
8.2.2 Results in the Uraltsev Formulation 187
8.3 Conclusion 192

BIBLIOGRAPHY 195

LIST OF TABLES

1.1 The elementary particles in the Standard Model. 7

4.1 Charge correlations for dilepton $B\bar{B}$ events. 63

6.1 Yields and backgrounds for tag count. Errors are statistical only. . . 139
6.2 Results for $b \to c\ell\nu$ fits to determine systematic error due to estimate of measured spectral fraction. Explanations of the fit labels in the first row are given in the text. Entries denoted with a "*" have been fixed for that fit. Values for branching ratios are in percent. 149
6.3 Systematic errors on the spectral fraction below 600 MeV from the fitting study. 150
6.4 **Left:** Breakdown of systematic errors on $\mathcal{B}_{SL}$. **Right:** Details of electron identification systematic error on $\mathcal{B}_{SL}$. 152

7.1 Breakdown of corrections and errors on $\langle E_\ell \rangle$ at various lower lepton energy cuts. All numbers are in GeV. 159
7.2 Breakdown of corrections and errors on $\langle E_\ell^2 \rangle$ at various lower lepton energy cuts. All numbers are in GeV^2. 160
7.3 Breakdown of corrections and errors on $\langle (E_\ell - \langle E_\ell \rangle)^2 \rangle$ at various lower lepton energy cuts. All numbers are in GeV^2. 161
7.4 Breakdown of corrections and errors on $\langle (E_\ell - \langle E_\ell \rangle)^3 \rangle$ at various lower lepton energy cuts. All numbers are in GeV^3. 162
7.5 Breakdown of electron ID systematic errors on $\langle E_\ell \rangle$ at various lower lepton energy cuts. All numbers are in GeV. 163
7.6 Breakdown of electron ID systematic errors on $\langle E_\ell^2 \rangle$ at various lower lepton energy cuts. All numbers are in GeV^2. 163
7.7 Breakdown of electron ID systematic errors on $\langle (E_\ell - \langle E_\ell \rangle)^2 \rangle$ at various lower lepton energy cuts. All numbers are in GeV^2. 164
7.8 Breakdown of electron ID systematic errors on $\langle (E_\ell - \langle E_\ell \rangle)^3 \rangle$ at various lower lepton energy cuts. All numbers are in GeV^3. 164
7.9 Correlations between measurements of $\langle E_\ell \rangle$ for various lower lepton energy cuts. 166
7.10 Correlations between measurements of $\langle E_\ell \rangle$ (rows) and $\langle E_\ell^2 \rangle$ (columns) for various lower lepton energy cuts. 167

7.11 Correlations between measurements of $\langle E_\ell \rangle$ (rows) and $\langle (E_\ell - \langle E_\ell \rangle)^2 \rangle$ (columns) for various lower lepton energy cuts. 167
7.12 Correlations between measurements of $\langle E_\ell \rangle$ (rows) and $\langle (E_\ell - \langle E_\ell \rangle)^3 \rangle$ (columns) for various lower lepton energy cuts. 168
7.13 Correlations between measurements of $\langle E_\ell^2 \rangle$ for various lower lepton energy cuts. 168
7.14 Correlations between measurements of $\langle E_\ell^2 \rangle$ (rows) and $\langle (E_\ell - \langle E_\ell \rangle)^2 \rangle$ (columns) for various lower lepton energy cuts. 169
7.15 Correlations between measurements of $\langle E_\ell^2 \rangle$ (rows) and $\langle (E_\ell - \langle E_\ell \rangle)^3 \rangle$ (columns) for various lower lepton energy cuts. 169
7.16 Correlations between measurements of $\langle (E_\ell - \langle E_\ell \rangle)^2 \rangle$ for various lower lepton energy cuts. 170
7.17 Correlations between measurements of $\langle (E_\ell - \langle E_\ell \rangle)^2 \rangle$ (rows) and $\langle (E_\ell - \langle E_\ell \rangle)^3 \rangle$ (columns) for various lower lepton energy cuts. 170
7.18 Correlations between measurements of $\langle (E_\ell - \langle E_\ell \rangle)^3 \rangle$ for various lower lepton energy cuts. 171

8.1 Solutions for m_b, μ_π^2, and $|V_{cb}|$ in the Uraltsev formulation from $\langle E_\ell \rangle$ and $\langle (E_\ell - \langle E_\ell \rangle)^2 \rangle$ with various lepton-energy cuts. The first quoted error on $|V_{cb}|$ is from the measurement uncertainties of $\mathcal{B}_{SL}$ and τ_B, the second is from the measurement uncertainties of the moments, and the third is from uncertainties in $m_c, \mu_g^2, \rho_D^3, \rho_{LS}^3$, and α_s. 190

LIST OF FIGURES

1.1 Photon exchange in electron-electron scattering. 8
1.2 A weak interaction vertex involving leptons. 10
1.3 A weak interaction vertex involving quarks. 11
1.4 Hadronization in $\Upsilon(4S)$ decay. Here a u and $\bar{u}$ are created from the energy of the strong force interaction between the b and $\bar{b}$ as they split apart. 14

2.1 Semileptonic decay of a B meson containing a b quark and a "spectator" u or d quark, denoted as q_{sp}. 17
2.2 A more realistic picture of B meson semileptonic decay. 17
2.3 Schematic of the steps of applying the Operator Product Expansion. 24

3.1 The colliding-beam facility at Cornell. 36
3.2 The annual integrated lumonisity from CESR. 39
3.3 The hadronic cross-section in the Upsilon region. 40
3.4 The side view of the CLEO II.V detector 42
3.5 Layout of the PT and VD in CLEO II 45
3.6 End-on (top) and side (bottom) cross-sectional views of the SVX detector in CLEO II.V 46
3.7 A cross-sectional view of the CLEO II main drift chamber. 47
3.8 A CLEO event display containing examples of both ghost and curler tracks, viewed in the r-ϕ plane. DR hits are represented by dots and reconstructed tracks are shown as solid and dashed lines. Tracks 16 and 17 are two halves of a curler. Tracks 5 and 13 are a "ghost pair". 50
3.9 Measured dE/dx as a function of momentum. The solid lines represent theoretical curves for various particle types. 51
3.10 Measured times of flight as a function of momentum. The solid lines represent theoretical curves for various particle types. 52
3.11 A cross-section of a muon chamber super-layer. 57

4.1 Monte Carlo simulation of electron momentum versus the cosine of the opening angle between the tag lepton and the signal electron (cos $\theta_{\ell e}$) for dilepton pairs from opposite B's (top) and from the same B (right). The line indicates $p + cos\theta_{\ell e} = 1$. 65

4.2 The efficiency of the diagonal cut determined with Monte Carlo simulations of lepton-tagged $B\bar{B}$ events with four different semileptonic decay modes. Clockwise from the top left, the points represent $B \to De\nu$, $B \to D^{*}e\nu$, $B \to DXe\nu$ and $B \to D^{**}e\nu$. The histograms are the same in all four plots, and give the overall efficiency for the complete mixture of semileptonic B decays. There is no discernible mode-to-mode variation. 67
4.3 Electron spectra for ON and scaled-OFF samples of events with unlike- (top) and like-sign (bottom) tags. 79
4.4 Continuum-subtracted electron spectra for all unlike-sign tagged events (histogram) and those passing the diagonal cut (points). 80
4.5 TEID (left) and `DPTHMU` ≥ 5 (right) fake rates for charged pions (top) and charged kaons (bottom). Note the different vertical scales. . . . 83
4.6 Relative abundances of $\pi^{\pm}$ (blue solid line), $K^{\pm}$ (red dashed line), and $p/\bar{p}$ (green dotted line) from generic CLEO $B\bar{B}$ Monte Carlo. 84
4.7 TEID (left) and muon (right) fake probabilities as a function of hadron momentum from 0.6 to 3.0 GeV/c. 84
4.8 Ratio of muons to electrons in reconstructed momentum in Monte Carlo. 85
4.9 Fits of the Monte Carlo spectra of signal electrons with an electron tag that fail one of the J/ψ vetoes to the corresponding spectra in data. The vetoed electrons in Monte Carlo have not been identified by `QQ` as coming from J/ψ decays, and thus include the contribution of mistakenly vetoed tracks, just as in data. The plots are (clockwise from top left): unlike-sign signal electrons from any source with a J/ψ-vetoed electron tag; vetoed unlike-sign signal electrons with a tag electron that passed all vetoes; vetoed like-sign signal electrons with a tag electron that passed all vetoes; and like-sign signal electrons from any source with a J/ψ-vetoed electron tag. The peaking effect in the top left plot is an artifact of the diagonal cut. The Monte Carlo simulation shows excellent agreement with the data. 88
4.10 Projections in momentum (left) and `CZCD` (right) of same-B secondary fits. The points are data; the histogram is the fitted Monte Carlo. . 89
4.11 Backgrounds in the charge-separated spectra. Each category includes backgrounds to both tag and signal leptons, unless otherwise noted. . 91
4.12 Unlike- (top) and like-sign (bottom) electron spectra after all backgrounds have been subtracted. 92
4.13 Efficiency of our electron identification package in CLEO II (left) and CLEO II.V (right). 93

4.14 Comparison of the momentum *(left)* and polar angle `CZCD` *(right)* distributions of good-barrel tracks for pre-embedded radiative Bhabha events for data (points) and Monte Carlo (histogram). 98
4.15 Efficiency ratio of track-quality cuts in embedded data and embedded MC. 100
4.16 *Left:* TEID efficiencies for reweighted unembedded (histogram) and embedded (points) radiative Bhabha events. *Right:* TEID efficiencies for unreweighted (histogram) and reweighted (points) embedded radiative Bhabha tracks. 101
4.17 Overall efficiencies for unlike-sign (left) and like-sign spectra. Detector bremsstrahlung is included in this correction. 103
4.18 Fully corrected unlike-sign (left) and like-sign spectra. These are the charged-separated spectra that are passed to Eqs. 4.1 and 4.2. 103
4.19 Breakdown of sources of secondary electrons. The branching ratios are from MC. 105
4.20 Secondary correction factor $\Delta(p)$ 106
4.21 Primary (points) and secondary spectra (histogram). 107
4.22 Results of MC-as-data analysis (points) compared to `QQ` (solid line) for the fully-corrected unlike-sign (left) and like-sign spectra. 109
4.23 Fit of the secondary electron spectrum from the opposite-B sample. The points are data and the fitted histogram is the Monte Carlo. . . 112
4.24 Primary spectra from CLEO II (points) and CLEO II.V (histogram) events. Plots are normalized to their respective number of tags. . . . 115
4.25 Primary spectra from electron-tag (points) and muon-tag (histogram) events. Plots are normalized to equal areas. 116
4.26 Primary spectra from positive tag (points) and negative tag (histogram) events. Plots are not normalized. 117
4.27 Primary spectra from high-p tag (points) and low-p tag (histogram) events. Plots are normalized to their respective number of tags. . . . 118

5.1 The final $b \to ce\nu$ momentum spectra with the alternative EID packages (points) overlaid with standard TEID spectrum (solid line). Note the limits on the momentum axes; only momentum ranges where the spectra differ are shown. 127
5.2 The efficiencies of the alternative EID packages (points) overlaid with standard TEID efficiency (solid line). Note the limits on the momentum axes; only momentum ranges where the efficiencies differ are shown. 129

5.3 The total fake probabilities of the alternative EID packages (points) overlaid with standard TEID fake probability (solid line). Note the limits on the momentum axes; only momentum ranges where the fake probabilities differ are shown. 130
5.4 J/ψ veto efficiencies for unlike-sign events with electron (left) and muon (right) tags. 132
5.5 Invariant mass of tag and signal track pair vs. signal momentum in data (left) and Monte Carlo (right) for events with an unlike-sign electron tag. The diagonal cut is applied. The effect of the J/ψ veto is clearly seen, as is the range in signal momentum in which it appears. 133

6.1 Multiplicity of good track-quality tracks in data (points) and Monte Carlo (histogram) for tag events (top) and primary signal events (bottom). The `NTRKGD`=10 bin in both plots is the sum of all events with `NTRKGD`$\geq$ 10. 141
6.2 Multiplicity of good track-quality tracks in data (points), reweighted Monte Carlo (solid histogram), and standard Monte Carlo (dashed histogram) for tag events. The Monte Carlo has been reweighted as described in the text. The `NTRKGD`=10 bin in both plots is the sum of all events with `NTRKGD`$\geq$10. 143
6.3 Results of fitting the final $B \to Xe\nu$ spectrum. 146

7.1 Spectrum of electrons from $B \to X_u e\nu$ decays from the `INCLGEN` Monte Carlo sample reweighted to enhance(red dashed)/degrade(blue solid) the $B \to \pi/\rho/\eta/\omega e\nu$ portion of the 2.2-2.6 GeV endpoint region by 30%. 155
7.2 The final $B \to X_c \ell\nu$ spectrum. 156

8.1 Measurements of the semileptonic branching ratio. The measurement presented in this thesis is shown in red. 173
8.2 **Left:** $\langle E_\ell \rangle$ as a function of E_{min}. The points are data and the band is the $\pm 1\sigma$ prediction in the Bauer pole-mass scheme [11]. **Right:** $\langle E_\ell \rangle_{data} - \langle E_\ell \rangle_{HQET}$ as a function of E_{min}. The points are the data with the predicted moment subtacted, and the band is the $\pm 1\sigma$ prediction. Inputs for these plots were set by $\langle E_\gamma \rangle_{2.0}$ [17] and $\langle E_\ell \rangle_{1.5}$. 179
8.3 Bands in the $\overline{\Lambda} - \lambda_1$ plane from $\langle E_\ell \rangle$ with $E_\ell > 0.7$ GeV (band 1), $\langle (E_\ell - \langle E_\ell \rangle)^2 \rangle$ with $E_\ell > 0.7$ GeV (band 2), $\langle E_\ell \rangle_{1.5} - \langle E_\ell \rangle_{0.7}$ (band 3), and $\langle (E_\ell - \langle E_\ell \rangle)^2 \rangle_{0.7} - \langle (E_\ell - \langle E_\ell \rangle)^2 \rangle_{1.5}$ (band 4). The widths of the bands reflect the combined experimental and theoretical uncertainties. These bands were calculated with the Bauer pole-mass formulation [11]. 181

8.4 Bands in the $\overline{\Lambda} - \lambda_1$ plane for $\langle E_\gamma \rangle_{2.0}$ (blue) and $\langle M_X^2 - \bar{M}_D^2 \rangle_{1.5}$ (red). Widths of bands represent measurement uncertainty on the moments. 183
8.5 Bands in the $\overline{\Lambda} - \lambda_1$ plane for $\langle E_\gamma \rangle_{2.0}$ (blue) and $\langle E_\ell \rangle_{0.7}$ (red). Widths of bands represent measurement uncertainty on the moments. . . . 185
8.6 Bands in the $\overline{\Lambda} - \lambda_1$ plane for $\langle E_\ell \rangle_{0.7}$ (blue) and $\langle (E_\ell - \langle E_\ell \rangle)^2 \rangle_{0.7}$ (red). Widths of bands represent measurement uncertainty on the moments. 186
8.7 **Left:** $\langle E_\ell \rangle$ as a function of E_{min}. The points are data and the line is the prediction in the Uraltsev formulation. **Right:** $\langle E_\ell \rangle^{data} - \langle E_\ell \rangle^{HQET}$ as a function of E_{min}. The points are the data with the predicted moment subtracted. Inputs for these plots were set by $\langle E_\ell \rangle_{0.6}$ and $\langle (E_\ell - \langle E_\ell \rangle)^2 \rangle_{0.6}$. The error bars on the points in both plots represent the measurement uncertainty of the moments. 189
8.8 Bands in $m_b - \mu_\pi^2$ space of the Uraltsev formulation determined by $\langle E_\ell \rangle$ (blue) and $\langle (E_\ell - \langle E_\ell \rangle)^2 \rangle$ (yellow) with lepton-energy cuts of 0.6, 0.9, 1.2, and 1.5 GeV, as indicated by the title of each plot. The width of each band represents the measurement uncertainty of the moment. 191

CHAPTER 1

Introduction

In 1897, J.J. Thomson determined that the so-called "cathode rays" emitted by a hot filament were actually streams of negatively-charged particles. He called them *corpuscles* and their charge the *electron* (the term "electron" would later be applied to the particle itself). Thomson postulated that the electron was a fundamental constituent of atoms. Since atoms were much heavier than his electrons, and electrically neutral on top of that, it was clear that they were not the *only* constituents of atoms. So he proposed a model of the atom that had the electrons embeddeded in a continuous medium of positive charge, calling it the "plum-pudding" model.

A few years later, Ernst Rutherford formulated a test of Thomson's model. He performed an experiment where he fired a beam of α particles (helium nuclei) into a thin sheet of gold foil. If Thomson's model was correct, the α particles' trajectories should be deflected slightly by their passage through the uniformly distributed positive charge of the gold atoms. Instead, Rutherford found that most of the α's passed straight through the foil (suggesting empty space), while some of them richocheted off at extreme angles (suggesting that they encountered something very massive). Apparently, most of the mass of an atom was concentrated in a very small space.

Niels Bohr soon put forth a model that claimed a hydrogen atom consists of an

electron in planetary orbit around a *proton* (as the hydrogen nucleus was called). Enormously successful in predicting the emission spectrum of hydrogen, it suffered from the fact that it could not be extrapolated to explain the structure of heavier elements. While helium (the next heaviest atom) had two electrons (and therefore two protons in its nucleus), it was four times heavier than hydrogen. Obviously, the nucleus contained more than just protons. So when in 1932 James Chadwick discovered the *neutron*, a particle similar in weight to the proton but electrically neutral, the pieces fell into place: atoms were made of electrons orbiting a nucleus containing *nucleons*, as protons and neutrons are collectively called.

However, there were still problems, and many of the proposed answers to these problems predicted the existence of particles beyond the electron, proton, and neutron. Dirac's attempt to derive a theory for the electron that incorporated both quantum theory and special relativity demanded the existence of the *positron*, a positively-charged antimatter partner to the electron. To explain why electrons emitted in nuclear β decay were not monoenergetic, Pauli predicted the existence of the chargeless, massless *neutrino*. Yukawa proposed the existence of a *meson*, a charged particle about one-sixth the mass of a nucleon, to explain how all those positively-charged protons could be held so closely together in the nucleus[1]

These predicted particles were searched for and subsequently seen in the laboratory over the next several years. However, also uncovered were many other types of particles that were completely unexpected: several types of mesons were discov-

[1]Yukawa's insightful model eventually proved too simplistic, and the name "meson" is now used for a different purpose.

ered, as well as many heavier particles that were more similar to the nucleons. With this proliferation of new particles, attempts were made to find patterns among them. In the sixties, Murray Gell-Mann proffered an explanation for the patterns in the properties of the various particles. He proposed that all the known particles (except the electron, muon, and the neutrino) were themselves made up of three types of fractionally-charged particles called *quarks*. Since no fractionally-charged particles had ever been observed, this theory did not seem well-motivated to most physicists; quarks seemed like a clever fiction. Experimental evidence was needed.

In the spirit of Rutherford, physicists at the Stanford Linear Accelerator Center fired a high-energy beam of electrons into a target of protons, probing for substructure. These "deep-inelastic scattering" experiments showed that nucleons are *not* fundamental, that in fact they consisted of three *partons*. Eventually[2] these partons were recognized as Gell-Mann's quarks.

So far as we know today, quarks have no substructure. They, along with the *leptons* (the class of particles consisting of the electron, its heavier cousins the μ and the τ, and the neutrinos) are the fundamental constituents of matter.

Atoms to nuclei, nuclei to nucleons, nucleons to quarks; this quest to delve deeper and deeper into matter, peeling away layers of abstraction until left with only the

[2]After the deep-inelastic scattering experiments, it was suspected that these partons were Gell-Mann's quarks, but not many physicists were ready to fully recognize them as such. The deciding piece of evidence for the quark model was provided in the "November Revolution" of 1974, with the discovery of the J/ψ meson that was much heavier than any other meson ever seen before. The quark model was ready with an explaination: it contained a fourth type of quark that the theory predicted. This explanation is now the accepted theory.

fundamental constituents, is what motivates the particle physicist. This thesis will describe the measurement of one part of the current model of elementary particle physics, called the Standard Model.

The first two chapters of this thesis will lay out the theoretical motivation for the measurements made here. The rest of this chapter will give a qualitative introduction to the current theory of elementary particle interactions, the Standard Model. The second chapter will explain in more detail the physics of semileptonic B-meson decays. In it, the theory of the weak decay that lays at the core of this process, as well as the complicating effects of the strong force, will be explored.

1.1 Particles and Forces

In the Standard Model, our universe consists of three types of particles: *leptons*, *quarks*, and the force-mediating *gauge bosons*. Each particle has an *antiparticle*, with the same mass and opposite quantum numbers. Some particles, like the photon, are their own antiparticles. One particle, the yet-to-be-seen Higgs boson, does not fall into these categories, and plays a special role in the theory, in particular the generation of the masses of the particles. All of our knowledge about the properties of matter arise from the observations of interactions of these particles.

1.1.1 Leptons

There are six types of leptons. The most familiar is the electron, denoted e^- or simply e. [3] The electron has two heavier cousins, the muon (μ), and tau (τ), both also negatively charged. The remaining three leptons are the massless[4] and chargeless neutrinos. The neutrinos are partnered up with the charged leptons: the electron neutrino ν_e, the muon neutrino ν_μ, and the tau neutrino ν_τ. The properties of all six leptons are summarized in Table 1.1.

1.1.2 Quarks

Quarks make up the vast majority of matter in the everyday world. As with the leptons, there are six flavors of quarks: up, down, charm, strange, bottom, and top. The properties of each are shown in Table 1.1. The complicated strong interactions inside hadrons make defining and measuring individual quark masses difficult, so some of the masses that appear in Table 1.1 are approximate. While the quarks carry a fractional electric charge, no particles with fractional charge have ever been observed in the laboratory. It is a feature of the strong force (described below) that quarks are only observed in bundles of three quarks or antiquarks called *baryons*, or quark-antiquark bound states called *mesons*. Baryons and mesons are collectively called

[3]The electron's antiparticle, the positron, will also be denoted as e at times throughout this thesis; in general, we will not distinguish between particles and antiparticles, as it can usually be inferred by context which is meant.

[4]This is not exactly true; there is growing evidence that neutrinos may have small but nonzero masses from neutrino mixing experiments. That is beyond the scope of this thesis, however, and since the Standard Model assumes the neutrinos are massless, I will do the same.

hadrons. Protons, for example, are made up of two u quarks and a d-quark, while neutrons consist of one u quark and two d quarks. The particles studied in this thesis, B mesons, contain a $\bar{b}$ antiquark paired with a u or a d quark.[5]

The quarks and leptons each fall naturally into three groupings called *generations*. The source of this structure is not understood, just as we do not understand the patterns of masses and decay couplings. The u and d quarks are in the first generation, the c and s quarks in the second, and the t and b quarks in the third. Similarily, the leptons are grouped as (e, ν_e), (μ, ν_μ), and (τ, ν_τ).

1.1.3 Particle Interactions and Force Mediators

Particles interact via the four fundamental forces: *gravity*, *electromagnetism*, the *strong force*, and the *weak force*. In the Standard Model, interactions are described as the exchange of particles called *mediators* of the force responsible for the interaction. Figure 1.1 shows a diagram of a photon being exchanged between two electrons, describing an interaction via the electromagnetic force. A photon is emitted by an incoming electron. This photon carries momentum and energy from the emitting electron and transfers it to the absorbing electron. An electron cannot just emit a photon and conserve energy and momentum. However, by the grace of the uncertainty

[5]It is for historical reasons that the B meson contains the $\bar{b}$-antiquark, while the $\bar{B}$ meson contains the b-quark. When the first strange-flavored particles, the Λ baryons, were discovered it was not known that they actually bore the $\bar{s}$-antiquark, and "foolish" consistency led to a similar convention for naming bottom-flavored hadrons. It is similar to the choice faced by Benjamin Franklin when labeling the two electric charges positive and negative, not knowing that by his choice the electron would inconveniently carry a negative charge, thus plaguing freshman physics students with sign errors for centuries to come.

	Name	Symbol	Charge	Spin	Mass (MeV/c^2)
Quarks	Up	u	$\frac{2}{3}$	$\frac{1}{2}$	1.5 to 4.5
	Down	d	-$\frac{1}{3}$	$\frac{1}{2}$	5.0 to 8.5
	Charm	c	$\frac{2}{3}$	$\frac{1}{2}$	1000 to 1500
	Strange	s	-$\frac{1}{3}$	$\frac{1}{2}$	80 to 155
	Top	t	$\frac{2}{3}$	$\frac{1}{2}$	174,000
	Bottom	b	-$\frac{1}{3}$	$\frac{1}{2}$	4000 to 4500
Leptons	Electron	e	-1	$\frac{1}{2}$	0.511
	Electron Neutrino	ν_e	0	$\frac{1}{2}$	$< 3 \times 10^{-6}$
	Muon	μ	-1	$\frac{1}{2}$	105.7
	Muon Neutrino	ν_μ	0	$\frac{1}{2}$	< 0.19
	Tau	τ	-1	$\frac{1}{2}$	1777 $\pm$ 0.28
	Tau Neutrino	ν_τ	0	$\frac{1}{2}$	< 18.2
Mediators	Photon (EM)	γ	0	1	0
	Gluon (Strong)	g	0	1	0
	Weak Bosons	W^+	+1	1	80,423 $\pm$ 39
		W^-	-1	1	80,423 $\pm$ 39
		Z^0	0	1	91,188 $\pm$ 2.1
	Higgs	H	0	1	$> 114,300$

Table 1.1: The elementary particles in the Standard Model.

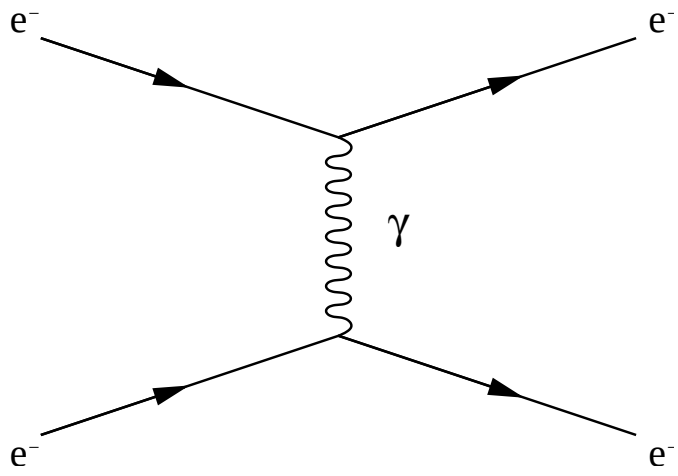

Figure 1.1: Photon exchange in electron-electron scattering.

principle, the energy ΔE needed to emit the photon can be "borrowed" as long as the photon is reabsorbed before time $\Delta t \simeq (\hbar/\Delta E)$. A photon exchanged in such a process is called a *virtual* photon, and is not a real photon in the sense that it can be detected. The strong force is similarily described by the exchange of virtual gluons, and the weak force by the exchange of virtual $W^{\pm}$ and Z^0 bosons.

Each force also has an associated *coupling constant*, which denotes the strength of the interactions of that force. The coupling of the strong force α_s is, as the name suggests, the largest. The electromagnetic coupling α_{EM} is two orders of magnitude smaller, and the weak force coupling G_F is a thousand times smaller still.

1.1.4 Gravitation and Electromagnetism

The gravitational force is the weakest of the four forces, yet to a certain extent it is the most familiar. Isaac Newton first developed a comprehensive model for

gravity in 1687, a theory that was later subsumed by Albert Einstein into his General Theory of Relativity. However, neither of these theories are quantum theories, nor has the proposed mediator of the gravitational field, the *graviton*, been discovered. Because it is so weak relative to the other forces, individual particles do not interact meaningfully via the gravitational force, and gravity is therefore not described in the Standard Model.

The electromagnetic force is responsible for almost all of the myriad of interactions common to everyday life. A complete classical theory was first derived by James Maxwell and was not only compatible with relativity, it was the inspiration for Einstein's work. The current quantum theory of electromagnetic interactions, *quantum electrodynamics* or *QED*, stands today as the most successful and precisely tested physical theory yet devised. The mediator of the electromagnetic force, the *photon*, couples to electric charge; therefore, all charged particles interact via the electromagnetic force.

1.1.5 The Weak Force

The weak force is responsible for the decay of quarks and leptons into lighter quarks and leptons. All quarks and leptons interact via the weak force. Unlike all the other gauge bosons, the mediators of the weak force, the $W^{\pm}$ and the Z^0 are very massive, causing the weak force to be short-ranged. It is also the only force that is capable of changing the *flavor* of a quark or lepton, like a bottom quark into a charm quark, or a muon into an electron.

Shown in Fig. 1.2 is the decay of an unstable lepton by a charged-current interac-

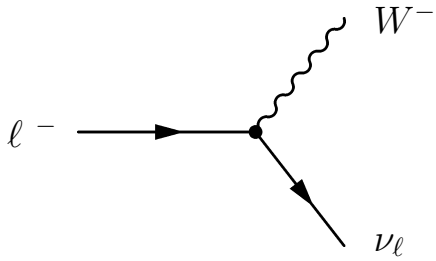

Figure 1.2: A weak interaction vertex involving leptons.

tion. Here a muon or tau is converted into its corresponding neutrino and a vitrual W^- is emitted. This is not a complete physical process, as the W is virtual and needs to decay into something else before this process can be observed. Note that couplings of the W to leptons of different generations (i.e. $\mu^- \to \nu_\tau W^-$) are not allowed within the Standard Model.

Quarks also decay into other quarks via the weak force by coupling to W bosons. A Feynman diagram of a u quark decaying to a d quark and emitting a vitrual W^+ is shown in Fig. 1.3. In contrast to leptonic decays, quarks *can* decay cross-generationally. Here it is necessary to make an important distinction: the generations defined by the quark masses are *not* the generations obeyed by the weak force. However, we can define weak eigenstates of quarks by rotating the mass eigenstates of down-type quarks into a new basis using a 3×3 matrix, called the *Cabibbo-Kobayashi-*

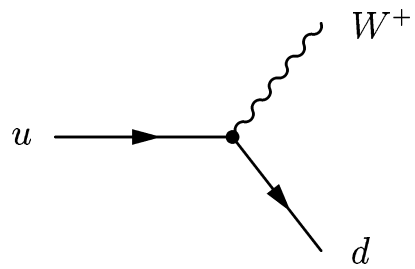

Figure 1.3: A weak interaction vertex involving quarks.

Maskawa (*CKM*) matrix [1][6]:

$$\begin{pmatrix} d' \\ s' \\ b' \end{pmatrix} = \begin{pmatrix} V_{ud} & V_{us} & V_{ub} \\ V_{cd} & V_{cs} & V_{cb} \\ V_{td} & V_{ts} & V_{tb} \end{pmatrix} \begin{pmatrix} d \\ s \\ b \end{pmatrix}. \tag{1.1}$$

Now we can write the weak eigenstates as mixtures of the mass eigenstates:

$$|b'\rangle = V_{td}|d\rangle + V_{ts}|s\rangle + V_{tb}|b\rangle. \tag{1.2}$$

The weak interaction only allows transitions within these new generations: $(u \leftrightarrow d')$, $(c \leftrightarrow s')$, and $(t \leftrightarrow b')$. Since we only observe the quarks in their the mass eigenstates, the experimentally measured probability for each weak transition is the overlap of the mass and weak eigenstates. For example, since V_{tb} is much larger than V_{ts} or V_{td}, the bottom quark mass eigenstate is mostly b', and very little s' or d'. Therefore, decays

[6]Again, it is not exactly true that leptons cannot "jump" generations. The main purpose of neutrino mixing experiments is to measure elements of the MNS matrix, the analogous matrix to the CKM matrix in the lepton sector. And again, this is "beyond the Standard Model," and will not be discussed further in this thesis.

of the top quark to the bottom quark are much more common than decays to strange or down quarks. In this way, the CKM matrix governs the relative probabilities of different quark decays.

The elements of the CKM matrix are fundamental inputs of the Standard Model, and must be experimentally determined. The current experimental limits on their magnitudes are as follows [2]:

$$\begin{pmatrix} 0.9741\,\text{to}\,0.9756 & 0.219\,\text{to}\,0.226 & 0.0025\,\text{to}\,0.0048 \\ 0.219\,\text{to}\,0.226 & 0.9732\,\text{to}\,0.9748 & 0.038\,\text{to}\,0.044 \\ 0.004\,\text{to}\,0.014 & 0.037\,\text{to}\,0.044 & 0.9990\,\text{to}\,0.9993 \end{pmatrix}. \tag{1.3}$$

1.1.6 The Strong Force

The strong force is what holds quarks in hadrons, and (indirectly) holds nucleons in the nucleus. The current theory of strong interactions is called *quantum chromodynamics*, or *QCD*, and is modeled on QED. The strong force involves all particles that carry the *color* charge. Color charge has nothing to do with real color, and is rather more analogous to the electric charge; why it is called color charge will become apparent in a moment. Whereas there is only one type of electric charge (that can be positive or negative; a charge and an anti-charge, so to speak), there are three types of color charge: "red", "blue", and "green". Quarks carry color charge, and can only group themselves into hadrons in combinations that make the overall state "colorless". Baryons form by combining one "red", one "blue", and one "green" quark, making the baryon itself "white," or colorless (and it is here that the reason for calling the strong charge "color" becomes apparent). Mesons form by combining,

say, a blue quark with an anti-blue anti-quark, making a colorless meson. Leptons do not carry color charge, and thus do not participate in strong interactions. The strong force mediator, the massless *gluon*, couples to the color charge. Interestingly enough, the gluons themselves carry color, allowing them to interact with each other, unlike photons.

The name "strong coupling constant" for α_s is a misnomer: α_s is not really a constant, but it increases as the distance between quarks increases. This "running" coupling constant has some interesting implications. As the distance between two quarks decreases, α_s *decreases*. Inside a hadron, α_s is so small that the quarks essentially do not interact, and rattle around freely. This phenomenon is called *asymptotic freedom*. On the flip side is *confinement*: α_s increases as separation increases, binding the quarks inside hadrons. As quarks in a hadron separate, the energy in the strong force coupling of the quarks increases. Eventually, there is enough energy in the coupling to create a quark-antiquark pair as it departs. The departing quark will then pair with the newly-formed antiquark to form a meson, and the newly-formed quark can replace the departed quark in the old hadron to make it a complete hadron again. This process of creating new quarks and antiquarks to satisfy confinement is called *hadronization*. A diagram of hadronization in $\Upsilon(4S) \to B^+B^-$ decay is shown in Fig. 1.4.

The running of α_s causes the physics of strong-force interactions at short distances to be very different from long-distance interactions, and different theoretical approaches must be employed for each. The borderline between the two regimes is called the QCD scale, and is marked by the parameter $\Lambda_{QCD} \sim 200$ MeV. At dis-

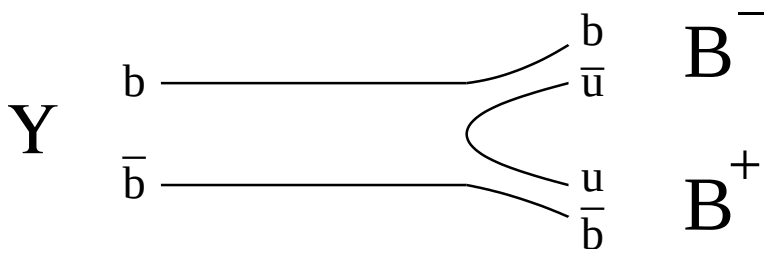

Figure 1.4: Hadronization in $\Upsilon(4S)$ decay. Here a u and $\bar{u}$ are created from the energy of the strong force interaction between the b and $\bar{b}$ as they split apart.

tances much shorter than $1/\Lambda_{QCD}$, α_s is small enough that the strong interaction can be described as the exchange of individual gluons using perturbation theory. At distances of order $1/\Lambda_{QCD}$, quarks and gluons start to hadronize, and QCD becomes non-perturbative.

1.2 Why Semileptonic B-Meson Decay?

In this thesis, we are interested in making a precision measurement of the CKM matrix element V_{cb}. To make this measurement, we need to observe decays where a b quark decays into a c quark.

Observing $b \to c$ decays would be a relatively straightforward task if we were able to see quarks individually. However, the strong force interferes. Because of confinement we do not see quarks; we only see hadrons. Therefore, if we wish to study the weak-force physics of a certain quark, we are forced to observe it interacting via the strong force with other quarks, which will obscure our view of the weak interactions.

Because B mesons are the lightest bottom-flavored hadrons, they can decay only

via the weak force; the flavor-preserving strong and electromagnetic interactions are forbidden because there are no lighter hadrons with the same quark content. Also, b quarks cannot decay to CKM-favored but far heavier t quarks. This leaves only transitions to c or u quarks. And since V_{cb} is roughly 10 times bigger than V_{ub}, approximately 99% of B decays are to final states with mesons containing a charm quark. This makes a sample of B mesons fertile ground for $b \to c$ decays.

Since leptons do not interact via the strong force, we study $B \to X_c \ell \nu$ decays to minimize our sensitivity to the complicating strong force interactions quarks in the final state. However, semileptonic decay processes are still not completely free from the meddling of the strong force. The b quark is still confined in a hadron, where it experiences strong interactions on the order of Λ_{QCD}. However, we can approximate the contribution of the strong force to observed weak decays of hadrons containing quarks of mass $m_q \gg \Lambda_{QCD}$. The details of this approximation are given in the next chapter.

CHAPTER 2

The Theory of Semileptonic B Decay

In this chapter, we detail the theoretical calculation of the differential rate $d\Gamma_{SL}$ of B meson semileptonic decay using the Operator Product Expansion (OPE) and Heavy Quark Effective Theory (HQET).

The semileptonic decay of a B meson is the result of the weak decay of the b quark into a c quark or a u quark and a virtual W, with the virtual W decaying to a lepton-neutrino pair. The diagram for this process is shown in Fig. 2.1. To calculate the rate of this process, we view it as the interaction of a leptonic current and a quark current mediated by W exchange.

Semileptonic decays are not as "clean" as shown in Fig. 2.1, but rather are more like the situation depicted in Fig. 2.2, with gluons being exchanged between the quarks inside the hadron. Moreover, since the energy scale of typical QCD interactions is of the order Λ_{QCD}, there is ample energy to create light quark-antiquark pairs, creating a so-called "brown muck" of gluons and light quarks and antiquarks. The presence of these light degrees of freedom greatly obscures the underlying weak process we are interested in studying. However, the sheer girth of the b-quark presents us with the opportunity to make some simplifying approximations.

First we will turn our attention to calculating the differential decay rate of $B \rightarrow$

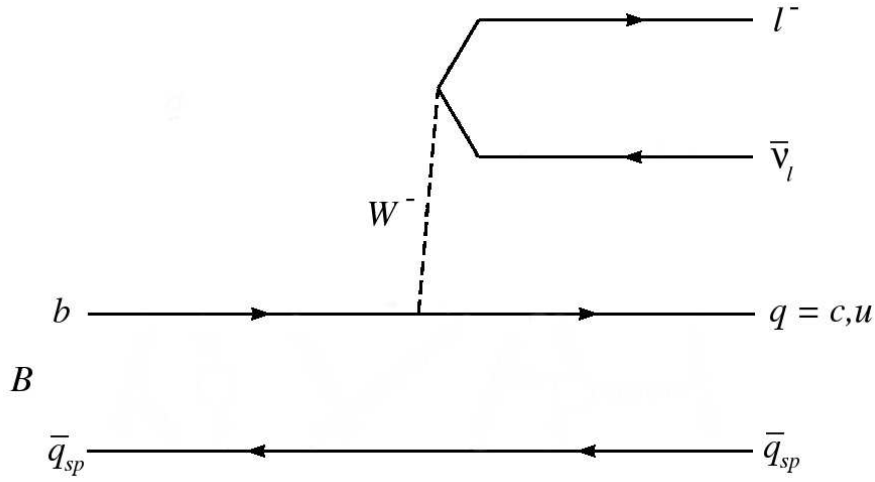

Figure 2.1: Semileptonic decay of a B meson containing a b quark and a "spectator" u or d quark, denoted as q_{sp}.

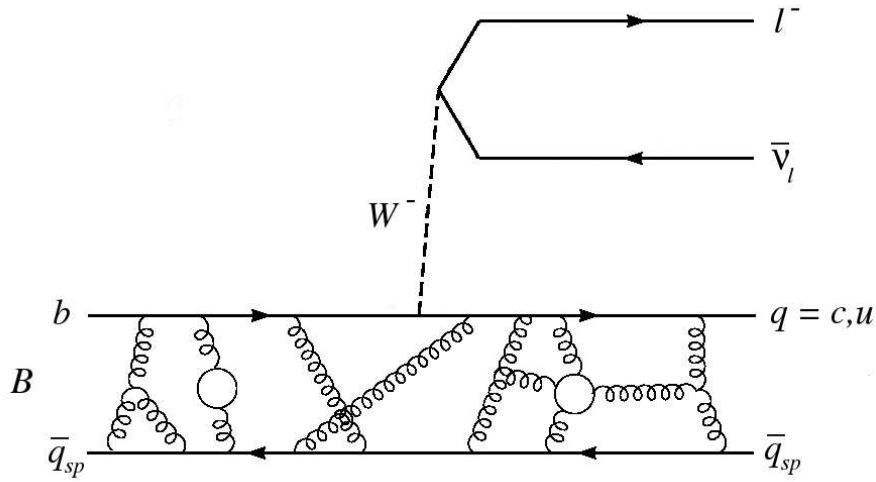

Figure 2.2: A more realistic picture of B meson semileptonic decay.

$X\ell\nu$. Our goal in obtaining an expression for the differential decay rate is to separate the physics processes that we cannot calculate (non-perturbative QCD) from those we can (perturbative QCD and weak physics). Once we have isolated the non-calculable parts, we will express them in a way that makes determination of them possible using data.

2.1 Calculation of the Semileptonic Rate

The general expression for the differential rate of decay for a particle of mass M is given by the "Golden Rule":

$$d\Gamma = \frac{(2\pi)^4}{2M}|\mathcal{M}|^2 d\Phi. \tag{2.1}$$

This expression is useful because it splits the kinematics of the decay from the dynamics. The kinematics are encoded in the *phase space* term $d\Phi$ and depend on the masses and momenta of the particles in the initial and final states. The dynamics, the details of the interactions of the particles via the various forces, are encoded in the *matrix element* $\mathcal{M}$.

2.1.1 Phase Space

Phase space is the term for the "map" of the density of final states for a process that are allowed by energy and momentum conservation. The n-body phase space describing the possible final states for a decay to n daughters is defined as:

$$d\Phi(P; p_1, p_2, ...) = \delta^4(P - (\sum_i p_i)) \prod_j \frac{d^3 p_j}{(2\pi)^3 2E_j}. \tag{2.2}$$

For reasons that will become clear in a few sections, in this thesis we will be dealing "inclusive" quantities, meaning that we will be measuring quantities for processes that sum over several final states arising from a particlular initial state. This is contrasted with "exclusive" quantities, which are quantities that are measured for a transitions from a specific initial state to a specific final state. For inclusive processes, the number of particles in the final state is not well defined. This ruins our nice, clean separation of kinematics and dynamics. For our calculation of the inclusive rate for $B \to X\ell\nu$, the sum over the final state particles and their phase space will be accounted for in the calculation of the matrix element. The differential decay rate is then written as

$$d\Gamma = \frac{d^3p_\ell}{(2\pi)^3 2E_\ell}\frac{d^3p_\nu}{(2\pi)^3 2E_\nu}\sum_X \sum_{\text{lepton spins}} \frac{(2\pi)^4}{2M_B}|\mathcal{M}|^2\delta^4(p_B - (p_\ell + p_\nu) - p_X). \tag{2.3}$$

where $\sum_X$ is the sum over all the possible hadronic finals states, as well as the integral over the phase space of those states.

Making the approximation that the lepton masses are negligible, we can write the differential elements as $d^3p = E^2 dE d\phi d(\cos\theta)$. Three of the four angles are just the orientation of the decay, which contains nothing interesting about the decay in the rest frame of the spinless B meson. Therefore, we can just integrate over these angles, giving us a factor of $2(2\pi)^2$. The one interesting angle is that between the lepton and neutrino directions, $\cos\theta_{\ell\nu}$. Our differential decay rate is now

$$d\Gamma = \sum_X \sum_{\text{lepton spins}} \frac{|\mathcal{M}|^2}{4M_B} E_\ell dE_\ell E_\nu de_\nu d(\cos\theta_{\ell\nu})\delta^4(p_B - (p_\ell + p_\nu) - p_X). \tag{2.4}$$

Here it is convenient to introduce a new variable $q \equiv p_\ell + p_\nu$. Form this definition, it is obvious that q^2 is the invariant mass of the virtual W exchanged. For massless

leptons, $q^2 = 2E_\ell E_\nu(1 - \cos\theta_{\ell\nu})$. The differential decay rate can now be written as

$$\frac{d\Gamma}{dq^2 dE_\ell dE_\nu} = \sum_X \sum_{\text{lepton spins}} \frac{|\mathcal{M}|^2}{8M_B} \delta^4(p_B - (p_\ell + p_\nu) - p_X). \tag{2.5}$$

2.1.2 The Matrix Element

We now turn our attention to the matrix element $\mathcal{M}$. The general expression for a matrix element for a process that is governed by a Hamiltonian $\mathcal{H}$ is

$$\mathcal{M} = \langle f|\mathcal{H}|i\rangle \tag{2.6}$$

with i and f describing the initial and final states respectively. For the weak decay $b \to q\ell\nu$, we have

$$\mathcal{H}_w = \frac{4G_F V_{qb}}{\sqrt{2}} L^\mu H_\mu, \tag{2.7}$$

where L^μ and H_μ are the leptonic and hadronic currents, respectively. They are given by the expressions

$$L^\mu = \bar{\ell}\gamma^\mu(1 - \gamma_5)\nu \tag{2.8}$$

$$H_\mu = \bar{q}\gamma_\mu(1 - \gamma_5)b. \tag{2.9}$$

Inserting this Hamiltonian into our expression for the differential decay rate gives

$$\frac{d\Gamma}{dq^2 dE_\ell dE_\nu} = \sum_X \sum_{\text{lepton spins}} \frac{|\langle X\ell\nu|\mathcal{H}_w|B\rangle|^2}{8M_B} \delta^4(p_B - (p_\ell + p_\nu) - p_X). \tag{2.10}$$

Since leptons do not interact strongly, the weak matrix element $\langle x\ell\nu|\mathcal{H}_w|B\rangle$ in Eq. [2.10] can be approximately factored into a leptonic matrix element $\langle \ell\nu|L^\mu|0\rangle$ and a hadronic matrix element $\langle X|H_\mu|B\rangle$. This is an approximation because, while the

leptons do not interact strongly, they do interact with the quarks in the hadron via electroweak processes, and corrections to this result will occur at order of G_F and α_{EM}. These corrections are small and will be neglected for this discussion.

With the factorization approximation, the differential decay rate becomes

$$\begin{aligned}\frac{d\Gamma}{dq^2 dE_\ell dE_\nu} &= \sum_X \sum_{\text{lepton spins}} \frac{G_F^2 |V_{qb}|^2}{2} \frac{|\langle \ell\nu | L^\mu | 0\rangle \langle X | H_\mu | B\rangle|^2}{8M_B} (2\pi)^3 \delta^4(p_B - (p_\ell + p_\nu) - p_X) \\ &= \frac{G_F^2 |V_{qb}|^2}{(2\pi)^3} L^{\alpha\beta} W_{\alpha\beta} \end{aligned} \tag{2.11}$$

The quantities $L^{\alpha\beta}$ and $W_{\alpha\beta}$ in Eq. 2.11 are called, respectively, the leptonic tensor and the hadronic tensor.

The leptonic tensor is defined by

$$L^{\alpha\beta} = \sum_{\text{lepton spins}} \langle 0 | L^{\dagger\alpha} | \ell\nu\rangle \langle \ell\nu | L^\beta | 0\rangle \tag{2.12}$$

and is calculable as an expansion in powers of the coupling constant. It is given by [1]

$$L^{\alpha\beta} = 2(p^\alpha k^\beta + p^\beta k^\alpha - g^{\alpha\beta} p \cdot k - i\epsilon^{\eta\beta\lambda\alpha} p_\eta k_\lambda). \tag{2.13}$$

The hadronic tensor is more complicated. It is defined by

$$W_{\alpha\beta} = \sum_X \frac{(2\pi)^3 \delta^4(p_B - q - p_X)}{2M_B} \langle B | H_\alpha^\dagger | X\rangle \langle X | H_\beta | B\rangle. \tag{2.14}$$

This is a second-rank tensor that depends on the momentum of the B meson p_B and the momentum of the daughter hadronic system p_X.

[1] In Eq. [2.13] I have changed notation, replacing $p_\ell \to p$ and $p_\nu \to k$, to prevent confusion between momentum labels and Lorentz indices.

2.1.3 The Free-Quark Calculation of the Rate

The hadronic tensor is difficult to calculate because it involves nonperturbative strong interactions. One way around this difficulty is to simply ignore it and treat the b quark as if it is a free particle that does not interact with the "spectator" quark q_{sp} in the hadron. With this simplifying assumption, the expression for $H_{\alpha\beta}$ takes a form identical to that of $L^{\alpha\beta}$. Using this free-quark assumption and integrating over q^2 and E_ν, the expression for the differential decay rate for $b \to x\ell\nu$ becomes

$$\frac{d\Gamma}{dx} = \frac{G_F^2 m_b^5}{192\pi^3}|V_{qb}|^2 w_0(x,y) \tag{2.15}$$

where $x = 2E_\ell/m_b$ and $y = m_q/m_b$. The physical limits of x are $0 \leq x \leq 1 - y^2$. The function $w_0(x,y)$ is the contains both weak interaction and phase-space information, and is given by

$$w_0(x,y) = \frac{2x^2(1-y^2-x)^2}{(1-x)^3}[(1-x)(3-2x) + y^2(3-x)]. \tag{2.16}$$

Integrating over all possible x gives

$$\Gamma = \frac{G_F^2 m_b^5}{192\pi^3}|V_{qb}|^2 \Phi(y), \tag{2.17}$$

where $\Phi(y) = \int_{x_m}^{x_M} w_0(x,y)$ is about 1 for $b \to u\ell\nu$ decays (reflecting the relativly small masses of the final state particles in comparison to m_b) and about 0.5 for $b \to c\ell\nu$ decays.

This result for the rate is very similar to the well-known expression for muon decay $\mu \to e\nu_e\nu_\mu$. Since there are no quarks involved in the initial or final states, muon decay is one of the cleanest weak decay processes, both theoretically and experimentally.

The rate for muon decay is given in terms of the mass of the muon m_μ by the expression

$$\Gamma_\mu = \frac{G_F^2 m_\mu^5}{192\pi^3}. \tag{2.18}$$

While the free-quark assumption makes a rough calculation of the rate relatively easy, it neglects QCD effects which are not small, and we need a method for obtaining the hadronic tensor that accounts for them. Because it involves non-perturbative physics, the hadronic tensor cannot be written as an expansion only in powers of the coupling constant, unlike the leptonic current. To get an appropriate expression for the hadronic current, we turn to the Operator Product Expansion (OPE) and Heavy Quark Effective Theory (HQET).

2.2 The Operator Product Expansion

The OPE is a short-distance approximation where the product of two operators separated by a short distance x is expanded in terms of local operators and coefficients dependent on x. We will use it to reorganize the expression for the hadronic tensor defined in Eq. 2.14 into something more tractable:

$$W_{\alpha\beta} = \sum_X \frac{(2\pi)^3 \delta^4(p_B - q - p_X)}{2M_B} \langle B|H_\alpha^\dagger|X\rangle\langle X|H_\beta|B\rangle. \tag{2.19}$$

The steps in applying the OPE are shown schematically in Fig. 2.3.

The first step is to perform the summation over the complete set of states in Eq. 2.14 by using $\sum_X = |X\rangle\langle X| = 1$. This removes the dependence on the structure of the final hadron state X from the tensor.

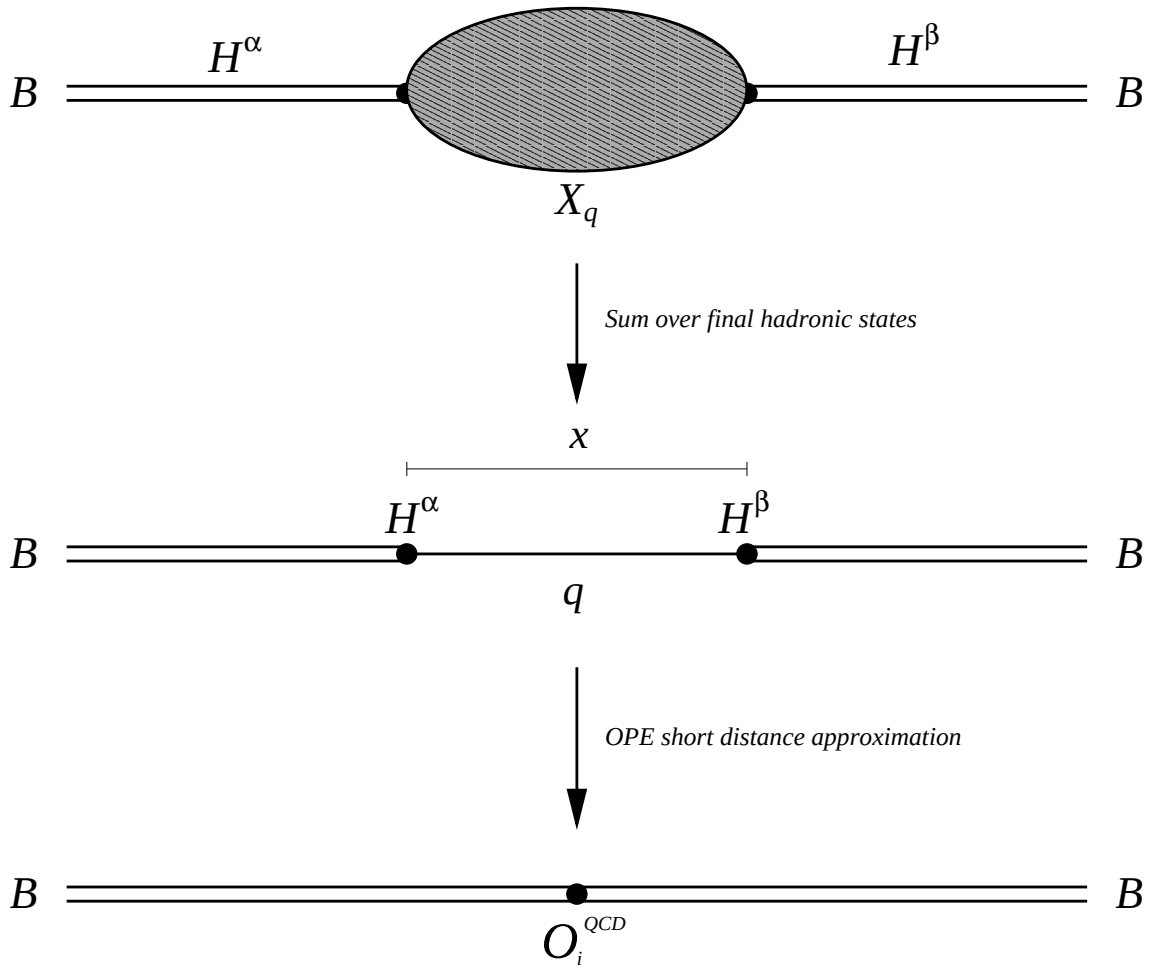

Figure 2.3: Schematic of the steps of applying the Operator Product Expansion.

The next step is to apply the OPE. The OPE makes the approximation that the product of two operators separated by a short-distance x can be expanded in terms of local operators and coefficients dependent on x. For our two hadronic currents, we can write

$$H^{\alpha}(0)H^{\beta}(x) = \sum_i \mathcal{C}_i^{\alpha\beta}\mathcal{O}_i^{QCD}(0), \tag{2.20}$$

where $\mathcal{O}_i^{QCD}$ are local QCD operators, and $\mathcal{C}_i^{\alpha\beta}(x)$ are the so-called Wilson coefficients. The Wilson coefficients contains both phase space information and the terms from the short-range perturbative QCD expansion in α_s, and and have been calculated by several authors [3, 4, 5].

The hadronic tensor now looks like

$$W_{\alpha\beta} = \sum_i \mathcal{C}_i^{\alpha\beta}\langle b|\mathcal{O}_i^{QCD}|B\rangle. \tag{2.21}$$

The operators $\mathcal{O}_i^{QCD}$ are generally not calculable as they contain non-perturbative physics. However. we can gain some insight into their structure in the case of hadrons containing heavy quarks by using HQET.

2.2.1 Quark-Hadron Duality

With the OPE, we have been able to separate the perturbative QCD corrections from the non-perturbative corrections. There is a price to pay for this ability. The short-distance approximation made in the OPE means that it cannot predict long-distance effects, such as what form the final hadronic states X will take (indeed, we summed them out of the expression). The OPE allows for calculations to be made in terms of quarks. Any comparison of the predictions with experiment must be made with

"inclusive" quantities, where a summation over all possible final states is performed. However, we live in an "exclusive" world, where we observe $B \to (D, D^*, D^{**}$, or $DX)\ell\nu$ rather than $b \to c\ell\nu$. The assumption that a sufficient sum over exclusive final states is equivalent to an inclusive view is called *quark-hadron duality*. The theoretical uncertainty associated with this assumption is not well uncerstood, and whether or not a particular measurement or calculation is "inclusive enough" must be evaluated on a case-by-case basis.

2.3 Heavy Quark Effective Theory

Heavy quarks behave differently in the strong interactions inside hadrons than light quarks because they are *heavy*. Since the masses of the b quark and the c quark (~ 4.6 GeV/c^2 and ~ 1.2 GeV/c^2, respectively) are much larger than Λ_{QCD}, the creation of $b\bar{b}$ or $c\bar{c}$ pairs in the brown muck is greatly suppressed. Also, since the momentum exchanges in hadrons due to strong interactions are of the order Λ_{QCD}, the change in velocity of a heavy quark during such interactions is about Λ_{QCD}/m_q. In the infinite-quark-mass limit, the heavy quark's velocity is conserved. In this limit, different flavors of heavy quarks behave identically; one flavor of heavy quark can be replaced by another flavor of heavy quark of the same color and the strong interactions with the light degrees of freedom will not be affected. This is known as the *heavy quark flavor symmetry*. The heavy quark can be viewed as a static source of a color field, with the light degrees of freedom orbiting it in the hadron. Indeed, an analogy can be drawn between a hadron containing a heavy quark and an atom. In atomic physics,

the nucleus of an atom is viewed as a static source of the electromagnetic field. One can replace the nucleus with another nucleus with the same charge and different mass, and still leave the electrons unaffected. There is also an analogous situation to hyperfine splitting in hadron with a heavy quark. The strong force couples to the spin of a quark via the chromomagnetic moment of the quark. Since the gyromagnetic ratio is proportional to $1/m_q$, the strong force decouples from the spin of a heavy quark in the infinite-mass limit. This is known as the *heavy quark spin symmetry*. Of course, both symmetries only hold in the infinite mass limit, and we will need to make corrections of $\mathcal{O}(\Lambda_{QCD}/m_b)$.

Using these symmetries, we can construct an "effective" theory of the dynamics of hadrons containing heavy quarks. Effective theories, rather than trying to calculate everything, incorporate only those degrees of freedom that matter in a more or less ad hoc manner. In this spirit, we will develop an effective theory of QCD for heavy quarks in hadrons by constructing a double power series expansion around small parameters; one expansion in powers of α_s to account for the perturbative QCD processes, and the other in powers of $1/m_b$ to account for non-perturbative effects.

2.3.1 The HQET Hamiltonian

The derivation here will follow the discussion presented in Ref. [6]. The key to constructing the effective Hamiltonian is to recognize that, due to its mass, the heavy quark Q in a hadron H_Q moves with more or less the hadron's velocity v. The

expression for the momentum of Q then looks like

$$p_Q = m_{H_Q} v + k, \tag{2.22}$$

where k is the "residual momentum", and is of order Λ_{QCD}. In the rest frame of H_Q, Q's momentum is entirely residual, and the motion of Q becomes non-relativistic in the limit $\Lambda_{QCD}/m_Q \to 0$. We can therefore express the Hamiltonian for a hadron containing a non-relativistic heavy quark as[2] :

$$\mathcal{H}_{H_Q} = m_Q + \mathcal{H}_Q + \mathcal{H}_{light}, \tag{2.23}$$

where $\mathcal{H}_{light}$ is the Hamiltonian of the light degrees of freedom, and $\mathcal{H}_Q$ is the Pauli Hamiltonian for a non-relativistic spinor particle:

$$\mathcal{H}_Q = \frac{(\vec{\sigma} \cdot \vec{\pi})^2}{2m_Q}. \tag{2.24}$$

Here $\vec{\pi}$ is the kinetic momentum of the heavy quark $\vec{\pi} = \vec{k} - g\vec{A}$, and $\vec{A}$ is the gluon-field vector potential.

Using the commutation relations for $\vec{\pi}$ and the properties of the Pauli matrices, the Pauli term can be rewritten as:

$$(\vec{\sigma} \cdot \vec{\pi})^2 = \vec{\pi}^2 - g\vec{\sigma} \cdot \vec{B},$$

where $\vec{B}$ is the chromo-magnetic field at the location of the heavy quark. Equation (2.23) can now be written in a most suggestive way:

$$\mathcal{H}_{H_Q} = m_Q + \frac{\vec{\pi}^2}{2m_Q} - \frac{g\vec{\sigma} \cdot \vec{B}}{2m_Q} + \mathcal{H}_{light}. \tag{2.25}$$

[2] A fully relativistic calculation has been done in numerous places [7, 8, 9], and gives the same results to $\mathcal{O}(1/m_Q)$.

2.3.2 HQET parameters

What has appeared here in Eq. [2.25] is just what we needed: an expansion in powers of a small parameter, in this case $1/m_Q$. The first term in is the only term that remains at the infinite mass limit, and the $\mathcal{O}(1/m_Q)$ terms are corrections for the fact that the heavy quark is not infinitely massive. The first $\mathcal{O}(1/m_Q)$ term corresponds to the kinetic energy of the heavy quark, and the second term corresponds to the chromomagnetic coupling of the heavy quark and the light degrees of freedom. The $\mathcal{H}_{light}$ describes the QCD interactions of the light degrees of freedom with themselves.

The expectation values of the operators in the HQET Hamiltonian in Eq. 2.25 describe physical properties of a hadron containing a heavy quark, but since they involve non-perturbative QCD processes, they cannot be calculated. Instead, we define a set of parameters that need to be experimentally determined. The lowest order of these, $\overline{\Lambda}$, is defined as

$$\overline{\Lambda} \equiv \langle H_Q | \mathcal{H}_{light} | H_Q \rangle, \tag{2.26}$$

and can be interpreted as the contribution of the light degrees of freedom to the hadron mass. The first $\mathcal{O}(1/m_Q)$ term, μ_π^2, is defined as

$$\mu_\pi^2 \equiv \langle H_Q | \pi^2 | H_Q \rangle, \tag{2.27}$$

and corresponds to the kinetic energy of the heavy quark, related to the "Fermi momentum" of the heavy quark inside the hadron. The other $\mathcal{O}(1/m_Q)$ term, μ_g^2, is defined as

$$\mu_g^2 \equiv \langle H_Q | g\vec{\sigma} \cdot \vec{B} | H_Q \rangle. \tag{2.28}$$

and corresponds to the chromomagnetic coupling of the heavy quark and the light degrees of freedom, and is spin-dependent.

The two terms μ_π^2 and μ_g^2 are often written in the parameterized form:

$$\mu_\pi^2 - \mu_g^2 = -\lambda_1 + 2\left[J(J+1) - \frac{3}{2}\right]\lambda_2, \tag{2.29}$$

with J being the spin of the hadron. The nomenclature of these new parameters will be used in what follows. The expansion has been calculated to one order higher than the derivation presented here. This adds six new expansion parameters: $\rho_1, \rho_2, \mathcal{T}_1, \mathcal{T}_2, \mathcal{T}_3$, and $\mathcal{T}_4$.

We can make a rough estimation of the size of the non-perturbative parameters due to the fact that they arise from strong interactions; each of these parameters is expected to be of order Λ_{QCD}^n, where n is the order of the dimension on the parameter. We can see from Eq. 2.30 that the dimension of $\overline{\Lambda}$ is GeV, λ_1 and λ_2 are GeV^2, and the dimensions of the ρ's and $\mathcal{T}$ are GeV^3. Because λ_2 is easily measured, one can write an expression for observables of semileptonic B decay (see Sect. 2.4.2) as a polynomial that is dependent on $\overline{\Lambda}$ and λ_1; using $(0 \pm 0.5 \text{ GeV})^3$ as an estimate of the ρ's and $\mathcal{T}$'s. In this way, a moment will define a band in $\overline{\Lambda} - \lambda_1$ space. The intersection of two of these bands will yield unique values of $\overline{\Lambda}$ and λ_1. We can also use more than two moments in an attempt to overconstrain the theoretical predictions, as a test of the quark-hadron duality assumption made in constructing the OPE.

Using the Hamiltonian from Eq. [2.25] and these HQET expansion parameters, we get an expression for the mass of a hadron H_Q containing a heavy quark to $\mathcal{O}(1/m_Q)$:

$$M_{H_Q} = m_Q + \overline{\Lambda} - \frac{\lambda_1}{2m_Q} + \frac{J(J+1) - \frac{3}{2}}{m_Q}\lambda_2 + \mathcal{O}(1/m_Q^2) \tag{2.30}$$

2.4 Measurements of HQET

With an expression for the hadronic tensor in the OPE framework, and the HQET expansion parameterizing the troubling non-perturbative aspects QCD in terms of expectation values of local operators, the final step is to replace the full QCD, represented by the operators $\mathcal{O}_i^{QCD}$ in Eq. 2.21, with our effective theory of QCD for heavy quarks by simply swapping the HQET operators into the OPE expansion.

The OPE allows the calculation of the fully-differential decay rate in HQET. However, as mentioned in Sect. 2.2.1, quark-hadron duality demands that we use inclusive quantities to compare HQET predictions to experimental data. Therefore, we must use measured quantities with enough phase space and final state modes.

2.4.1 The Semileptonic Branching Ratio

One of the measurements we make in this thesis is the semileptonic branching ratio of the B meson. The branching ratio is related to the semileptonic width by $\mathcal{B}_{SL} = \tau_B \Gamma_{SL}$, where $\tau_B = 1.6$ ps is the average lifetime of the B meson [10]. We can then use the measured branching ratio to extract $|V_{cb}|$ from the data; we need simply to integrate Eq. [2.11] using the hadronic tensor containing the HQET operators over

all the kinematic variables to get the expression for the total rate [11]:

$$\Gamma(B \to X_c \ell \nu) = \frac{G_F^2 |V_{cb}|^2 \bar{m}_B^5}{192\pi^3} \Bigg[0.370 - 0.115\overline{\Lambda} - 0.012\overline{\Lambda}^2 + 0.0\overline{\Lambda}^3$$
$$- 0.04\lambda_1 - 0.10\lambda_2 - 0.01\lambda_1\overline{\Lambda} + 0.02\lambda_2\overline{\Lambda} \tag{2.31}$$
$$- 0.02\rho_1 + 0.02\rho_2 - 0.02\mathcal{T}_1 + 0.0\mathcal{T}_2$$
$$- 0.03\mathcal{T}_3 - 0.02\mathcal{T}_4 - 0.040\epsilon - 0.022\epsilon_{BLM}^2 + 0.007\epsilon\overline{\Lambda} \Bigg],$$

Here we use the spin-averaged meson mass $\bar{m}_{H_Q} = \frac{3m^*_{H_Q} + m_{H_Q}}{4}$ as an approximation for the quark mass, an approximation that is good to the extent that $\overline{\Lambda}/m_Q$ is small.

Before Eq. 2.31 can be used, the values of the non-perturbative expansion parameters must be determined. Since they contain the non-perturbative QCD corrections, they cannot be calculated and must be measured. The easiest to measure is λ_2. From Eq. 2.30, we can get an expression for λ_2 in terms of the mass splitting of the pseudoscalar state H_Q and vector state H_Q^*:

$$\lambda_2 = (m_{H_Q^*} - m_{H_Q})\frac{m_Q}{2} = (m_{H_Q^*} - m_{H_Q})\frac{\bar{m}_{H_Q}}{2}. \tag{2.32}$$

Using PDG values [10], we obtain $\lambda_2 = 0.1255 \pm 0.001$ GeV^2. The other expansion parameters are not so easily obtained; we will use measurements of the moments of different kinematic distributions to get these values.

2.4.2 Moments

The remaining HQET parameters can be determined with a battery of moments measurements. In general, a moment is given by the definition

$$\langle M \rangle = \int M(\vec{x}) d\vec{x} \frac{d\Gamma}{d\vec{x}}. \tag{2.33}$$

Expressions for moments are predicted by HQET, and are usually expressed as polynomials of the non-perturbative parameters:

$$\begin{aligned}
\langle M \rangle &= M^{(1)} + M^{(2)}\Lambda + M^{(3)}\Lambda^2 + M^{(4)}\Lambda^3 \\
&+ M^{(5)}\lambda_1 + M^{(6)}\lambda_2 + M^{(7)}\lambda_1\Lambda + M^{(8)}\lambda_2\Lambda \\
&+ M^{(9)}\rho_1 + M^{(10)}\rho_2 + M^{(11)}\mathcal{T}_1 + M^{(11)}\mathcal{T}_1 \\
&+ M^{(12)}\mathcal{T}_2 + M^{(13)}\mathcal{T}_3 + M^{(14)}\mathcal{T}_4 + M^{(15)}\epsilon \\
&+ M^{(16)}\epsilon^2_{BLM} + M^{(17)}\epsilon\Lambda,
\end{aligned}$$

where the M^i coefficients are numerical constants given by the HQET/OPE methods described above, and ϵ and ϵ^2_{BLM} are used to denote the terms dependent on α_s in the perturbative expansion, and are set equal to one.

The three main types of moments that have been measured to date are

- the moments of the lepton-energy spectrum in $B \to X_c \ell \nu$ decays [12, 13],
- the moments of the hadronic-mass-squared distribution in $B \to X_c \ell \nu$ decays [14, 15, 16], and
- the moments of the photon-energy spectrum from $b \to s\gamma$ decays [17, 18].

Each has its own experimental limitations. Meaasurements of the lepton-energy spectrum are able to cover a large amount of phase space; the measurement presented in this thesis measures the portion of the energy spectrum where $E_\ell \geq 600$ MeV, or about 94% of the total spectrum. Hadronic mass moments are tougher to measure, as they demand reconstruction of the undetected neutrino, which means that one must detect all the other particles in the event and attribute the missing energy and momentum to the neutrino. Measurements of hadronic mass moments have been made for decays with *lepton energy* greater than 1.0 GeV. The photon-energy moments of the rare decay $B \to X_s\gamma$ are very desirable because they are two-body decays; in the infinite quark mass limit, the photons from this process would be monochromatic. The extent that the photon-energy spectrum is smeared depends on the Fermi motion of the b-quark inside the meson. Thus the mean of the photon-energy spectrum (the first moment) gives a measurement of $\overline{\Lambda}$. This measurement, however, is plagued by the fact that this decay is relatively rare; overwhelming backgrounds have limited measuements of the spectrum to $E_\gamma \geq 1.8$ GeV. Several authors have calculated moments expressions for "truncated" spectra [11, 19] to reflect these experimental limitations. These expressions are usually presented in the form of Eq. 2.34 with large tables of M^i's calculated for various minimum energy cuts.

In this thesis, we will measure the semileptonic branching ratio of the B meson, and several moments of the lepton-energy spectrum at various minimum energy cuts between 0.6 and 1.5 GeV.

CHAPTER 3

CESR and CLEO

Our source of subatomic particles is the Cornell Electron Storage Ring, or CESR (pronounced "Caesar"). CESR collides electrons (e^-) and their antimatter partners, positrons (e^+), at a center of mass energy of about 10 GeV. When an electron and a positron collide, they annihilate in a state of pure energy, a virtual photon. That virtual photon then turns into another fermion-antifermion pair, whether it be leptons or, more interestingly, a quark-antiquark pair.

The CLEO detector (named for another who is historically coupled to a CESR) is used to identify and measure the particles produced by CESR in an effort to better understand the fundamental constituents of matter and the laws governing their interactions. This chapter will describe CESR and the two generations of CLEO detectors used to collect the data used for this thesis.

A note about terminology: I use `teletype` fonts for any CLEO-specific variables or software packages. For the edification of the non-CLEO reader, these quantities are defined when they are first introduced.

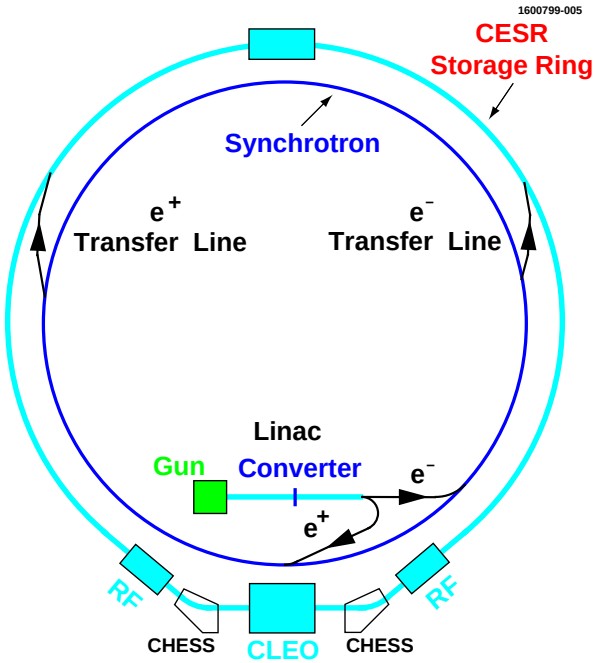

Figure 3.1: The colliding-beam facility at Cornell.

3.1 CESR - The Cornell Electron Storage Ring

Forty feet under Cornell University's track-and-field facility lies the Cornell Electron Storage Ring, a symmetric electron-positron collider 768 meters in circumference[20]. From 1979 to 2003, electron and positron bunches were made to collide at center-of-mass energies from 9 to 12 GeV; most of this time was spent in the vicinity of 10.58 GeV. In early 2003, CESR was retooled to run efficiently at energies as low as 3 GeV. The data for this thesis was collected between 1990 and 1999. The storage ring itself is part of a larger facility shown schematically in Fig. 3.1.

We must first begin by creating the beams of electrons and positrons with a linear accelerator (linac). Electrons are produced by heating a filament, and then collected,

collimated, bunched, and accelerated to an energy of about 300 MeV in a 30 meter long vacuum pipe by a series of radio-frequency (RF) cavities. For positron production, electrons from the filament are accelerated to 150 MeV before being intercepted by a tungsten target, producing a spray of electrons, positrons, and photons. The positrons are selected by their charge and mass with a magnetic field, and then accelerated in the remainder of the linac to energies of about 200 MeV.

The electron and positron bunches from the linac are transferred to the synchrotron, where they are accelerated to their ultimate energies. The synchrotron is an evacuated ring that mostly consists of the 192 three-meter sections of bending and focusing magnets. At four places around the ring, particles pass through three-meter-long accelerating cavities. It takes about 4000 revolutions, or about 1/100 seconds, for particles to reach their maximum energy in the synchrotron. They are then ready for transfer into CESR.

Bunches of particles in CESR are confined in stable orbits by magnets. Electron and positron bunches counter-circulate in the storage ring at the same time, and are kept apart by magnets and electrostatic separators. Being charged, the electrons and positrons emit *synchrotron radiation* as they circulate, about 1.2 MeV per revolution. This energy is replaced by several RF cavities. Bunches are steered into one another at the interaction point (IP) on the south end of the ring and directly in the center of CLEO.

The most useful metric of an accelerator's instantaneous performance is a quantity called the *luminosity*. It is defined conceptually as

$$\mathcal{L} \equiv nf\frac{N_{e^+}N_{e^-}}{A}, \tag{3.1}$$

where n is the number of electron (or positron) bunches in the beam, N_{e^+} and N_{e^-} are the numbers of electrons and positrons in each bunch f is the orbital frequency, and A is the cross-sectional area of the beams. The highest luminosity achieved during the collection of the data in this thesis was 8×10^{32} cm^{2}s^{-1}.

The instantaneous luminosity and the cross-section σ for a particular process determine the rate at which that process occurs. The number of events N is given by

$$N = \sigma \left[\int \mathcal{L} dt \right]. \tag{3.2}$$

where the quantity in brackets is the *integrated luminosity.* Fig 3.2 shows the yearly integrated luminosity generated by CESR from 1985 to mid-2001. Dips in 1995 and 1999 correspond to extended shutdowns for major upgrades to both CESR and CLEO.

Here σ is the *cross-section* of the process in question, and is measured in *barns* . Fig. 3.3 shows the total cross-section for $e^+e^- \rightarrow$ *hadrons* at center-of-mass energies around 10 GeV.[1] The enhancements in this plot are the Upsilon (Υ) resonances, bound states of a bottom quark (b) and an anti-bottom quark ($\bar{b}$). At the 10.58 GeV resonance, the total hadronic cross-section is about 4 nb. About one-fourth of this is due to production of the $\Upsilon(4S)$ and the rest from the *continuum* production of lighter quark-antiquark pairs. The $\Upsilon(4S)$ is broader the the lower Υ resonances because it has just enough energy to decay via the strong force to a pair of B mesons, each with a mass of about 5.28 GeV/c^2. The data sample used for this thesis consists of an integrated luminosity of 9.13 fb^{-1} at a center-of-mass energy near 10.58 GeV (hereafter referred to as *on-resonance* or simply "ON"). This corresponds to a sample

[1]The cross-section has the dimensions of area and is typically measured in *barns* ($1\ b = 10^{-24}\ cm^2$) or multiples thereof.

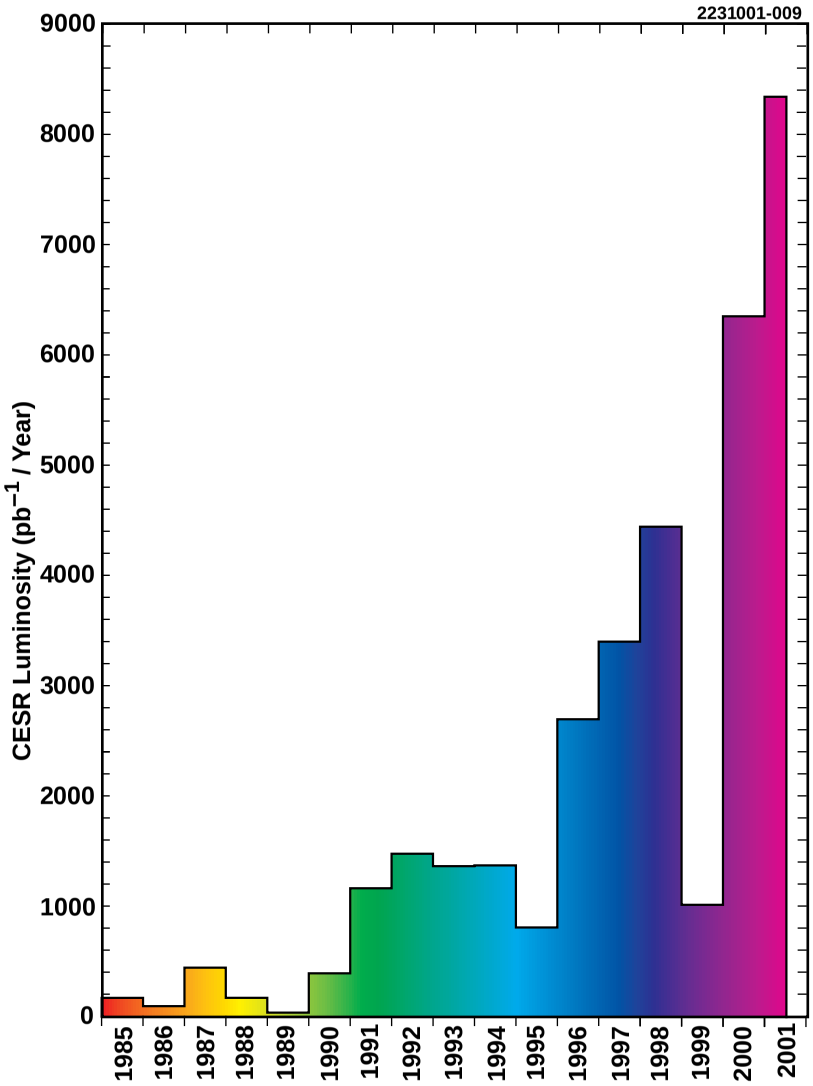

Figure 3.2: The annual integrated lumonisity from CESR.

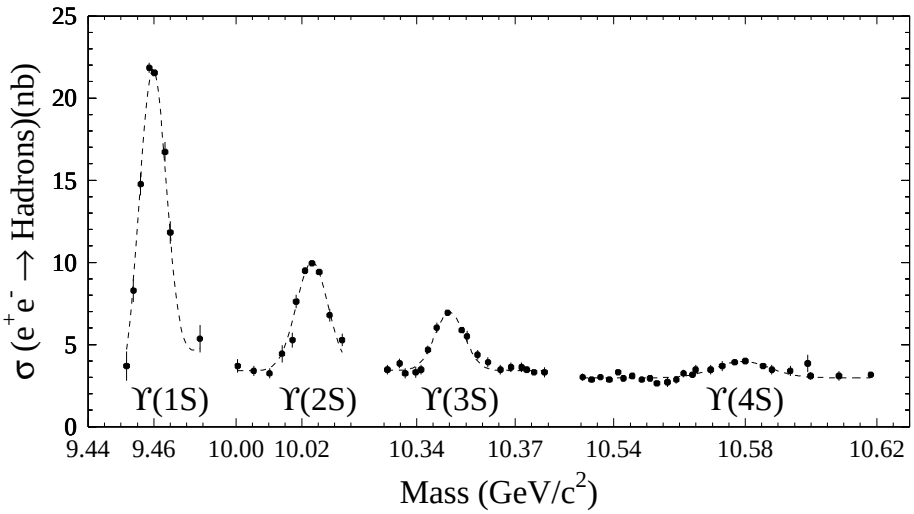

Figure 3.3: The hadronic cross-section in the Upsilon region.

of about 9.7 million $B\bar{B}$ events. An additional 4.35 fb^{-1} was collected about 60 MeV below the $\Upsilon(4S)$ (called *off-resonance* or "OFF"), providing a sample useful for estimating backgrounds to B physics.

3.2 The CLEO Detector

Observing the kinds of particles created from electron-positron annihilations, how often certain particles appear, how long they live, and their kinematic properties gives us insights into the natural laws that govern their behavior. To reconstruct the history of these events, we must detect and measure as many of the particles and their properties as possible. These properties include a particle's energy and momentum at the vertex, its electric charge, its mass, and its trajectory. To this end, the CLEO collaboration has built a general purpose detector [21, 22] around

CESR's interaction point, covering nearly the entire 4π of the solid angle with several types of instrumentation, each able to measure some property of a particle with good accuracy.

The basis of all particle detectors is the behavior of subatomic particles when they interact with matter. Particles entering a chunk of matter encounter an aggregate of electrons and nuclei, and can interact with either the atoms as a whole or their individual parts. For example, an alpha particle entering gold foil can scatter off a nucleus via the strong force, collide electromagnetically with an atomic electrons, or be absorbed in a nuclear reaction to produce other types of radiation. Similarly, we are able to distinguish different particle species by how they interact with the material in CLEO's subdetectors.

Particles leaving the IP encounter the parts of CLEO in the following order: the beryllium beam pipe, the tracking system, the time-of-flight counters, the electromagnetic crystal calorimeter, the 1.5-Tesla superconducting solenoid electromagnet, and the muon identification system. Between 1990 and 1999, the CLEO detector existed in two different configurations, CLEO II (1990-1995) and CLEO II.V (1995-1999). A side view of CLEO II.V is shown in Fig. 3.4. The main difference was that the innermost wire chamber of the tracking system in CLEO II was removed and replaced in CLEO II.V by silicon strips to provide better vertex resolution (see Sect. 3.2.2). Also, the gas filling in the main drift chamber (Sect. 3.2.3) was changed from an argon/ethane mixture to a helium/propane mix.

In the following sections, we will describe these sub-detectors in the order that particles encounter them. To facilitate this discussion, the following coordinate system

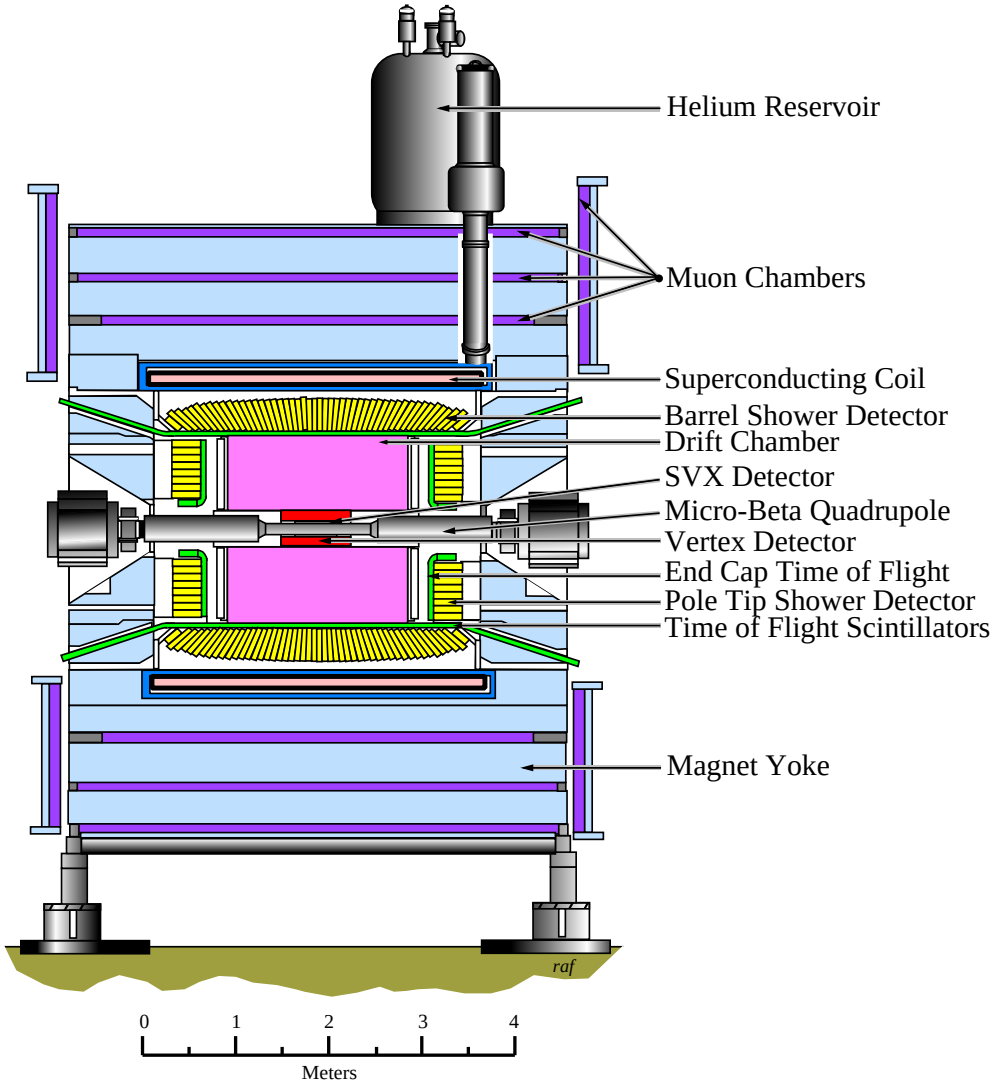

Figure 3.4: The side view of the CLEO II.V detector

will be used: the origin is positioned at CESR's IP in the center of CLEO, the z-axis points along the beam line in the direction of travel of the positron beam (west), the y-axis points upward, and the x-axis points outward from the center of CESR (south). Points in the $x - y$ plane are determined by their radial distance r from the beam line and the angle ϕ off the y-axis. The polar angle θ is defined off the z-axis. In our analysis, we mostly restrict ourselves to the best-performing region of CLEO, the section in the region $|cos\theta| \leq 0.7071$, called the *good barrel* region. In describing the detector, we will also refer to the *endcap* regions of $|cos\theta| \geq 0.81$, and the *bad barrel* regions in between the endcap and the good barrel.

3.2.1 A Few Words About Tracking

Upon exiting the beam pipe, a charged particle encounters a set of devices designed to measure its trajectory and momentum. In CLEO II, this consisted of three concentric drift chambers. A drift chamber uses *sense wires* held at high positive voltage suspended in a mixture of gases. *Field wires* or a tube of conducting material at negative high voltage form a *cell* around each sense wire. Thus an electric field of known shape and strength is established in the cell. As a charged particle travels through a cell it knocks electrons off, or ionizes, the gas molecules. These ionized electrons then drift toward the sense wire of the cell under the influence of the cell's electric field. The strength of the electric field increases as an electron approached the sense wire. Very near the wire, the approaching electron gains enough energy to itself ionize gas molecules as it passes, creating an avalanche of electrons to be collected by the sense wire. This avalanche produces a measurable electronic pulse on the sense

wire known as a *hit*. We resolve the trajectory of the particle through the cell even further by measuring the time of arrival of the avalanche, thus getting an estimate of the particle's distance of closest approach to the sense wire. Combining information from multiple staggered cells, the particle's trajectory through the wire chamber can be precisely measured. Hits are later grouped by software into combinations called *tracks*.

The tracking layers are inside a 1.5-Tesla magnetic field oriented in the z direction. Therefore, charged particles traveling through them follow a helical path. A measurement of the particle's transverse momentum $p_\perp$ is made from the helix's radius of curvature a in the r-ϕ plane with the relation

$$p_\perp = qBa \tag{3.3}$$

where q is the magnitude of the particle's electric charge and B is the magnitude of the magnetic field. With the particle's polar angle θ, $p_\perp$ provides a measurement of the particle's total momentum. Also, the direction of curvature indicates the sign of the particle's charge.

3.2.2 The Inner Tracking System: PT, VD, and SVX

The innermost layer of CLEO II's tracking system was known as the Precision Tracker (PT), and consisted of six layers of aluminized mylar tubes with a single sense wire strung in each tube. The tubes were mounted directly on the beam pipe in a hexagonal close-pack configuration, as shown in Fig. 3.5. The tubes varied from 4.5 mm to 7.5 mm in diameter and provided the smallest cell size of all the drift chambers. The PT

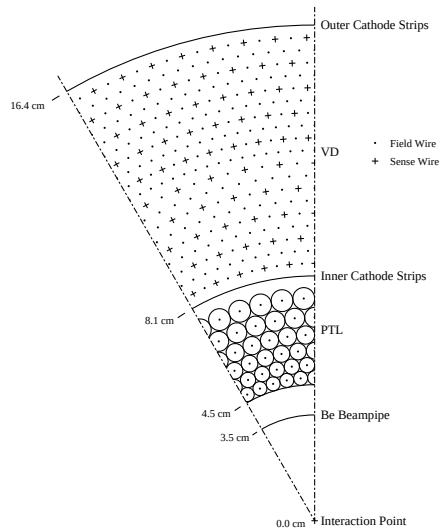

Figure 3.5: Layout of the PT and VD in CLEO II

provided an average r-ϕ resolution of about 100 μm.

Surrounding the PT in CLEO II was a multi-wire drift chamber with small wire spacing, called the Vertex Detector (VD) and shown in Fig. 3.5. The VD had ten layers of cells; each cell formed by a hexagonal arrangement of field wires surrounding a sense wire. Hits on the wires were read out at both ends, and the division of the charge seen at each end gave a measurement of the z position with a resolution of about 1.7 cm. Further z position information was obtained from segmented cathodes on the inner and outer walls of the VD, which provided a z resolution of about 750 μm. The average r-ϕ resolution of the VD was about 150 μm.

The PT was removed in 1995 and replaced by a silicon vertex detector (SVX), pictured in Fig. 3.6. It was made of three concentric layers of 300-μm-thick double-

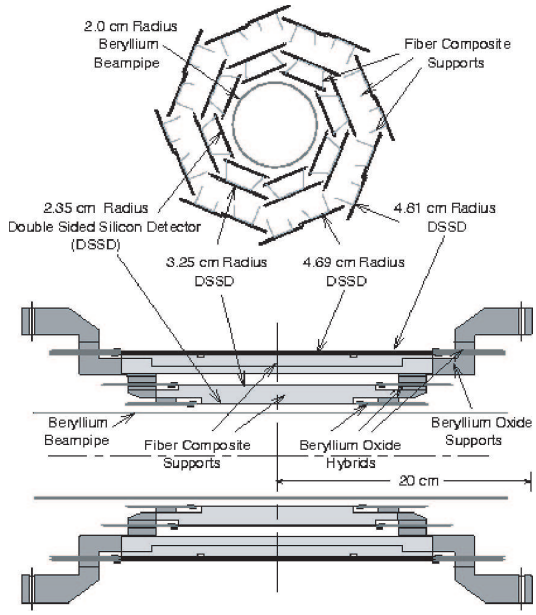

Figure 3.6: End-on (top) and side (bottom) cross-sectional views of the SVX detector in CLEO II.V

sided Si wafers mounted directly to the beam pipe. A charged particle traversing the active detector creates electron-hole pairs along its path, which are then collected on fine conducting sense strips on both sides of the silicon. The position resolution achieved by this device was about 30 μm in r-ϕ and 60 μm in z, much better than the earlier drift-tube detector PT. Nevertheless, the precision space points measured with the inner tracker were important for ensuring excellent track fits and precise momentum measurement.

The inner tracking system was crucial for many measurements made by CLEO, especially measurements of charmed particle decay. However, this analysis does not need precision vertex finding, as B mesons typically decay within $\sim 20\mu$m of the IP.

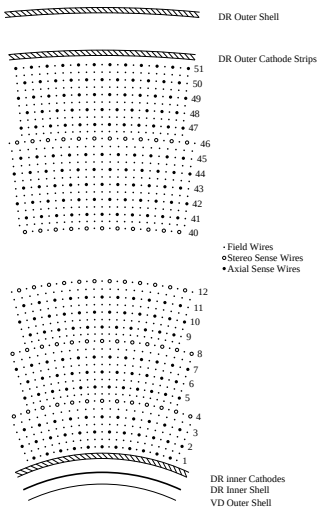

Figure 3.7: A cross-sectional view of the CLEO II main drift chamber.

3.2.3 The Central Drift Chamber

The largest and most important tracking device in CLEO II was known as the central drift chamber, or DR. Situated around the inner tracking layers, it consisted of 12,240 sense wires and 36,240 field wires arranged in 51 staggered layers of nearly square cells with dimensions 14 mm $\times$ 14 mm. The drift chamber itself had an inner radius of 17.5 cm, an outer radius of 95 cm, and was 2.15 m in length. Forty of the 51 layers were *axial*, having sense wires that ran parallel to the z-axis, while the sense wires in the other 11 *stereo* layers were skewed from the z-axis by 3°-7° to provide z information throughout the volume of the detector. The axial layer are staggered to help resolve the ambiguity of whether the particle passed through the cell to the left or the right of the sense wire. The layout of the cells is shown in Fig. 3.7.

The inner and outer radii were covered with longitudinally-segmented cathodes to

provide precision measurements of the z position at the beginning and end of most tracks. In the good barrel region, the momentum of a 2 GeV/c track was measured with a precision of about 0.6%.

Track Reconstruction

Track reconstruction is the process of turning the hits in the DR into more directly interesting physics quantities like momentum and position measurements. This process is described below.

Reconstruction begins by converting the raw hit times into drift distances using tracking-detector calibrations that were precisely determined and closely monitored as data was collected. Hits are then grouped into track candidates by pattern-recognition software. The track candidates are then fit with helical trajectories, corrected for energy loss in material. Several passes through an event's hits are necessary to assure the quality of the fits. Fit results that were stored included the helical trajectory parameters, their errors with correlations, and the residual of the fit, defined as

$$\texttt{RESICD} = \left[\sum_i (d_i^{obs} - d_i^{fit})^2 / N \right]^{1/2} \tag{3.4}$$

The sum is over all non-stereo layers i in the DR, d_i^{obs} is the measured drift distance for the hit in layer i, d_i^{fit} is the drift distance predicted by the track's helix, and N is the total number of degrees of freedom in the fit, a function of the number of DR hits included in the fit.

The track fitter was designed with a big-tent mentality; it formed and included track candidates that were reconstructed with incomplete information. One type

of these tracks are called *z-escapes*, arising when a particle's trajectory was nearly parallel to the beam axis, therefore not crossing most of the stereo layers or the cathodes. Another type of fit made with poor information is known as a *dredge seed*. Dredge tracks were formed near the end of track reconstruction, and are the fitter's attempt to cobble together additional tracks from hits not included in other tracks.

Confusing arrangements of hits can also lead to problematic tracking. A charged particle with a sufficiently low momentum will curve enough in the magnetic field so that it never reaches the DR's outer diameter and travels back toward the IP; such particles are known as *curlers*. Curlers can result in two or more separate track fits, one each for the outgoing and incoming parts of the particle's trajectory. Another common problem arises when hits from a single particle traveling away from the IP are split into multiple tracks. Extra tracks generated this way are known as *ghosts*. An event with examples of both ghosts and curlers is shown in Fig. 3.8. A separate processor, called `Trackman`, was run after track fitting to identify these and other spurious tracks.

Measurement of dE/dx

The amount of ionization that a charged particle produces in a material depends on its velocity. The linear density of energy deposited in the gas by the passage of a charged particle, dE/dx, is estimated from the integrated charge of the hits it caused in the DR. This quantity, when combined with the track's measured momentum, gives the DR some power to discriminate between particles of different mass, and thus some particle identification abilities.

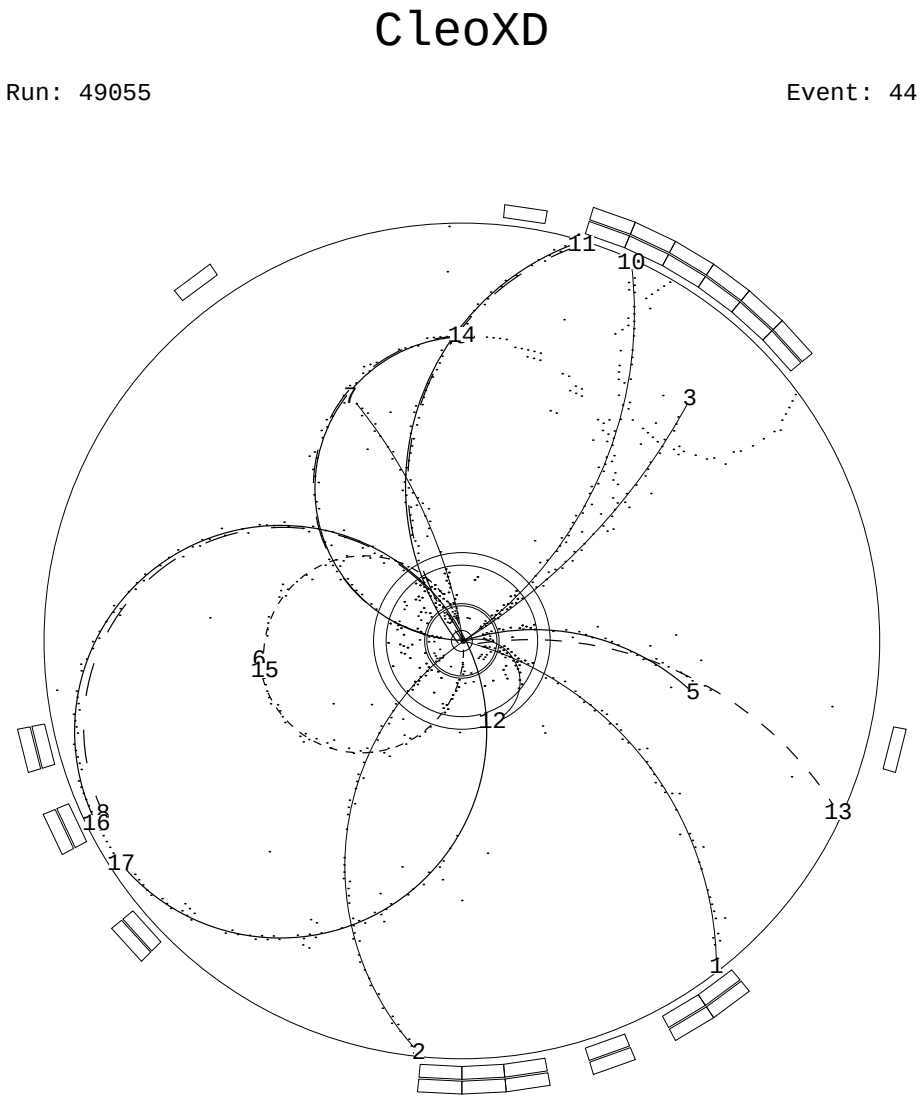

Figure 3.8: A CLEO event display containing examples of both ghost and curler tracks, viewed in the r-ϕ plane. DR hits are represented by dots and reconstructed tracks are shown as solid and dashed lines. Tracks 16 and 17 are two halves of a curler. Tracks 5 and 13 are a "ghost pair".

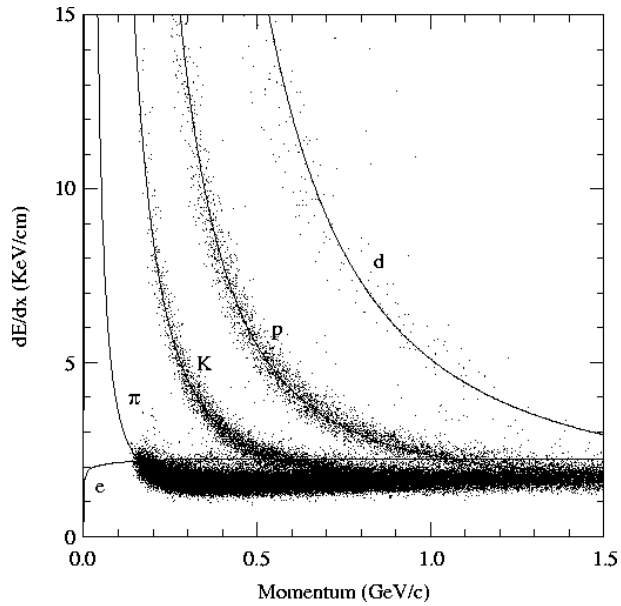

Figure 3.9: Measured dE/dx as a function of momentum. The solid lines represent theoretical curves for various particle types.

To perform particle identfication using dE/dx, we cut on the difference between the mean of the lowest half of the pulse heights (thus truncating the Landau-like high-side tail of the distribution) and the expected pulse heights for a given particle type divided by the expected resolution for that pulse height and number of hits. Fig. 3.9 shows the expected curves for various particle types versus measured dE/dx as a function of momentum. For electron identification in this analysis, we use the CLEO quantity `SGELDI`, the number of σ away the dE/dx measurement for a track is from the expected value for an electron.

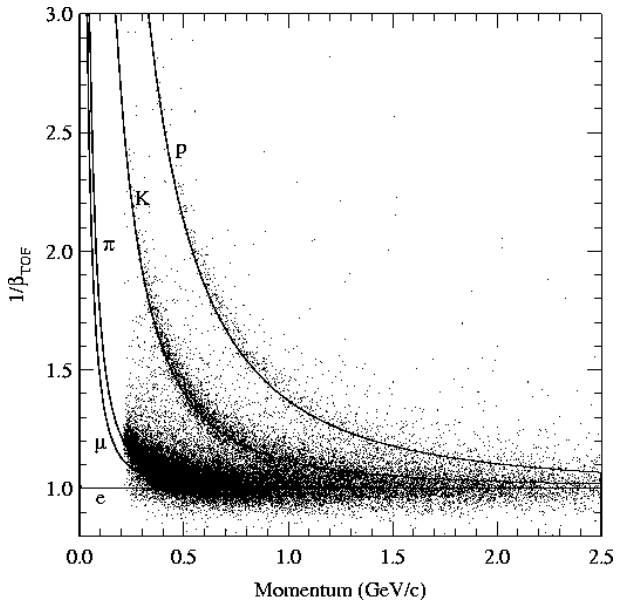

Figure 3.10: Measured times of flight as a function of momentum. The solid lines represent theoretical curves for various particle types.

3.2.4 The Time-of-Flight Counters

The Time-of-Flight (TF) system provided another source of information about a charged particle's velocity. It did this by measuring the amount of time between the crossing of an electron bunch and a positron bunch at the IP and the passage of a charged particle through strips of doped plastic sciltillator arranged outside the DR, approximately one meter away from the IP. Again, the velocity measurement combined with the momentum measurement provides a constraint on a particle's mass. Fig. 3.10 shows the expected curves for various particle types versus measured times of flight as a function of momentum.

The TF consisted of three sections arranged around the IP to provide good solid

angle coverage. The barrel section consisted of 64 rectangular blocks, each 2.8 m $\times$ 10 cm $\times$ 5 cm, arranged to form a cylindrical shell around the z-axis. A charged particle entering the sciltillator interacted with the heavy organic molecules embedded in it, causing the emission of a flash of light. This light was then fed through lucite light guides to a pair of photomultiplier tubes, one on each side. In each of the endcap regions were 28 wedge-shaped sections about 58 cm long and 5 cm thick. A single photomultiplier tube collected light on the narrow end of each section. Together, the barrel and the endcap sections covered about 97% of the solid angle. The time resolution of this system was about 150 ps.

Like in the case of dE/dx, we cut on the number of standard deviations between the measured arrival time of a charged particle and the expected time of a postulated particle type. In our electron identification package, we cut on a quantity called `SGELTF`, the number of σ between the measured time and the expected time for an electron.

3.2.5 The Electromagnetic Calorimeter

Along with the DR, the Electromagnetic Crystal Calorimeter (CC) are the subdetectors of CLEO most important to this measurement. As the name "calorimeter" suggests, the CC was designed to measure the energy of particles, both charged and neutral, entering it.

A particle entering one end of a cesium iodide (CsI) crystal will deposit a portion of its energy in the bulk of the crystal through various interactions, producing light that is read out by photo-diodes at the other end of the crystal. Particles such as

electrons and photons interact electromagnetically in the crystal, depositing almost all their energy through a cascading process of bremsstrahulung and pair production. Muons, being much heavier than electrons, will not be stopped by bremsstrahulung processes as easily, and will not deposit much of their energy in the CC. Hadrons, in addition to electromagnetic processes, can also interact via the strong force with the nuclei of the thallium-doped CsI crystals, producing secondary hadrons and causing non-localized showers. As we will see, different particles interact differently in the CC, so the characteristics of the resulting shower depend on the incident particle.

The CC itself is made up of about 7800 thallium-doped CsI crystals, each about 30 cm long and 5 cm square in cross section, distributed over the barrel and endcaps as shown in Fig. 3.4, covering 95% of the solid angle. The crystals are arranged to point nearly directly toward the IP; they are aimed slightly away from the IP to minimize gaps through which particles can pass undetected. Material between the IP and the CC will degrade a particle's energy before reaching the crystals, motivating the placement of the CC inside the solenoid.

Showers are reconstructed by first turning the amount of light detected in each crystal into an estimate of the energy deposited in that crystal. Since showers often span multiple crystals, neighboring crystals having deposited energies above threshold are grouped into clusters, with the requirement that the highest-energy crystal be at least 10 MeV. The position of the shower's center is then calculated as the energy-weighted mean of all the member-crystal positions. Showers are associated with DR tracks by loose track-shower matching criteria.

The energy and angular resolutions for barrel showers are 3.8% and 11 mrad for

100 MeV showers and 1.5% and 3 mrad at 5 GeV. The energy resolution of the barrel calorimeter is about 2% for 2.0 GeV electrons and photons. Endcap performance is degraded somewhat by the presence of the DR endplates and electronics in front of the crystals.

Measurement of E/p

The calorimeter is a critical component of electron identification. Electrons deposit almost all their energy in the CC, so if we neglect the electron's small mass, the ratio of the energy measured in the CC to the momentum measured in the DR should be near 1. Heavier particles do not efficiently dump their energy into the CC, and should have an E/p value significantly less than 1. One exception is antiprotons, which can annihilate with protons in the crystals. However, these interactions will produce a value of E/p significantly greater than 1, as the mass of both the proton and antiproton are converted into energy in addition to the initial kinetic energy of the antiproton.

Shower Shape

Showers from different particles have different shapes in the calorimeter. Electrons and photons leave relatively localized showers, while showers from hadrons tend to be broader. The quantity $E9/E25$, the sum of the energies in the 3x3 square of crystals around the center of the shower divided by the sum of energies in the 5x5 square, is used to give a measurement of the shape of a shower. Showers from electrons and photons will tend to have a $E9/E25$ value closer to 1 than hadrons. Overlapping

showers can pose a problem for the determination of $E9/E25$, as the shower recognition algorithms often do not correctly allocate the energy seen in crystals to the proper shower, or indeed even recognize that two showers are present. We will see the impact of this effect in our electron identification studies, detailed in Sect. 4.3.3.

3.2.6 The Magnetic Field

A large superconducting solenoid of diameter 3 m and length 3.5 m provided CLEO's 1.5-Tesla axial magnetic field. Cooled by liquid helium, the coil carries a current of 3500 A and stores 25 MJ of energy, and delivers a field that is uniform to $\pm 0.2\%$ over 95% of the tracking volume. The iron flux return for the magnet also serves as part of the absorber for the muon identification system.

3.2.7 The Muon Chambers

Since muons are leptons, they do not interact via the strong force. Therefore, they lose only a moderate amount of energy as they pass through the material of the detector. Due to their higher mass, they do not lose as much energy to bremsstrahulung processes as electrons. These qualities make them the only charged particles capable of penetrating the iron flux return yoke of CLEO's magnetic field, and relatively easy to identify. The muon detector (MU) exploits these qualities using gas-filled tracking chambers sandwiched between the 36-cm-thick layers of iron in the flux return yoke.

A MU tracking super-layer is shown in Fig. 3.11. Each super-layer consists of three layers of staggered proportional wire chambers 8.3 cm wide, 1 cm thick, and about

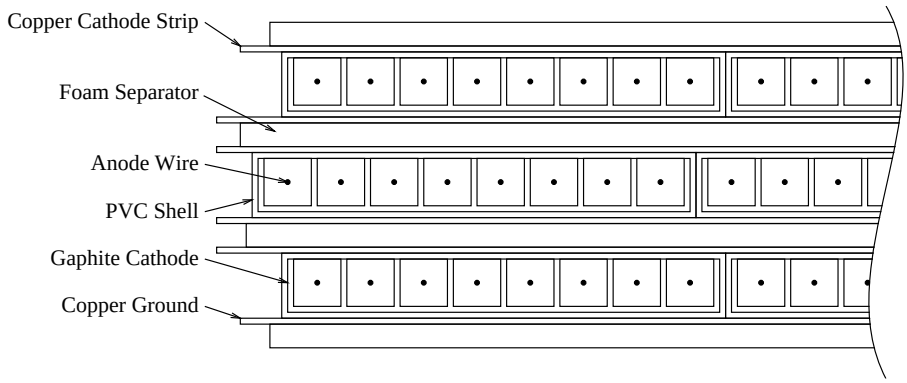

Figure 3.11: A cross-section of a muon chamber super-layer.

5 m long. Each chamber has eight rectangular cells with a sense wire strung along its center. Three of the cell's walls are coated with graphite and used as cathodes. The fourth wall is made of copper strips oriented perpendicular to the sense wire to provide z information. The eight sense wires in a counter are ganged together when read out, and adjacent counters' sense wire sets are connected together with a series of resistors. Muon hits are located using charge division from pulse height measurements made at each end of a read-out chain. Averaged over its volume, the muon detector's spatial resolution is about 5 cm. The three barrel super-layers are embedded in the iron at depths of 36, 72, and 108 cm, corresponding to 3, 5, and 7 *absorption lengths* (an absorption length is the average distance a particle travels in a material before scattering off a nucleus). There is one super-layer in the endcaps at a depth of about 7 absorption lengths.

Tracks are identified as muons by matching hits in the MU chambers to the extrapolated trajectory of a DR track. For a track to be identified as a muon in this analysis, we require that the deepest muon chamber to match a hit be at least 5 absorption lengths deep, and all the shallower chambers also have matched hits. For example, a track with hits matching in the muon chamber at depths of 3 and 5 absorption lengths is labelled a muon, while a track with hits matching at depths 3 and 7 (while missing hits in the depth 5 chamber) would not be identified as a muon.

3.2.8 The Trigger and Data Acquisition System

Bunch trains in CESR's electron and positron beams cross at the IP at a rate of about 3 MHz. The rate of interesting physics processes, however, is much smaller: production of $\Upsilon(4S)$ occurred at a rate of about 1-3 Hz. Including other processes such as tau, charm, 2-photon, and QED events, the total rate of interesting physics is about 10 Hz. It is impossible to read out and record the information from CLEO anywhere near the bunch-crossing rate, so we employ a sophisticated system of electronics and software filters, called *triggers*, to reduce the data flow to a more manageable rate.

There are tens of thousands of sensitive elements and corresponding electronic channels in CLEO, each of which could hold pertinent data in any given event. Readout of CLEO takes several milliseconds, and during this time the detector is insensitive to new physics events. This makes it crucial to read out the detector only during interesting physics events. To this end, a multi-level trigger and data acquisition system was developed [23, 24]. As data flows from the lowest level trigger to the highest, the decision process becomes increasingly refined and time-consuming; each level re-

ceives only the events that have passed the previous level, and uses increasingly more detailed information to make its decision.

The level-zero trigger (L0) is a hardware triger, the first and the fastest trigger in the system. Individual detector elements of the TF, CC, and VD were combined into groups for use in L0, and patterns of hits found in those groups were used to select interesting events. If an interesting event is found, sample-and-hold circuits on the individual data channels stored their current values until an event was either read out or failed some other trigger level. L0 reduced the event rate from the 3 MHz bunch-crossing frequency to a rate on the order of 20 kHz.

The level-one trigger (L1) is a hardware trigger that accepts all the events from the L0 trigger. Using information from TF, VD, CC, and DR detectors, L1's goal is to further reduce the event rate to about 100 Hz. If an event fails any of the L1 criteria, the trigger is reset and CLEO is ready to be read out again.

The level-two trigger (L2) accepts events passing L1, and using additional information from the VD and DR decides if an event should or should not be read out. Since only a fraction of the tens of thousands of channels in CLEO contain information during any particular event, only channels with values above a certain threshold were recorded. Events were accepted by L2 at a rate of about 25 Hz. After L2, the hardware trigger is reset, and CLEO is readied for data-taking again.

A software trigger logically called L3 takes the events passed by L2. At this stage, detector deadtime is no longer a concern, so rather sophisticated reconstruction algorithms can be run on the event. These algorithms were designed to reject other types of uninteresting events, such as cosmic rays or interactions of the beam with

residual gas molecules in the beampipe. `L3` rejects approximately half of the events passed to it by `L2`. Those that pass are written to tape for later analysis. Overall trigger efficiency for accepting $e^+e^- \to B\bar{B}$ events was over 99%.

3.2.9 Event Reconstruction

The various tasks of reconstructing the various signals in CLEO into interesting physics quantities, as well as the calculation of event-wide quantities (total energy of the event, thrust axis of the event, etc.) are accomplished by a two software packages, called `PASS1` and `PASS2`. `PASS1` is a collection of routines that specialize in fast track and event reconstruction, and is used to perform fast classification of the raw data events as well as running online to provide real-time feedback about the performance of the detector during data collection. `PASS2` is the main reconstruction software, specializing in accuracy at the cost of running much more slowly than `PASS1`. All data that is used for physics analysis by CLEO has been processed by `PASS2`.

3.3 Physics Simulation

We make heavy use of simulated data for various aspects of this analysis, as will be described in subsequent chapters. This section will explain the techniques used to generate this simulated data at CLEO. Simulated data at CLEO (called *Monte Carlo* data because of the use of a random number generator to determine outcomes) is generated in two steps.

The first step is a physics simulation. A program called `QQ` produces a list of

particles (and their respective 4-momenta) that are created in an e^+e^- interaction using a list of parameters for known particles and physics processes, including mass, spin, lifetime, and partial branching ratios. Whenever possible, these models and parameters are constrained by measurements. All of the Monte Carlo used in this analysis is $B\bar{B}$ Monte Carlo, where every e^+e^- interaction yields a pair of B mesons.

The list of particles produced by `QQ` is then passed to a program (based on CERN's `GEANT`) called `CLEOG`, which takes the stable particles in the QQ list and simulates the response of CLEO as the particle traverses it. To this end, `CLEOG` contains a full description of the CLEO detector, including the position, size, and type of materials a particle could encounter. As a particle is propagated through the detector and encounters material, a random number is thrown to determine if the particle interacts with the material. If it does, another random number is thrown to determine the effect of the interaction. If the material is instrumented, the detector's response is simulated. Hits from random trigger events (where CLEO was read out even though no physics event was seen) are inserted into Monte Carlo events to simulate detector noise. In the end, `CLEOG` produces an event in the same format as the real data from the CLEO detector is collected, so they can both be processed by `PASS2`.

A detailed description of the Monte Carlo samples produced for this analysis is given in Sect. 4.2.1.

CHAPTER 4

Measuring The Lepton Energy Spectrum

This chapter explains the method we used for extracting the electron-energy spectrum from $B \to Xe\nu$ decays. From this spectrum, we extract its moments (after a small correction for $B \to X_u e\nu$ decays), and with the number of tags we calculate the semileptonic branching ratio.

4.1 Strategy For Extracting the $B \to X_c e\nu$ Spectrum

We first select Υ(4S) events with a "tag," a lepton with momentum $p_t \geq 1.4$ GeV/c; more than 97% of the leptons in $B\bar{B}$ events satisfying this requirement are from semileptonic B decays. Within events with a tag lepton, we look for an additional "signal" electron with momentum $p_e \geq 600$ MeV/c.

The whole reason for "tagging" one of the B mesons with a lepton tag is to determine its flavor, and from that infer the flavor of the other B. This information gives us insight into the source of our signal electron. Table 4.1[1] summarizes the main sources of our signal electrons and their resulting charges, given a positively-charged

[1] $B^0\bar{B}^0$ mixing is a second-order weak process where a neutral B changes, or "mixes" into its antiparticle. So when mixing occurs, a $B^0\bar{B}^0$ becomes either a B^0B^0 or a $\bar{B}^0\bar{B}^0$ event.

	No B^0 Mixing	**B^0 Mixing**
Primary Events	$\ell^+ \leftarrow \bar{b} \quad b \longrightarrow e^-$	$\ell^+ \leftarrow \bar{b} \quad \bar{b} \longrightarrow e^+$
Opposite B Secondary Events	$\ell^+ \leftarrow \bar{b} \quad b \rightarrow c \rightarrow e^+$	$\ell^+ \leftarrow \bar{b} \quad \bar{b} \rightarrow \bar{c} \rightarrow e^-$
Same B Secondary Events	$\ell^+ \leftarrow \bar{b} \longrightarrow \bar{c} \rightarrow e^-$	

Table 4.1: Charge correlations for dilepton $B\bar{B}$ events.

tag. Assuming the tag lepton came from a semileptonic B decay, the signal electron comes mainly from three sources:

1. The semileptonic decay of the B meson that did not produce the tag lepton (hereafter referred to as "primary electrons," or $\frac{d\mathcal{B}(b)}{dp}$);

2. The semileptonic decay of a charmed meson produced in the decay of the B meson that was not the parent of the tag ("opposite-B secondary electrons," or $\frac{d\mathcal{B}(c)^{oppB}}{dp}$);

3. The semileptonic decay of the charmed meson that was produced in the semileptonic decay that produced the tag lepton ("same-B secondary electrons," or $\frac{d\mathcal{B}(c)^{sameB}}{dp}$).

To separate the primary electrons from the other two possibilities, we exploit charge and kinematic correlations between the electron and its tag. Requiring the tag and the signal electron to have unlike charges eliminates the opposite-B secondary electron background in events where $B^0\bar{B}^0$ mixing has not occurred. Of course, if one of the neutral B's mixes, this charge correlation is reversed.

Therefore, we separate our sample into two types of events: "unlike-sign" events, where the tag lepton and signal electron have opposite charge, and "like-sign" events, where they have the same charge. The contributions of these sources to the measured electron spectrum, including the effect of mixing, can then be described by the following equations:

$$\frac{dN(\ell^{\pm}e^{\mp})}{dp} = N_{\ell}\,\eta(p)\,\epsilon(p)\left[\frac{d\mathcal{B}(b)}{dp}(1-\chi) + \frac{d\mathcal{B}(c)^{oppB}}{dp}\chi + \frac{d\mathcal{B}(c)^{sameB}}{dp}\right] \tag{4.1}$$

$$\frac{dN(\ell^{\pm}e^{\pm})}{dp} = N_{\ell}\,\eta(p)\left[\frac{d\mathcal{B}(b)}{dp}\chi + \frac{d\mathcal{B}(c)^{oppB}}{dp}(1-\chi)\right], \tag{4.2}$$

where N_ℓ is the number of tag leptons in the sample, $\eta(p)$ is the efficiency of electron identification, $\epsilon(p)$ is the efficiency of the "diagonal cut" (described in Sec. 4.1.1), and χ is the fraction of our total events that $B^0\bar{B}^0$ mixing occurred, determined as described in Sec. 4.1.2.

4.1.1 Diagonal Cut

To get a soluble set of equations from Eqs. 4.1 and 4.2, we need to remove the same-B secondary electron term from Eq. 4.1. To do this, we exploit the kinematic correlation between tags and signals coming from the same B. When it is produced, the tag lepton recoils against the daughter hadron, so on average the hadron is boosted in a direction opposite to the tag lepton. If this hadron then decays semileptonically to a signal electron, that electron will tend to have momentum in the same direction that the hadron was boosted, i.e. the direction opposite to the tag. Therefore, the tag and signal will tend to be back-to-back. Since the B's are essentially at rest, dilepton

pairs coming from opposite B's have momenta that are to a good approximation uncorrelated. One can see the strong correlation of these same-B secondary events in the plot on the right in Fig. 4.1, which shows the cosine of the angle between the tag and signal momentum vectors (the "opening angle" $\theta_{\ell e}$) versus the signal's momentum. The preponderance of events at $\cos\theta_{\ell e} \approx -1$ shows the back-to-back tendency of same-B secondary events.

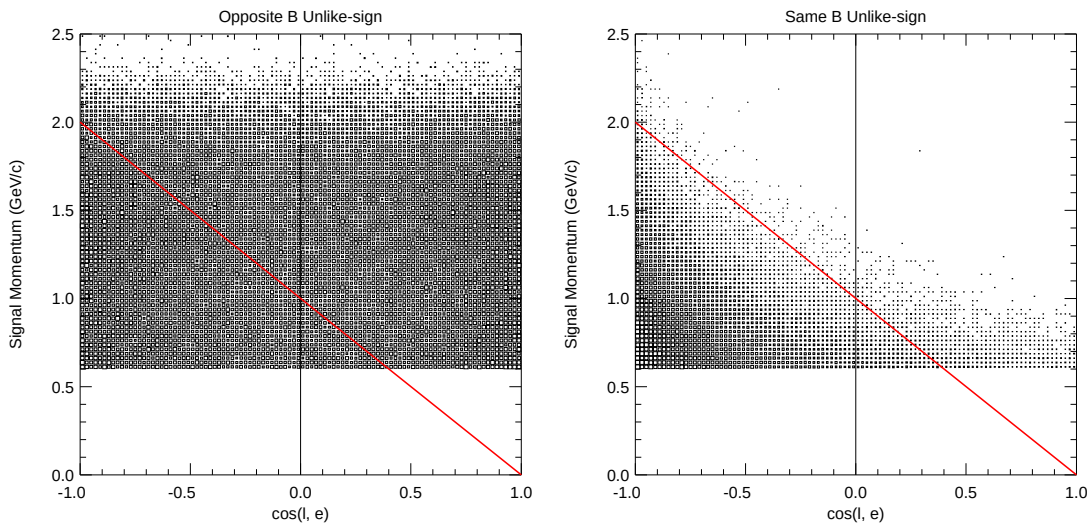

Figure 4.1: Monte Carlo simulation of electron momentum versus the cosine of the opening angle between the tag lepton and the signal electron (cos $\theta_{\ell e}$) for dilepton pairs from opposite B's (top) and from the same B (right). The line indicates $p + cos\theta_{\ell e} = 1$.

Inspection of the plots in Fig. 4.1 suggest that a cut in the 2-D plane of signal-electron momentum p and the opening angle between the tag lepton and the signal electron cos $\theta_{\ell e}$ will greatly suppress the same-B secondaries while accepting a majority of the primaries. We therefore use a "diagonal cut", $p + cos\ \theta_{\ell e} \geq 1$. This cut is

identical to that used in the previous CLEO II analysis [25, 26], and is applied only to unlike-sign events.

We have checked that this cut does not bias our measurement by affecting different $B \to X_c \ell\nu$ decay modes differently. Fig. 4.2 shows that the efficiency of the diagonal cut for $B \to D\ell\nu$, $B \to D^*\ell\nu$, $B \to D^{**}\ell\nu$, and $B \to DX\ell\nu$ is essentially independent of decay mode.

4.1.2 $B^0\bar{B}^0$ Mixing

We determine the mixing parameter χ by combining several pieces of experimental information. The value in PDG2002 for the $B_d^0\bar{B}_d^0$ mixing parameter is $\chi_d = 0.181 \pm 0.004$ [10]. The charged/neutral B lifetime ratio from the same source is $\tau_\pm/\tau^0 = 1.083 \pm 0.017$. CLEO has measured the ratio of charged to neutral B production at the $\Upsilon(4S)$, $\frac{f_{+-}\tau_\pm}{f_{00}\tau_0} = 1.11 \pm 0.08$ [27]. Combining these inputs, we find $\chi = f_{00}\chi_d = 0.089 \pm 0.004$. This is the value for χ and the error that we use in extracting the primary and secondary spectra from the measured like- and unlike-sign spectra.

A semi-independent confirmation of this that uses semileptonic B-decay information in a very direct way follows from the most recent CLEO measurement of the rate of same-sign to unlike-sign dilepton production in $B\bar{B}$ events: $r = \frac{\ell^+\ell^+ + \ell^-\ell^-}{\ell^+\ell^-} = 0.081 \pm 0.002$ [28]. When combined with the lifetime data and the production ratio, this gives $\chi = 0.088 \pm 0.003$, in excellent agreement with the first value.

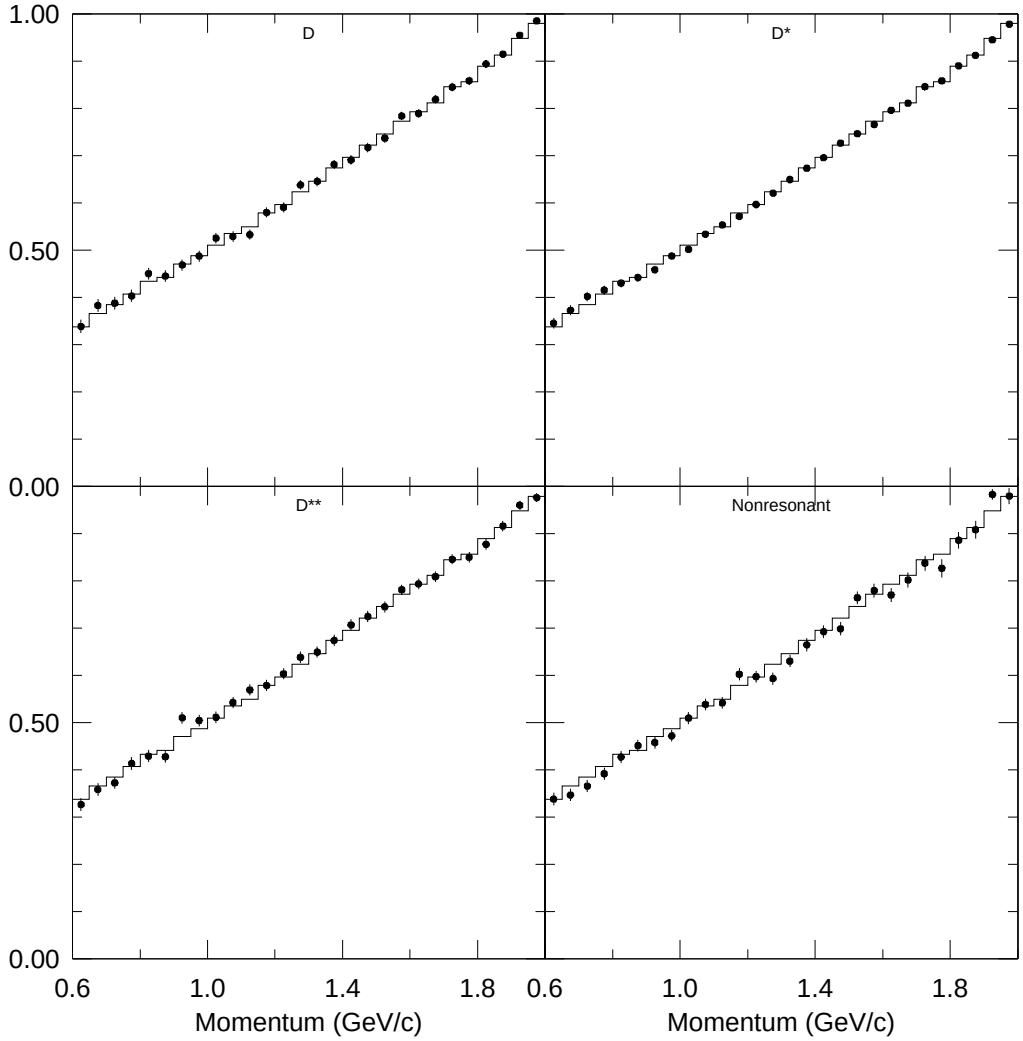

Figure 4.2: The efficiency of the diagonal cut determined with Monte Carlo simulations of lepton-tagged $B\bar{B}$ events with four different semileptonic decay modes. Clockwise from the top left, the points represent $B \to De\nu$, $B \to D^* e\nu$, $B \to DXe\nu$ and $B \to D^{**}e\nu$. The histograms are the same in all four plots, and give the overall efficiency for the complete mixture of semileptonic B decays. There is no discernible mode-to-mode variation.

4.2 Data Samples and Event Selection

We have analyzed the entire CLEO II and CLEO II.V dataset, giving us a total integrated luminosity of 9.4 fb^{-1} ON the $\Upsilon(4S)$ and 4.5 fb^{-1} OFF, which is taken at center-of-mass energies about 60 MeV below the nominal $\Upsilon(4S)$ mass and below the $B\bar{B}$ production threshold.

We start by selecting hadronic events with a standard CLEO event classification cut. For this analysis, we augment it with a tighter charged multiplicity requirement. Since $B\bar{B}$ events have higher average multiplicity than background processes like τ-pairs, radiative Bhabhas and μ-pairs, and two-photon events, we require an event to have at least five charged tracks that pass our track-quality criteria (Sec. 4.3.1).

Lepton production at the $\Upsilon(4S)$ includes a sizable continuum (non-$B\bar{B}$ hadronic events) component which is subtracted using the OFF data sample. Before subtraction, OFF distributions must be scaled to correct for differences in the integrated luminosities and for the energy dependence of the continuum production cross section. The ON/OFF scale factor is defined as

$$\alpha_{\mathcal{L}} = \frac{\mathcal{L}_{ON}}{\mathcal{L}_{OFF}} \times \left(\frac{E^2_{OFF}}{E^2_{ON}} \right),$$

where $\mathcal{L}_{ON}$ and $\mathcal{L}_{OFF}$ are the ON and OFF integrated luminosities, and E^2_{ON} and E^2_{OFF} are the luminosity-weighted average beam energies. Using this formula, we find scale factors of $\alpha_{\mathcal{L}}(\mathrm{II}) = 1.931$ and $\alpha_{\mathcal{L}}(\mathrm{II.V}) = 2.170$ for the CLEO II and CLEO II.V samples, respectively.

Independent determinations of these scale factors have been made by computing

the ratio of ON and OFF yields of charged tracks between 3.0 and 3.5 GeV/c, well above the B-decay kinematic limit. For CLEO II the ratio is 1.931 ± 0.007, in excellent agreement with the above-computed ratio. For CLEO II.V the track ratio is 2.158 ± 0.006, smaller than the integrated-luminosity result by 0.6%. (A similar disagreement for CLEO II.V was observed in a previous analysis [29].) Since the track ratios provide a direct measurement of the ON/OFF normalization as it affects subtraction of spectra, we have opted to use it rather than the corrected luminosity ratio for CLEO II.V, and take 1% as the overall uncertainty on the luminosity scale factor.

4.2.1 Monte Carlo Samples

Monte Carlo samples are used in this analysis for the determination of some components of the event- and track-selection efficiencies, and to estimate several contributions to the background.

The most important sample was a full-`CLEOG` simulation of $B\bar{B}$ events with at least one decay to a high-momentum lepton. The statistics of this sample (like CLEO's generic $B\bar{B}$ Monte Carlo) amounted to approximately five times that of the combined CLEO II and II.V data set. Unlike the generic CLEO Monte Carlo, we enabled PHOTOS [30] to model electroweak radiative corrections. Preselection criteria were used within `QQ` to select for full simulation only events with at least one generated lepton of momentum greater than 1.35 GeV/c.

In measuring the momentum spectrum for $b \to c\ell\nu$ we must correct for the contribution of $b \to u\ell\nu$. For this we use a sample of Monte Carlo generated using the `INCLGEN` generator [31]. `INCLGEN`, developed for CLEO's most recent exclusive $|V_{ub}|$

measurement, is built on the inclusive description of $b \to u\ell\nu$ developed by DeFazio and Neubert [32], with shape-function parameters determined by fitting CLEO's inclusively measured $b \to s\gamma$ energy spectrum [17]. For all final states with hadronic masses up to that of the $\rho(1450)$, exclusive final states as described by ISGW2 [33] are substituted. The scale for the subtraction was set by normalizing the `INCLGEN` spectrum to CLEO's measured partial branching fraction [29, 34] in the best-measured region of 2.2-2.6 GeV/c. The resulting $b \to u\ell\nu$ spectrum (Fig. 7.1) is subtracted from the primary spectrum (Fig. 4.21) to produce the final $b \to c\ell\nu$ spectrum in Fig. 7.2, which is ready for the computation of the moments.

The `INCLGEN` sample has also been used to provide additional statistics for efficiency corrections in the momentum range near the $b \to c\ell\nu$ end point (see Sec. 4.5).

In addition, various `QQ`-only samples were generated to determine several corrections. We will describe their production when necessary throughout this chapter.

4.3 Lepton Identification

4.3.1 Track Quality

The first step in lepton identification is to require that a track be well measured before it is passed to the lepton identification packages. A well-measured track must pass a rather standard set of track quality cuts:

- `KINCD` ≥ 0 (Good track fit with vertex in interaction region)
- Pass `Trackman`

- Not a dredge or z-escape track
- Pass three of the following:
  - 0.02 mm $\leq$ `RESICD` $\leq$ 1.0 mm
  - the track's distance of closest approach to the beam spot is $\leq$ 5 mm
  - the z position of the track vertex is within 5 cm of the z position of the beam spot.
  - DR hit fraction $\geq$ 30%

The DR hit fraction is defined as the ratio of the number of DR hits found for a track to the number expected given its reconstructed trajectory.

Once a track passes these cuts, we subject it to a set of lepton identification requirements to reject hadron tracks.

4.3.2 Muon Identification

We identify muons with momenta of at least 1.4 GeV/c for use as tags by requiring that the outermost matched hits in the muon chambers be at least 5 absorption lengths deep in the iron (designated as `DPTHMU` $\geq$ 5), and that all the chambers at shallower depths also have hits matched to the track (denoted `MUQUAL = 0`).

Because muons are used only as tags in this analysis, we are insensitive to many of the details of muon identification. Specifically, we do not need to know the efficiency of muon identification, since we use the overall number of tags *detected* to normalize the spectrum and measure the branching ratio. However, a good understanding of

the contribution from "fake" muons (non-muon tracks passing our muon identification cuts) is essential, as they are a background that renders the charge correlations meaningless. The determination of fake rates is discussed in Sec. 4.4.1.

4.3.3 Electron Identification

Electron identification is extremely important to this measurement; the biggest systematic uncertainties in the last measurement of the tagged electron spectrum [26] were those arising from electron identification. Therefore, much work has gone into developing an electron identification package and understanding its efficiency and fake rates.

We had several choices for electron identification packages. Our goal was to develop an electron identification package that had a relatively momentum-independent and well-understood efficiency, while still having manageable fake rates.

*C*ornell *E*lectron *ID*entification (CEID) [35, 36] is CLEO's standard electron indentification package. It uses information from several sources and combines them into the log-likelihood `R2ELEC`. CEID is trained, and its efficiency and fake rates are measured with data. In particular, electrons from radiative Bhabha events embedded in hadronic events are a primary tool. Studies [37] have suggested that using radiative Bhabhas to measure the efficiency of the CEID package leads to a significant bias in the momentum region above 1.8 GeV/c, especially for CLEO II.V data. It has been suggested that the source of this bias is distortion of the electron's shower shape due to overlap of the electron and the radiated photon in the calorimeter. A technique was developed, the `PVRTX` cut [36], to select a radiative Bhabha sample where this

shower-overlap effect is minimized for use in determining the `CEID` efficiency. This cut requires that the sum of the energies of all showers in the calorimeter within 0.3 radians of the track be less than 3 GeV. There remained some trepidation, however, about whether the momentum dependence in the efficiency was purely a feature of the selection of radiative Bhabha electrons or a real effect that also applied to identifying electrons in hadronic events.

We decided that a more robust solution to this problem was to employ electron identification criteria that are not dependent on details of shower shape or other features that may not be the same in $B\bar{B}$ and radiative Bhabha events. The package *S*imple *E*lectron *ID*entification (SEID) was originally conceived [38] for use in tau physics, where well-understood electron identification efficiency is more important than low fake rates. Its simplicity, high efficiency, and independence of shower-shape information made it an attractive starting point for our analysis.

As designed, SEID consists of only two cuts: $E/p > 0.85$ and `SGELDI` > -2.0. In hadronic events, rejection of fake electrons from antiproton annihilation in the calorimeter can be enhanced, with little loss in efficiency, with a high-end E/p cut, $E/p < 1.1$. Time-of-flight cuts, applied only when good time-of-flight information is available, were similarly found to reduce antiproton and kaon fake rates with a small loss in efficiency.

This combination of cuts, "SEID+TF," proved to be very competitive with CEID at momenta above 1 GeV/c and while showing evidence of the "`PVRTX`" effect described above (due to the high-side E/p cut), the effect was much smaller than in CEID, and disappeared completely with the application of the `PVRTX` cut. The proce-

dure was still significantly less effective than CEID at eliminating fakes for momenta below 1 GeV/c, however, and concerns about the determination of (especially kaon) fake rates at low momentum seemed to introduce a significant additional systematic error.

Based on these considerations, we have adopted a set of electron identification cuts we dubbed TEID (*T*he *E*lectron *ID*entification). It exploits the strengths of each individual package: CEID gives high efficiency and small fake rates at low momentum, while the efficiency of SEID at high momentum is less momentum dependent and more reliably measured with embedded radiated Bhabhas. The TEID cuts are

1. **0.6 - 1.0 GeV/c**: CEID
    - `R2ELEC` ≥ 3
2. **1.0 - 1.6 GeV/c**: SEID+TF
    - $0.85 \leq E/p \leq 1.1$
    - `SGELDI` $\geq$ -2.0
    - `SGELTF` ≤ 3.0 if:
        - `TFSTAT` $= 2$ and `TFIDQL` $= 0$ (good TF information)
3. $\geq$ **1.6 GeV/c**: SEID
    - $0.85 \leq E/p \leq 1.1$
    - `SGELDI` $\geq$ -2.0

The determination of the efficiency of the electron identification package with radiative Bhabha events embedded in hadronic events is described in Sec. 4.5.2.

We handle the estimation of fake-lepton yields in the usual way for precision analyses: accumulating track spectra in data using all analysis cuts except for lepton identification and then combining with fake rates measured with tagged $\pi^{\pm}$, $K^{\pm}$ and $p/\bar{p}$. The determination of the fake rates is described in Sec. 4.4.1.

A significant advantage of this cut-based electron identification package is the ease with which specific components can be adjusted or eliminated to assess systematic uncertainties. A complete description of this determination is given in Sec. 5.5.

Monte Carlo plays no role in this procedure, except for small corrections and the determination of the relative particle abundances with generic $B\bar{B}$ events.

Electron Identification in Monte Carlo

Traditionally, electron identification in the `CLEOG` Monte Carlo is "kludged," i.e. the event-reconstruction software peeks at the generator information to get a track's identity, and assigns a value for the electron identification variable accordingly. The goal is to apply, on the user's behalf, distributions for fakes and efficiencies that are equivalent to those measured in the data. This procedure has drawbacks for precision measurement. The "training" information used by `CLEOG` may not have been completely up-to-date at the time of production; the events from which such information is derived may not be compatible with those for a specific analysis; and the training information may not represent the same distribution of luminosities as a specific measurement.

Because of these shortcomings, we chose not to develop this facility for our electron identification procedure, but adopted a simpler and more flexible procedure. In accumulating distributions from Monte Carlo we assume perfectly efficient electron identification. The most appropriate and up-to-date efficiency information can then be applied to the Monte Carlo events when specific distributions are produced from them. (This also facilitates the use of multiple electron identification packages, as well as adjustments to cuts in assessing systematic errors.) Our procedures for determining the electron identification efficiency and results for the TEID procedure are described in Sec. 4.5.2. We rely on `CLEOG` to simulate the efficiency of muon detection, for which it is quite reliable. This affects our analysis only through the selection and vetoing of muon tags.

4.3.4 Physics Vetoes

Many of the background leptons for this measurement are from semileptonic decays. These decays produce undetected neutrinos, making a reconstruction of the invariant mass quite hard. However, there are some leptons from decays in which all the final state particles are detectable. In these cases, we can employ mass-reconstruction cuts to suppress leptons from these sources.

J/ψ veto

Leptons from the decays of J/ψ's produced in B decays are potentially a significant background for this analysis. We apply a veto to our candidate tag leptons and signal electrons by calculating the invariant mass of the candidate and any oppositely-

charged track above 800 MeV that passes loose lepton identification cuts. For electrons, the second track must either pass `R2ELEC` $\geq$ 3 or $E/p \geq 0.85$. For muons, the second track must pass `MUQUAL` $= 0$ and `DPTHMU` ≥ 3. Monte Carlo was used to determine the mass windows for electron and muon candidates. In each case, the J/ψ mass peak was fitted with a bifurcated gaussian, and the asymmetric windows were chosen at $\pm 3\sigma$. The efficiency of this veto to reject a tag lepton from J/ψ is 65.4%. For unlike-sign signals electrons, the efficiency for rejection is 58.4%, and for like-sign signals it is 56.6%. Application of the veto introduces a very small inefficiency when signal electrons are erroneously flagged as daughters of J/ψ. This was determined with Monte Carlo to be 0.04% and 0.07% for the unlike-sign and like-sign signals, respectively.

$\pi^0 \to \gamma e^+ e^-$ veto

We reject both tag and signal candidates from π^0 Dalitz decays by requiring that the three-body invariant mass of the candidate, an oppositely-charged track above 500 MeV, and a photon be within 3σ of the π^0 mass. The second track has *no* electron identification requirements. The photon is determined to not be from a $\pi^0 \to \gamma\gamma$ decay by requiring that the reconstructed mass of it with any other photon in the event must be more than 3σ away from the π^0 mass. This veto has little effect on the tag sample, since Dalitz decays of π^0's from B's produce very few electrons above 1.4 GeV. The efficiencies for rejecting Dalitz electrons are 28.6% and 29.7% for unlike- and like-sign signals, respectively. The signal inefficiencies associated with this cut are 0.2% and 0.7%.

γ conversion veto

Photon conversions in material are rejected by the `GCFIND` routine. This routine combines a candidate with another track of opposite charge, forms a vertex, and flags the candidate as coming from a photon conversion based on the distance of closest approach, the vertex position in the detector, and other such quantities. It rejects about 40.7% of tags, 56.2% of unlike-sign signals, and 54.7% of like-sign signals from photon conversions, while introducing an inefficiency of about 2.0% for both cases.

4.3.5 Raw Spectra

For the measurement of the inclusive electron sample we first select the subset of events passing our event-selection criteria (Sec. 4.2) that have at least one tag. To be accepted as a tag, a track must

- be in the good barrel fiducial region, $|cos\theta| \leq 0.707$,
- have momentum between 1.4 GeV/c and 2.6 GeV/c,
- pass the track-quality and veto cuts described in Sects. 4.3.1 and 4.3.4, and
- be identified as either an electron or a muon, as defined in Sects. 4.3.2 and 4.3.3.

In events with tags, we look for a signal electron. To be accepted as a signal electron, a track must

- be in the good barrel fiducial region, $|cos\theta| \leq 0.707$,
- have momentum between 0.6 GeV/c and 3.0 GeV/c,

- pass the track-quality and veto cuts described in Sects. 4.3.1 and 4.3.4, and
- be identified as an electron, as defined in Sec. 4.3.3.

Fig. 4.3 gives the signal-electron momentum spectra separately for events with like-sign tags and for those with unlike-sign tags. The unlike-sign spectrum with the diagonal cut applied (Sec. 4.1.1) is shown in Fig. 4.4. Of course, the diagonal cut is not applied to like-sign events.

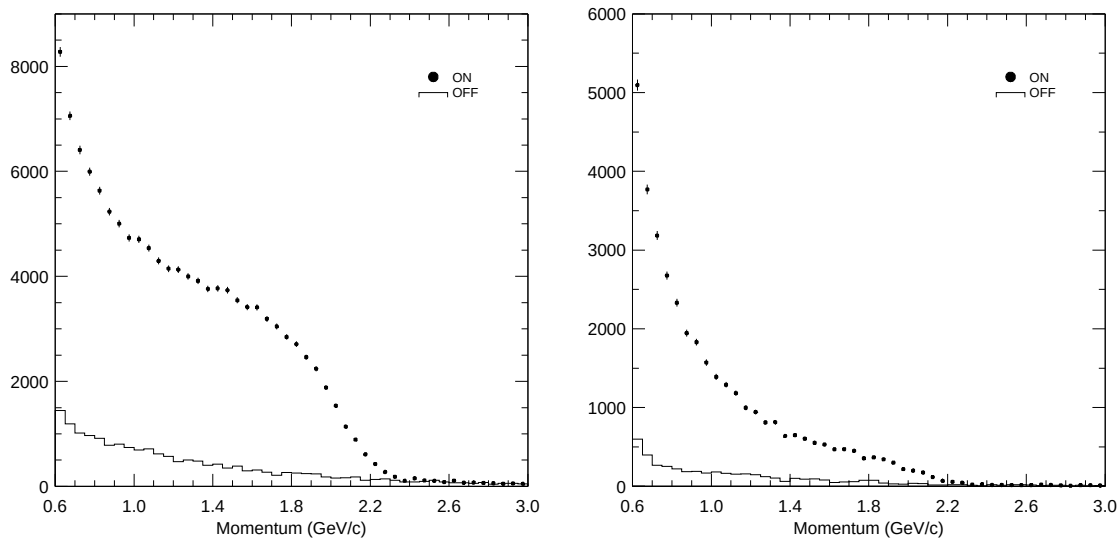

Figure 4.3: Electron spectra for ON and scaled-OFF samples of events with unlike- (top) and like-sign (bottom) tags.

4.4 Background Corrections to Raw Spectra

Not all the leptons in $B\bar{B}$ events come from primary B or secondary charm decays. Background contributions to the charge-separated spectra can occur when either the

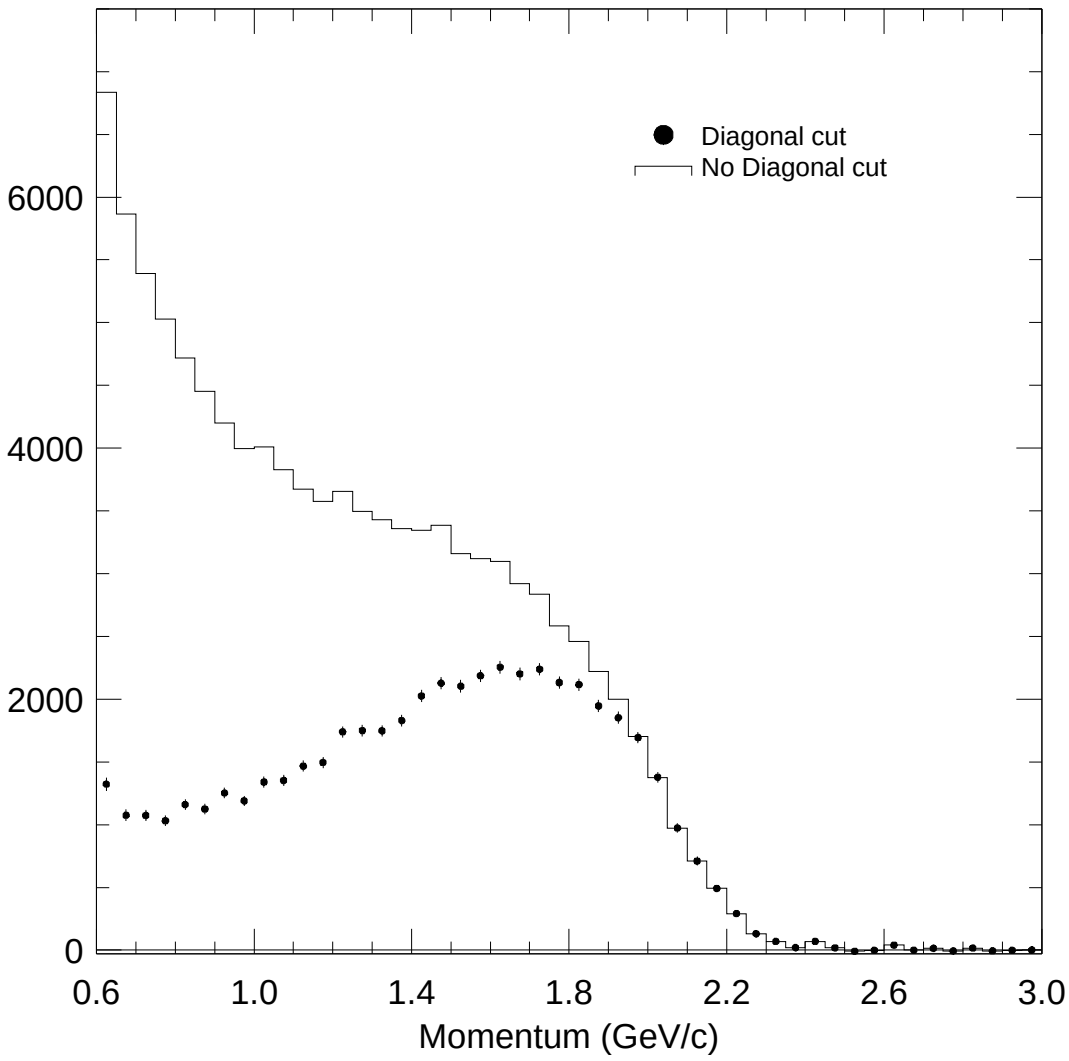

Figure 4.4: Continuum-subtracted electron spectra for all unlike-sign tagged events (histogram) and those passing the diagonal cut (points).

tag or the signal electron is not from semileptonic B decay. To correct for these backgrounds, we must first subtract candidate signal electrons whose *tags* come from

- fake leptons,
- semileptonic decays of D's or other charmed particles,
- J/ψ, π^0 Dalitz, or photon conversions that "leaked" through a veto, or
- leptons from several other sources in B decays, including leptonic decays of τ's, leptonic decays of ψ', and Dalitz decays of η (non-vetoed backgrounds).

Once these are removed, we subtract signal electrons from

- fake electrons,
- J/ψ, π^0 Dalitz, or photon conversions that "leaked" through a veto,
- τ, ψ', Λ_c, K_L^0, or η Dalitz (non-vetoed backgrounds),
- the same B as the tag (diagonal cut leakage, unlike-sign only), or
- upper-vertex charm.

Each of these background corrections is described in the following sections. All of corrections are shown in Fig. 4.11, and the charge-separated spectra after the backgrounds are subtracted are shown in Fig. 4.12.

4.4.1 Fake Leptons

Fake leptons are charged kaons, charged pions, and protons or antiprotons that are misidentified as electrons or muons. We have measured the species-by-species probabilities for misidentification with tagged samples of pions from K_S^0 decays, kaons from $D^* \to D \to K\pi$, and protons and antiprotons from $\Lambda/\bar{\Lambda}$ decays [39]. Fake-rate measurements with large momentum bins demonstrated that there were no measurable differences in fake rates between CLEO II and CLEO II.V or between ON and OFF data. The full data sample was therefore combined to maximize the statistical significance of our fake-rate measurements. Examples of the $\pi^\pm$ and $K^\pm$ fake rates for TEID and `DPTHMU` ≥ 5 muons are given in Fig. 4.5. Because our $B \to X\ell\nu$ measurements average positive and negative leptons, we used only charge-averaged fake rates and did not separate candidate-track spectra by charge.

The results of this final step for TEID and `DPTHMU` ≥ 5 are given in Fig. 4.7 in Sec. 4.4.1. Smoothing is an optional step to reduce the bin-to-bin scatter due to limited statistics.

Application of Fake Rates

The separate pion/kaon/proton fake probabilities were combined into overall fake probabilities per hadron track appropriate for B decays with abundances determined with CLEO standard generic $B\bar{B}$ Monte Carlo (see Fig. 4.6). The fake rates were measured in 50 MeV/c bins, and smoothed using a MN_FIT spline technique for muons, and by combining groups of bins for electrons. Even though the statistics of the electron-fake measurements were not large, as reflected by the need to combine

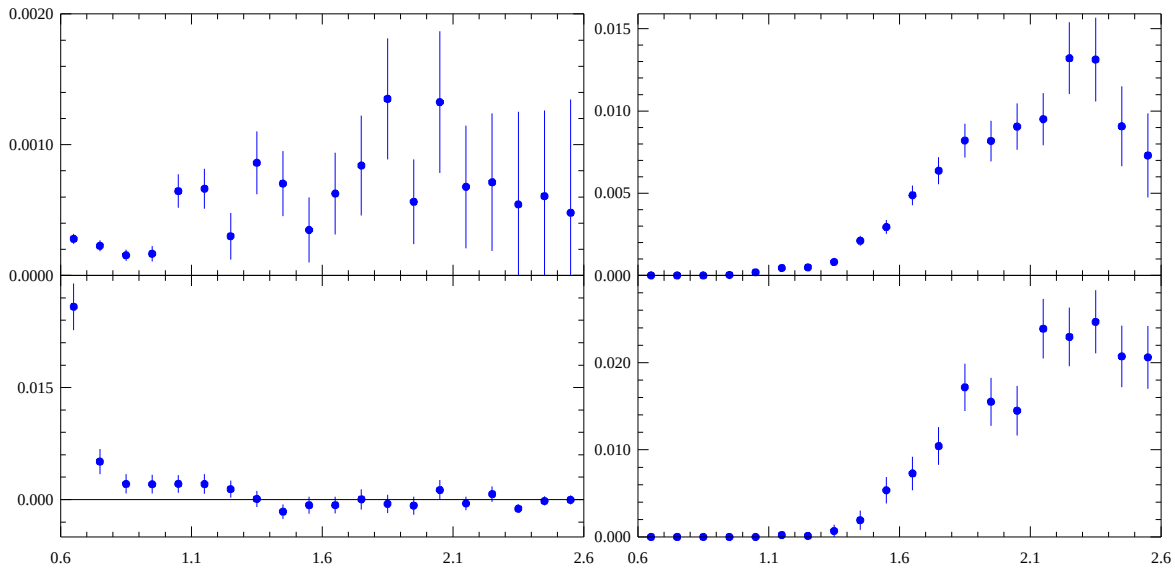

Figure 4.5: TEID (left) and DPTHMU ≥ 5 (right) fake rates for charged pions (top) and charged kaons (bottom). Note the different vertical scales.

bins, the contribution of these statistical errors to the measured spectra was negligible. We therefore treated the uncertainties in the fake rates as entirely systematic (Sec. 5.4). Our final abundance-weighted fake rates for TEID, both as measured and after smoothing, are shown in Fig. 4.7.

The contribution of fake leptons to any momentum spectrum is determined by combining the momentum-dependent fake probabilities with the continuum-subtracted spectrum of hadronic tracks that pass the same cuts, except for lepton identification, as the lepton sample in question. The number of hadronic tracks N_h that are candidates for misidentification as leptons is computed with the following formula [26]:

$$N_h = \frac{n_t - (1 + R_{\mu/e})(n_e/\epsilon_{eID})}{1 - (1 + R_{\mu/e})(f_e/\epsilon_{eID})}. \tag{4.3}$$

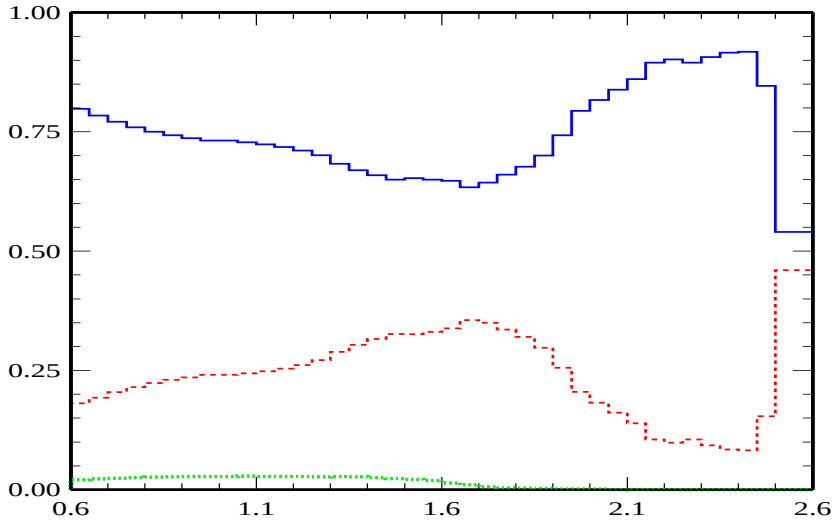

Figure 4.6: Relative abundances of $\pi^{\pm}$ (blue solid line), $K^{\pm}$ (red dashed line), and $p/\bar{p}$ (green dotted line) from generic CLEO $B\bar{B}$ Monte Carlo.

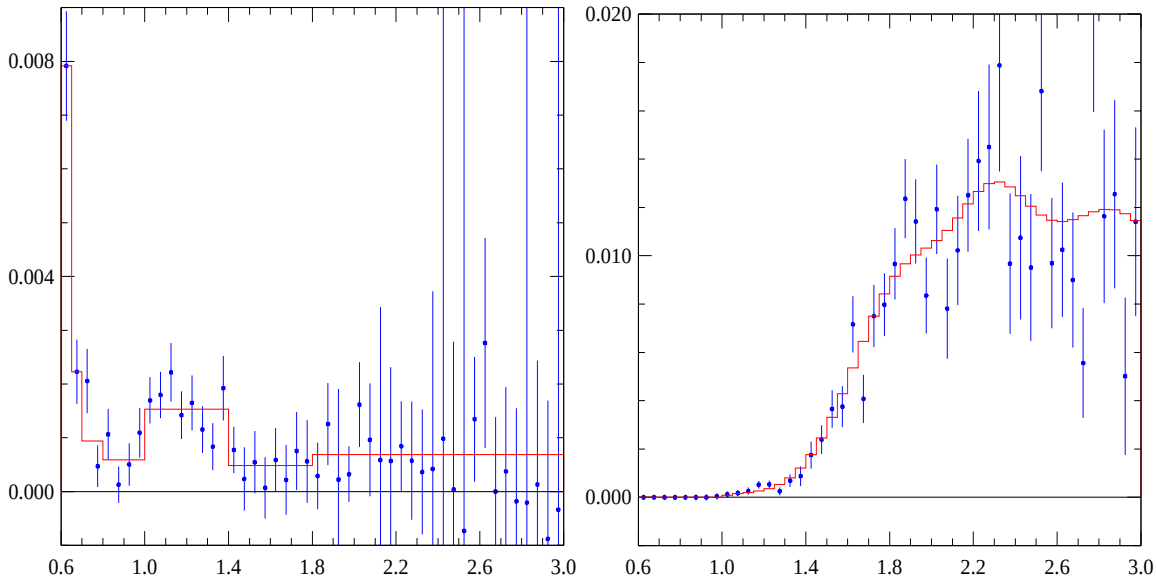

Figure 4.7: TEID (left) and muon (right) fake probabilities as a function of hadron momentum from 0.6 to 3.0 GeV/c.

The track spectrum n_t is corrected for real leptons, which are estimated with the measured electron spectrum n_e, since electrons are measured over a broader momentum range than muons. The total lepton correction is given by the measured electron spectrum divided by the electron identification efficiency ϵ_{eID} times $1 + R_{\mu/e}$, where $R_{\mu/e}$ is the ratio of muons to electrons determined with $B\bar{B}$ Monte Carlo (Fig. 4.8). The small overestimate of the lepton correction due to fake electrons is corrected by the term in the denominator that includes the electron fake rate f_e.

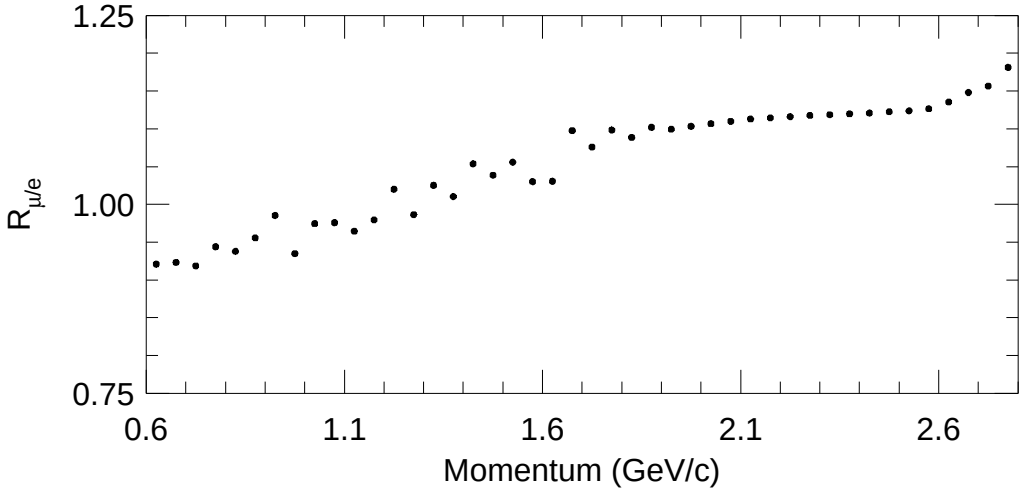

Figure 4.8: Ratio of muons to electrons in reconstructed momentum in Monte Carlo.

The calculation of fakes for an inclusive single-lepton spectrum (e.g. the spectrum of tag leptons) is straightforward: tracks are considered one at a time. Things get more complicated in the dilepton cases, where care must be taken to avoid double-counting the events where both the tag and signal are fakes. This is done with a

two-step iterative procedure.

When calculating the contribution of fake leptons to a dilepton sample, it is useful to think in terms of candidate pairs of tag and signal tracks. If an event has one track above 1.4 GeV and three others above 600 MeV, then there are $1 \times 3 = 3$ candidate-track pairs. If an event has two tracks above 1.4 GeV and two others above 600 MeV, then there are $2 \times 2 + 2 = 6$ candidate track pairs (the "+2" represents the two 1.4 GeV tracks together, where one plays the tag and the other plays the signal, and vice versa). In this way we take into account all the possible tag-signal combinations that we encounter: fake tag-real signal, fake tag-fake signal, real tag-fake signal, and real tag-real signal.

We must collect separate track spectra for electron and muon tags, because of the different J/ψ and other veto cuts (see Sec. 4.3.4). The procedure described below is executed separately for each species of tag, and for like- and unlike-sign signal events. Also, the word "track" in the following is understood to mean tracks that have passed all cuts except for lepton identification.

The first step is to calcuate the number of lepton pairs that get into our sample via a fake tag. To do this, we find track pairs for which one track is above 1.4 GeV and the other is an identified electron above 600 MeV. The momenta of these pairs are collected in a two-dinemsional histogram. Bin-by-bin in signal momentum, the spectrum of fake tags is calculated, and we end up with a two-dimensional distribution for pairs of fake tags and signal electrons. From this we project the momentum spectrum of identified signal electrons with fake tags.

This leaves the correction for real tags with fake signals to be computed. To do

this, we first collect the spectrum of tracks above 600 MeV with an lepton-IDed tag lepton. We then subtract from this the spectrum of identified signals with fake tags that was calculated previously. This track spectrum now contains only signal tracks with real tags. The fake spectrum calculated from this is the real tag-fake signal contribution, avoiding double-counting the fake-fake combination. This added to the spectrum from the previous step gives us our total fake correction.

4.4.2 Veto and Diagonal-Cut Leakage

We estimate the leakage through our vetoes and the diagonal cut using generic $B\bar{B}$ Monte Carlo. To build confidence in our simulation and extract the relevant normalization factors, we fit the spectra of vetoed leptons in Monte Carlo to the corresponding spectra in the data. As described in Sec. 4.3.3, we do not assert electron identification in the Monte Carlo. Prior to fitting, the electron spectra determined from Monte Carlo under the assumption of perfect electron identification are multiplied by the efficiency of our electron identification package to more closely simulate the actual electron identification efficiency (Sec. 4.5.1).

To get the correction for veto leakage, the spectra of unvetoed leptons (as identified by `QQ`) from Monte Carlo are then scaled by the normalization factor returned by the fit. Example fit results are shown in Fig. 4.9. They demonstrate that the Monte Carlo does a very good job of reproducing the distribution observed in data for the J/ψ veto, which is the most important veto in this analysis.

The leakage of same-B secondary signal electrons is estimated with a procedure similar to that described above for the vetoes. In this case, the two-dimensional

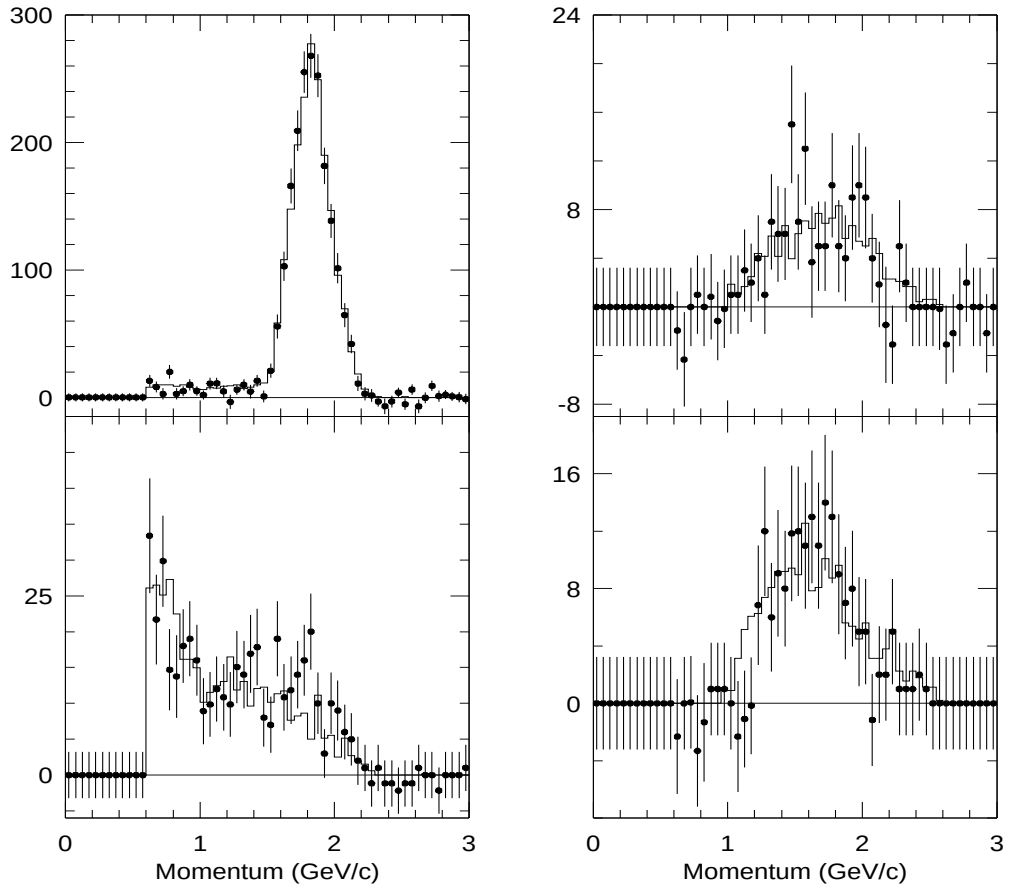

Figure 4.9: Fits of the Monte Carlo spectra of signal electrons with an electron tag that fail one of the J/ψ vetoes to the corresponding spectra in data. The vetoed electrons in Monte Carlo have not been identified by `QQ` as coming from J/ψ decays, and thus include the contribution of mistakenly vetoed tracks, just as in data. The plots are (clockwise from top left): unlike-sign signal electrons from any source with a J/ψ-vetoed electron tag; vetoed unlike-sign signal electrons with a tag electron that passed all vetoes; vetoed like-sign signal electrons with a tag electron that passed all vetoes; and like-sign signal electrons from any source with a J/ψ-vetoed electron tag. The peaking effect in the top left plot is an artifact of the diagonal cut. The Monte Carlo simulation shows excellent agreement with the data.

distribution of $\cos\theta_\ell$ versus signal-electron momentum is fitted. Again, the normalization is determined by fitting the Monte Carlo distributions for same-B secondary signal electrons that fail the diagonal cut (i.e. were successfully eliminated) to the corresponding distribution in data. This factor is then used to scale the Monte Carlo distributions for those that leaked through the cut, providing the background correction to be applied to the electron spectrum. Projections of these distributions and the fits in momentum and $\cos\theta_\ell$ are shown in Fig. 4.10.

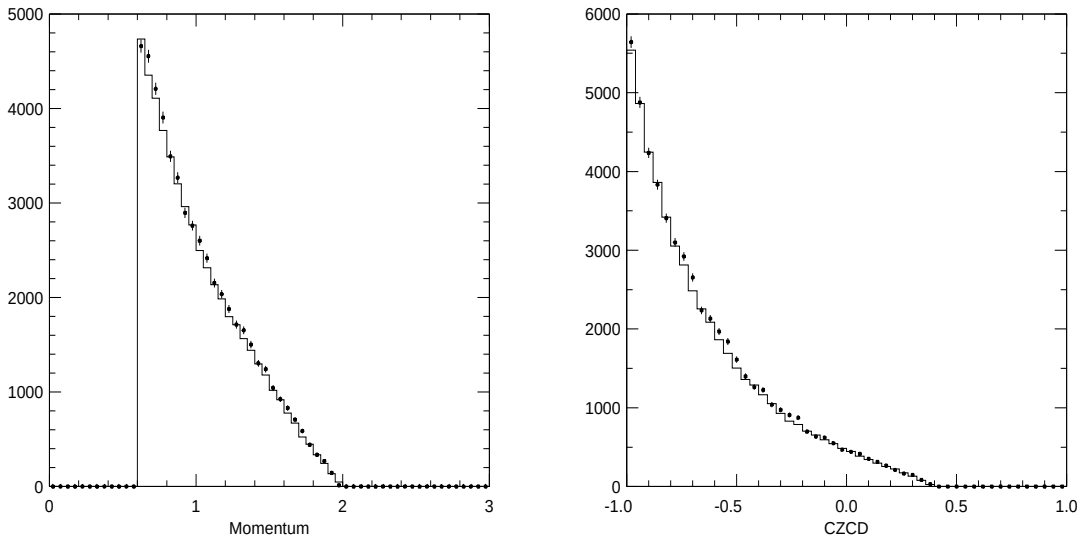

Figure 4.10: Projections in momentum (left) and `CZCD` (right) of same-B secondary fits. The points are data; the histogram is the fitted Monte Carlo.

4.4.3 Nonvetoed Backgrounds

Corrections to the charge-separated spectra for backgrounds from physics sources that we do not veto are obtained directly from Monte Carlo. The distributions from

each source are normalized to the number of $B\bar{B}$'s in the data sample. As with the veto-leakage corrections, we multiply each distribution of electron backgrounds from Monte Carlo by the measured electron identification efficiency.

The unlike- and like-sign electron spectra after all background corrections are shown in Fig. 4.12. The remaining steps are to correct for detection efficiencies and to solve Eqs. 4.1 and 4.2 to get the separated primary and secondary spectra.

4.5 Efficiency Corrections

Since cuts are blind to the source of the track they are acting on, our procedures inadvertently eliminate some electrons that belong in the charge-separated spectra. With the exception of the electron identification efficiency, we use Monte Carlo to determine these losses and calculate corrections to our measured spectra. Where possible, the Monte Carlo has been validated by comparison with data.

Although we discuss the efficiency of all our cuts as though they were applied separately, we actually apply the corrections in just two steps. First, we correct the background-subtracted charged-separated spectra (Fig. 4.12) by the electron identification efficiency. Second, we correct the resulting spectra with one "efficiency" that covers everything besides electron identification. This is the efficiency for all of the other cuts applied simultaneously, as well as the effect of bremsstrahlung in the detector material. It is, in effect, the product of all of the multiplicative corrections that are obtained with Monte Carlo, and properly accounts for any correlations among the components of the overall efficiency.

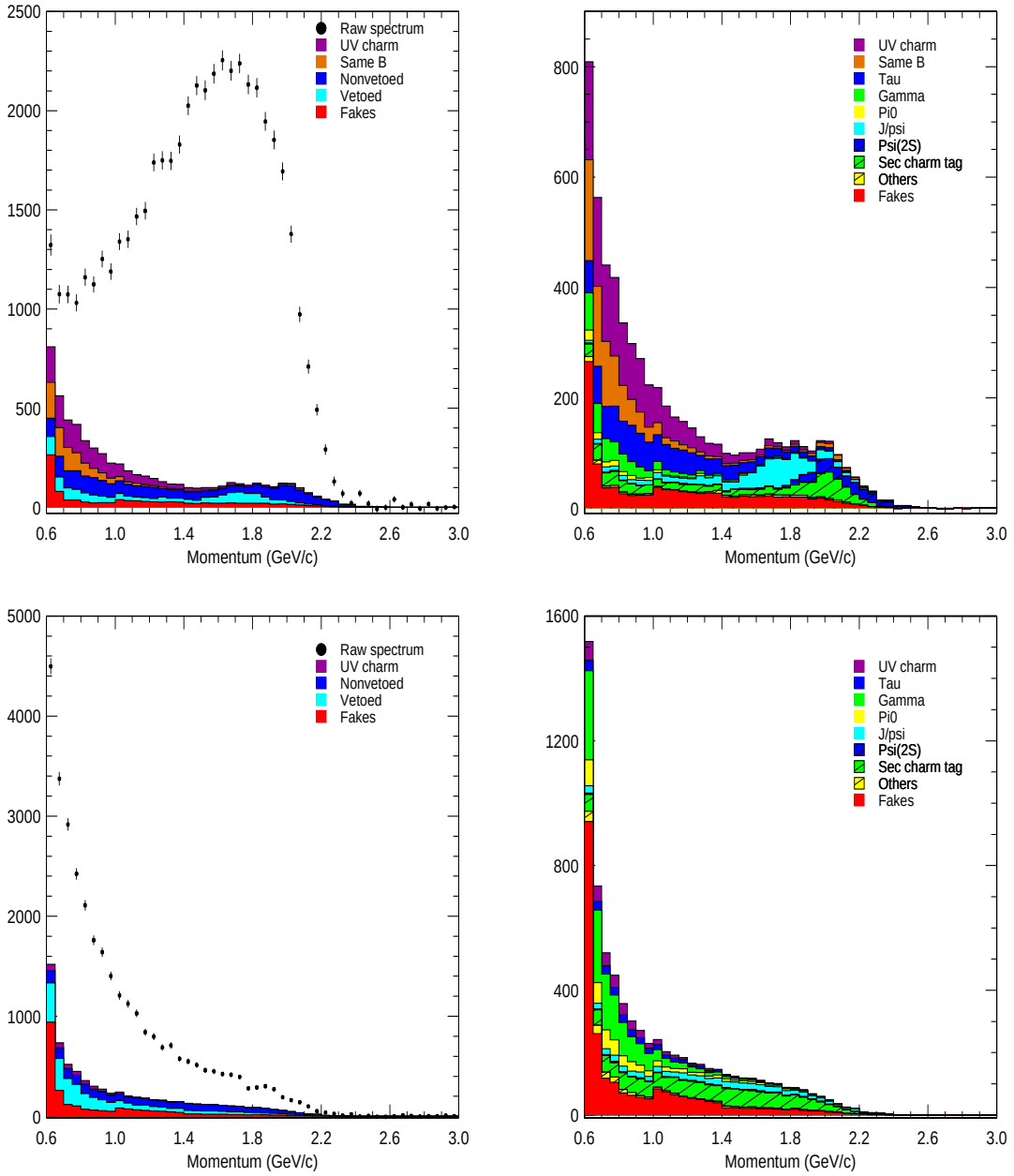

Figure 4.11: Backgrounds in the charge-separated spectra. Each category includes backgrounds to both tag and signal leptons, unless otherwise noted.

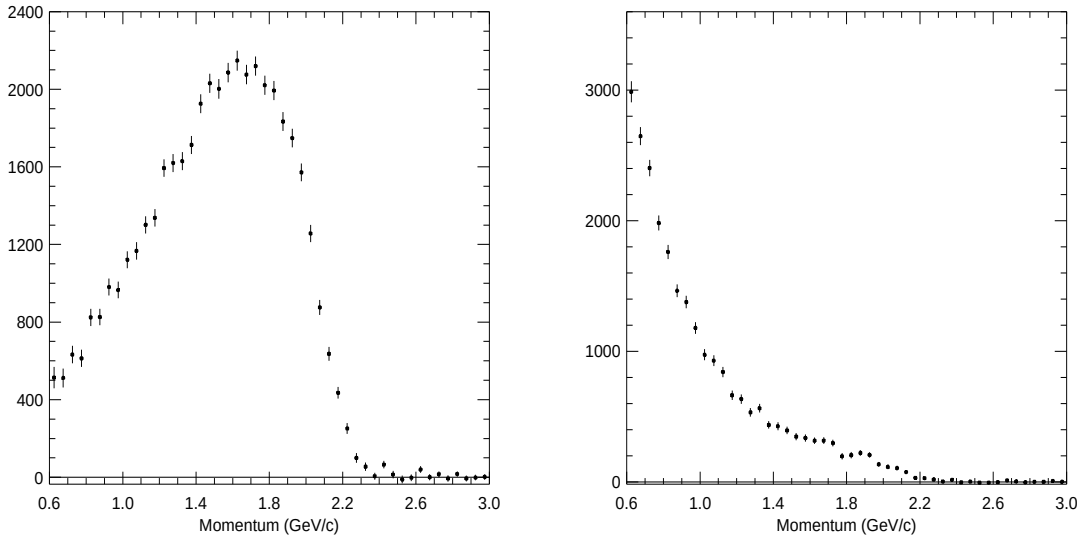

Figure 4.12: Unlike- (top) and like-sign (bottom) electron spectra after all backgrounds have been subtracted.

4.5.1 Tracking and Electron Identification Efficiency

For the recent inclusive end-point $b \to u\ell\nu$ analysis [29], we conducted extensive studies of the ability of the Monte Carlo to simulate the efficiency of track reconstruction and selection with a set of very stringent track-quality cuts. This was done using embedded radiative Bhabha events in both data and Monte Carlo, and was carried out in concert with radiative Bhabha studies of electron identification. Details of these investigations are given in Sec. 4.5.2.

For the tracking study, these events were used to determine the ratio of the track-selection efficiency for data to that for Monte Carlo. This ratio was applied as a correction factor in determining the track-selection efficiency from signal Monte Carlo.

In the previous application of this procedure, to the lepton-energy end-point mea-

surement of $b \to u\ell\nu$ [29, 34], the track-quality cuts were very stringent and the ratio was found to be significantly different from 1. For the current analysis, we use a much less demanding set of track-quality cuts (Sec. 4.3.1), and find the correction factor not to be measurably different from 1 (Fig. 4.15).

The same embedded sample was used to determine the electron identification efficiency for our TEID package, as well as for CEID and other variants used in our systematics studies. The efficiency of our electron identification package is shown in Fig. 4.13.

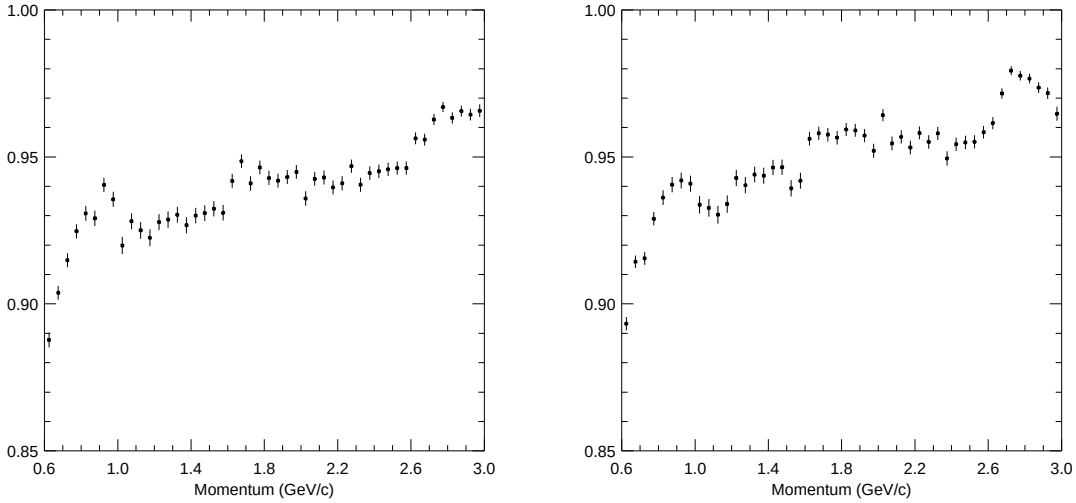

Figure 4.13: Efficiency of our electron identification package in CLEO II (left) and CLEO II.V (right).

4.5.2 The Embedding Study

Since Monte Carlo currently cannot accurately simulate dE/dx, getting the overall efficiency of an electron ID package using dE/dx with Monte Carlo is out of the question. Therefore, we need to measure the efficiency of our electron identification package directly from the data.

To do this, we need a sample of tracks which are *a priori* electrons, so we can ask the electron ID package how many of these tracks it determines to be electrons. Radiative Bhabha events ($e^+e^- \rightarrow e^+e^-\gamma$) are a plentiful and easily selected source of electrons. While the angular distribution tends to be peaked in the beam direction, there are sufficient numbers of tracks in the good-barrel region to measure the efficiency over the entire range of momentum we wish to study.

Care must be taken in using measurements from radiative Bhabhas and applying them to electrons in hadron events, which have very different properties. To put our electrons in a more "hadronic" environment, we take the raw detector hits from obvious radiative Bhabha events, and combine them with the raw hits of a hadron event to make an "embedded" event. The embedded electrons are still distinguishable by their momenta, so we can determine the fraction of the embedded electron tracks in the post-embedding event that pass our electron identification requirements.

The procedure for our embedding study was to overlay the *entire* radiative Bhabha event, not just the hits we think are associated with the desired electron track, onto a hadronic event. Our intention in this was to avoid the complexity and potential uncertainty associated with stripping the information for individual tracks, thus risking throwing out hits that might actually belong to the desired track. Large samples of

such events, distributed over the CLEO II and II.V data sets, were constructed for both data and Monte Carlo. For data, a radiative Bhabha from a given ON-resonance run was embedded into a hadronic event from the same run that passed a cut of the Fox-Wolfram parameter $R_2 < 0.5$ [40] to ensure that it was $B\bar{B}$-like[2] . For Monte Carlo, a simulated radiative Bhabha was embedded into a simulated $B\bar{B}$ event for the same run. In both cases the target hadronic events were selected so that the charged multiplicity distribution for the embedded sample was compatible with $B\bar{B}$ events.

Radiative Bhabha Selection

We select radiative Bhabha events using a prescription created for studies of CEID [35, 36, 37]. We perform a `PASS1` skim, looking for events that pass the following criteria:

- one or two `TRIO`-approved tracks,
- at least three showers with $E \geq 150$ MeV,
- total energy in the calorimeter ≥ 6 GeV,
- minimum opening angle between any pair in a triplet of showers is 18°, and

[2] R_2 is defined as the ratio of the Fox-Wolfram moments H_2/H_0, where

$$H_k = \frac{1}{s}\sum_{i=1}^{n}\sum_{j=1}^{n}\left[|\vec{p_i}||\vec{p_j}|P_k(\cos\phi_{ij})\right]. \tag{4.4}$$

Here n is the number of particles in the event, s is the center-of-mass energy squared, ϕ_{ij} is the angle between the momentum vectors for particles i and j, and P_k is a kth order Legendre polynomial. Values of R_2 near zero represent "spherical" events, such as $B\bar{B} \to hadrons$, while R_2 values near one represent more "jet-like" events, with the back-to-back pattern characteristic of $e^+e^- \to q\bar{q}$ $(q = u, d, s, c)$ events.

- energy of the best triplet of showers is $\geq$ 900 MeV.

After this initial skim, events must pass a second layer of cuts, performed in `PASS2`, before they are selected for embedding:

- `PASS1` criteria using `PASS2`,
- exactly two tracks, of opposite charge,
- at least one track with $p \leq 3$ GeV/c,
- each track matches to one of the four biggest showers,
- one of the four biggest showers is not matched to a track, and
- energy of the matched showers $\geq$ 3.5 GeV.

Hadron Bed Selection

To end up with an embedded event that is similar to a $B\bar{B}$ event, we choose suitable hadron events in which to embed the radiative Bhabha event with a similar two-step system to that of choosing the radiative Bhabha. Events classified as hadrons were skimmed in `PASS1`, and the sample further culled in `PASS2` by requiring that the events pass the following criteria:

- `R2` ≤ 0.5,
- between 5 and 12 tracks, and
- no tracks with `R2ELEC` ≥ 0.

Monte Carlo Samples

Although embedding Monte Carlo radiative Bhabhas will not give us any insight into electron ID, it will allow us to evaluate the ability of the Monte Carlo to simulate tracking. In this vein, we construct samples of Monte Carlo-generated Bhabha and hadronic events to embed and compare with results obtained from embedded data events.

Since the vast majority of Bhabha-type events do not have the low momentum good barrel track we desire, we preselect `QQ` events to shape the initial sample of Bhabhas by requiring:

- an electron (or positron) with $|\cos\theta| \leq 0.7071$ and $0.6 \leq |\vec{p}_{gen}| \leq 3.0$ GeV/c,
- a photon with $|\cos\theta| \leq 0.85$ and $|\vec{p}_{gen}| \geq 150$ MeV/c, and
- the other electron (or positron) with $|\cos\theta| \leq 0.85$.

After `QQ`, we run `CLEOG` on these events, and then insert noise hits from a random trigger event. We then apply the same `PASS2` radiative Bhabha criteria as described for the data. The momentum and distributions for this Monte Carlo sample are quite similar to our data sample (see Fig. 4.14).

For the hadron beds, we simply generate generic $B\bar{B}$ events, insert noise, and apply the same `PASS2` hadron bed criteria as described for the hadron beds from data.

Because Bhabha and hadron events in the data each have their own detector noise, the embedded events will have twice the level of noise than usual. Since we want our

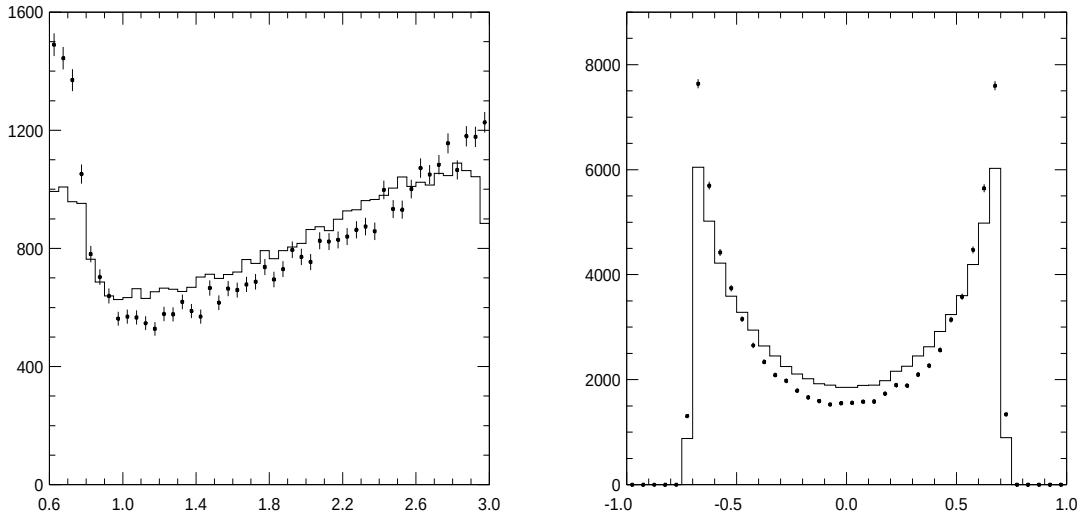

Figure 4.14: Comparison of the momentum *(left)* and polar angle `CZCD` *(right)* distributions of good-barrel tracks for pre-embedded radiative Bhabha events for data (points) and Monte Carlo (histogram).

Monte Carlo to mirror the data as much as possible, we insert random trigger events into both the Bhabha and hadron bed events, thus giving us "double noise" in the embedded Monte Carlo event. Care was taken to ensure that the same random trigger event was not inserted into both the Bhabha event and its hadron bed event.

Embedding

Now that we have our samples of radiative Bhabha and hadron events from the data, and similar samples from Monte Carlo, we are ready to embed. In this study, we embed Bhabhas from data into hadron beds from data, and Bhabhas from Monte Carlo into hadron beds from Monte Carlo.

After embedding, we can find an embedded track using the quantity

$$\cos\Delta\theta = \frac{\vec{p_r} \cdot \vec{p_e}}{|\vec{p_r}||\vec{p_e}|}$$

where $\vec{p_r}$ is the momentum of the track in the raw radiative Bhabha event and $\vec{p_e}$ is the momentum of the track in the embedded event. The track in the embedded event with the highest $\cos\Delta\theta$ is considered to be found if it satisfies $\cos\Delta\theta \geq 0.99$.

Track Quality In Data and Monte Carlo

One of the payoffs of all this embedding is the confidence we gain in the Monte Carlo to simulate track reconstruction for our track-quality cuts. Figure 4.15 shows the ratio of efficiencies of our track-quality cuts in data and Monte Carlo. We were looking for a correction factor to apply to our Monte Carlo to to make it more "data-like", but since this ratio is essentially unity for all momenta, we determined that

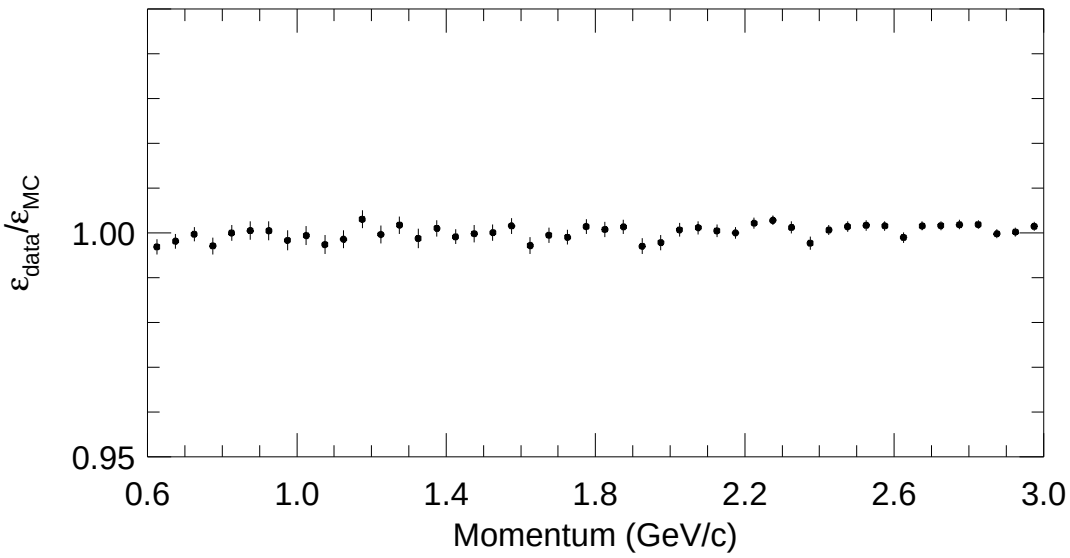

Figure 4.15: Efficiency ratio of track-quality cuts in embedded data and embedded MC.

the Monte Carlo does a good enough job simulating track reconstruction efficiency, and no correction needs to be applied. Note that this last statement is applicable to our specific package of track-quality cuts; other track-quality requirements can cause deviation from this level of agreement between data and Monte Carlo (see Ref. [29], the lepton energy endpoint analysis, for an example).

Electron Identification Efficiency

We use the embedded data sample to measure the efficiency of electron identification for TEID and for the several different permutations of TEID used in the EID systematic error study described in Sec. 5.5.

In addition to the $\cos\Delta\theta$ requirement for embedded-track finding, we also require

that the track pass the PVRTX cut for reasons described in Sec. 4.3.3. We measure the electron-identification efficiency by looking at "found" embedded tracks passing our track-quality cuts (Sec. 4.3.1) to see if they also pass our electron-indentification requirements. The number passing our electron-identification cuts divided by the total number of good-track-quality embedded tracks is the efficiency.

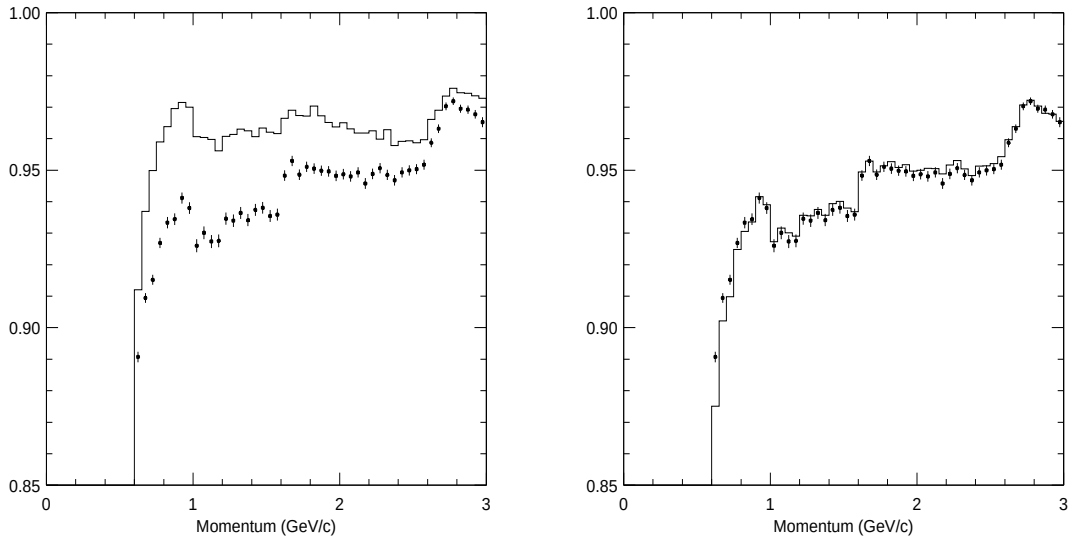

Figure 4.16: *Left:* TEID efficiencies for reweighted unembedded (histogram) and embedded (points) radiative Bhabha events. *Right:* TEID efficiencies for unreweighted (histogram) and reweighted (points) embedded radiative Bhabha tracks.

We also correct for the difference in the angular distributions of radiative Bhabha tracks (see Fig. 4.14) and $B\bar{B}$ events. This is done by simply reweighting the radiative Bhabha track sample so that each momentum bin has a flat polar angular distribution. Reweighted distributions of the TEID efficiency for unembedded and embedded radiative Bhabha tracks are shown in Fig. 4.16, as are the TEID efficiencies

for unreweighted and reweighted embedded radiative Bhabha tracks.

4.5.3 Other Efficiencies and Detector Bremsstrahlung

The efficiencies of the primary spectrum passing the track-quality, veto, diagonal, and fiducial cuts are determined using Monte Carlo, as is the correction for detector bremsstrahlung.

Since our default Monte Carlo sample contains only $B \to X_c \ell \nu$ decays, we only get an efficiency measurement for tracks below 2.3 GeV/c. To get a measurement for tracks between 2.3 and 2.6 GeV/c, we use the `INCLGEN` sample of $B \to X_u \ell \nu$ Monte Carlo. Above 2.6 GeV/c, we use the value of the efficiency in the 2.6 GeV/c bin.

The overall efficiencies for signal electrons from semileptonic B decays with unlike-sign and like-sign tags are shown in Fig. 4.17. The principal source of difference between the two cases is the diagonal cut. Application of the overall efficiency corrections to the raw unlike-sign and like-sign spectra results in the fully corrected spectra shown in Fig. 4.18.

4.6 Primary Spectrum Extraction

Now that we have our fully corrected charge separated spectra, we are ready to extract the primary spectrum. In this section, we explain the method used to perform this extraction.

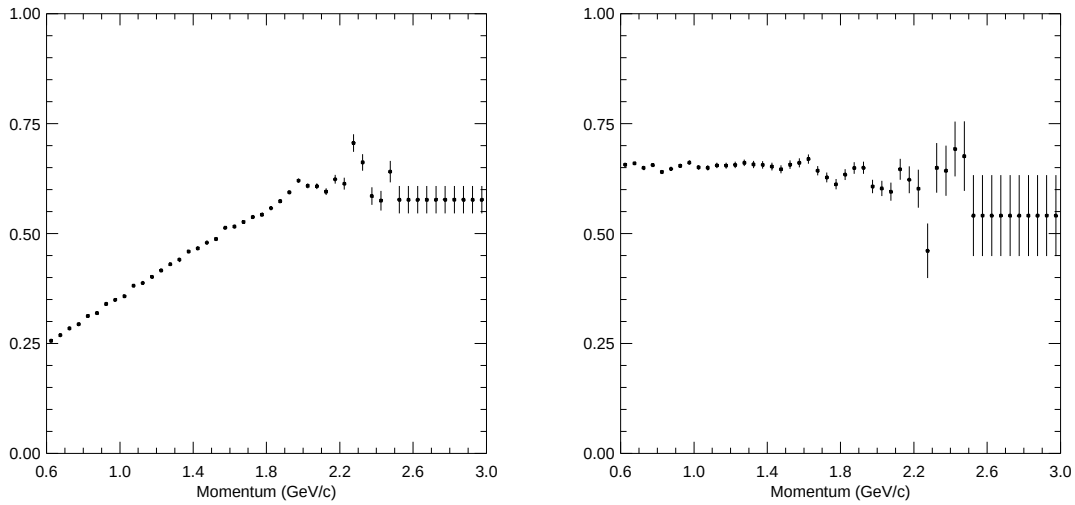

Figure 4.17: Overall efficiencies for unlike-sign (left) and like-sign spectra. Detector bremsstrahlung is included in this correction.

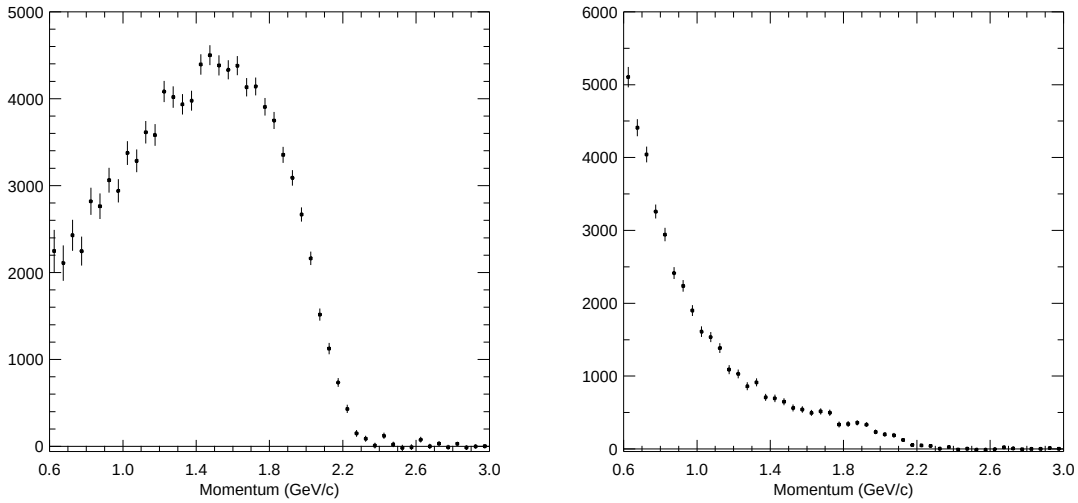

Figure 4.18: Fully corrected unlike-sign (left) and like-sign spectra. These are the charged-separated spectra that are passed to Eqs. 4.1 and 4.2.

4.6.1 Correction to Secondary Spectrum

The ratio of charged D mesons to neutral D mesons in B^+B^- events is different from that in $B^0\bar{B}^0$ events. The semileptonic branching ratio of charged D mesons is different from that of neutral D mesons. Neutral B mesons mix, while charged B mesons do not. Separately, these three effects would not trouble us. Together, they undermine an assumption in the derivation of Eqs. 4.1 and 4.2: the assumption that the secondary spectra in charged B and neutral B events are identical.

An examination of the Monte Carlo, which represents quite well the state of the art as compiled by the PDG [10], shows that this assumption does not hold. A QQ study of B decays determined that 8.22% of charged B decays will yield a secondary electron (for future reference, call this number R_+). The fraction of neutral B decays that yield a secondary electron (call this R_0) is 10.03%. Of these neutral B secondaries, $\chi_0 = 17.1\%$ will be from B^0's that mixed, and will therefore be of the opposite sign to the tag lepton; the rest will have the same sign as the tag. (All the secondaries in charged B events will be same-sign.) Refer to Fig. 4.19 for more detail.

To correct for this effect, we would like to rewrite Eqs. 4.1 and 4.2, replacing $\frac{d\mathcal{B}(c)^{oppB}}{dp}$ with R_0 in the terms involving mixing. (The same-B term in Eq. 4.1 is eliminated by the diagonal cut.) This gives the modified equations[3]:

$$\frac{dN(\ell^\pm e^\mp)}{dp} = N_\ell \left[(1 - f_0\chi_0)\frac{d\mathcal{B}(b)}{dp} \; + \; f_0\chi_0 R_0(p) \right], \text{and} \tag{4.5}$$

$$\frac{dN(\ell^\pm e^\pm)}{dp} = N_\ell \left[\chi_0 \frac{d\mathcal{B}(b)}{dp} \; + \; \left(\frac{d\mathcal{B}(c)}{dp} - f_0\chi_0 R_0(p) \right) \right]. \tag{4.6}$$

[3]At this point, we will drop the explicit efficiency factors that appear in Eqs. 4.1 and 4.2, as they have already been accounted for in the fully-corrected spectra.

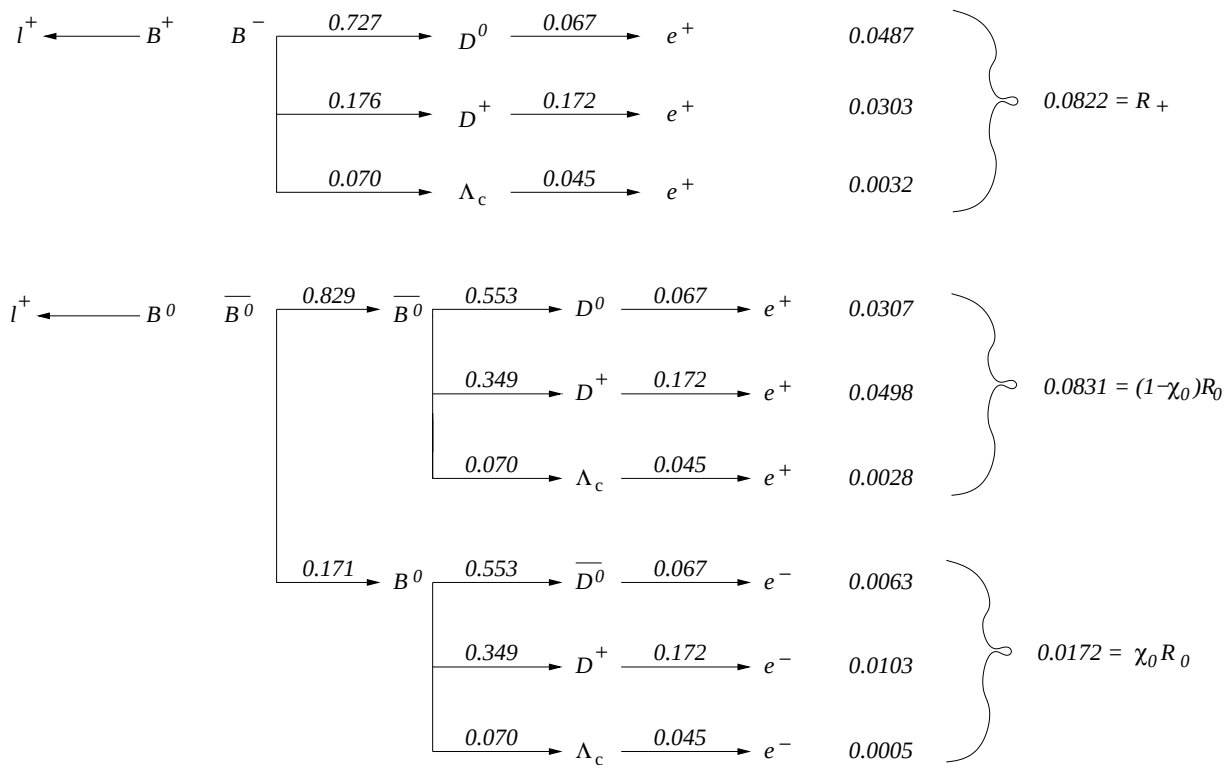

Figure 4.19: Breakdown of sources of secondary electrons. The branching ratios are from MC.

Since it is not feasible to determine which events are B^+B^- and which are $B^0\bar{B}^0$, we need to replace $R_0(p)$ with $\frac{d\mathcal{B}(c)}{dp}\Delta(p)$, where

$$\Delta(p) = \frac{R_0}{\frac{d\mathcal{B}(c)}{dp}} = \frac{1}{(1-f_0)\frac{R_+}{R_0} + f_0}. \tag{4.7}$$

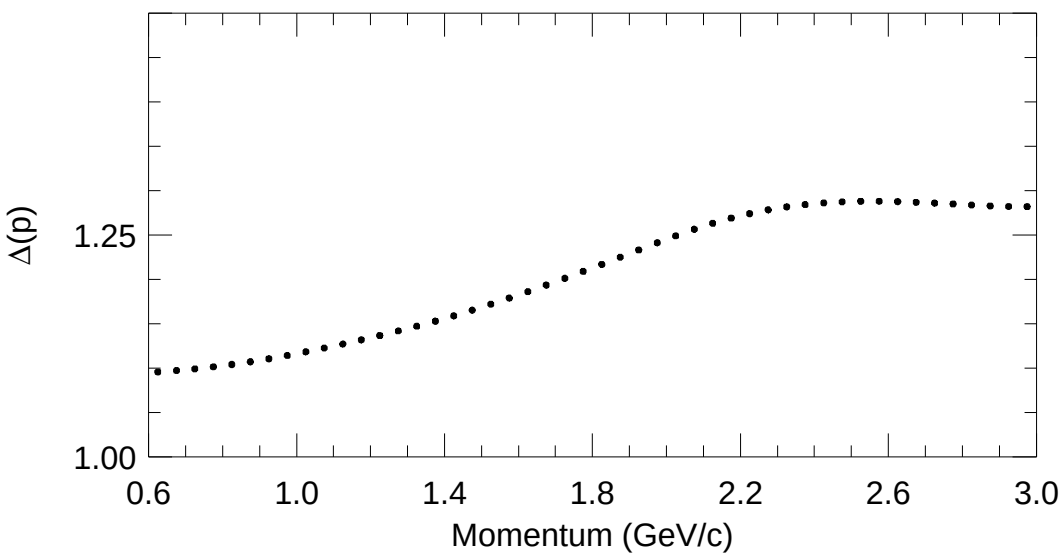

Figure 4.20: Secondary correction factor $\Delta(p)$

Making the substitution and solving these equations, we get expressions for the primary and secondary spectra:

$$\frac{d\mathcal{B}(b)}{dp} = \frac{1}{(1-[\Delta(p)+1]\,\chi)}\frac{1}{N_\ell}\left[[1-\chi\Delta(p)]\frac{dN(\ell^\pm e^\mp)}{dp} - \chi\Delta(p)\frac{dN(\ell^\pm e^\pm)}{dp}\right], \text{and} \tag{4.8}$$

$$\frac{d\mathcal{B}(c)}{dp} = \frac{1}{(1-[\Delta(p)+1]\,\chi)}\frac{1}{N_\ell}\left[\chi\frac{dN(\ell^\pm e^\mp)}{dp} - (1-\chi)\frac{dN(\ell^\pm e^\pm)}{dp}\right], \tag{4.9}$$

with $\chi \equiv f_0\chi_0$.

4.6.2 Solving the Equations

We now have everything we need to get the primary spectrum. Plugging the fully-corrected charge-separated spectra from Fig. 4.18 into Eqs. 4.8 and 4.9, we obtain the primary and secondary spectra shown in Fig. 4.21.

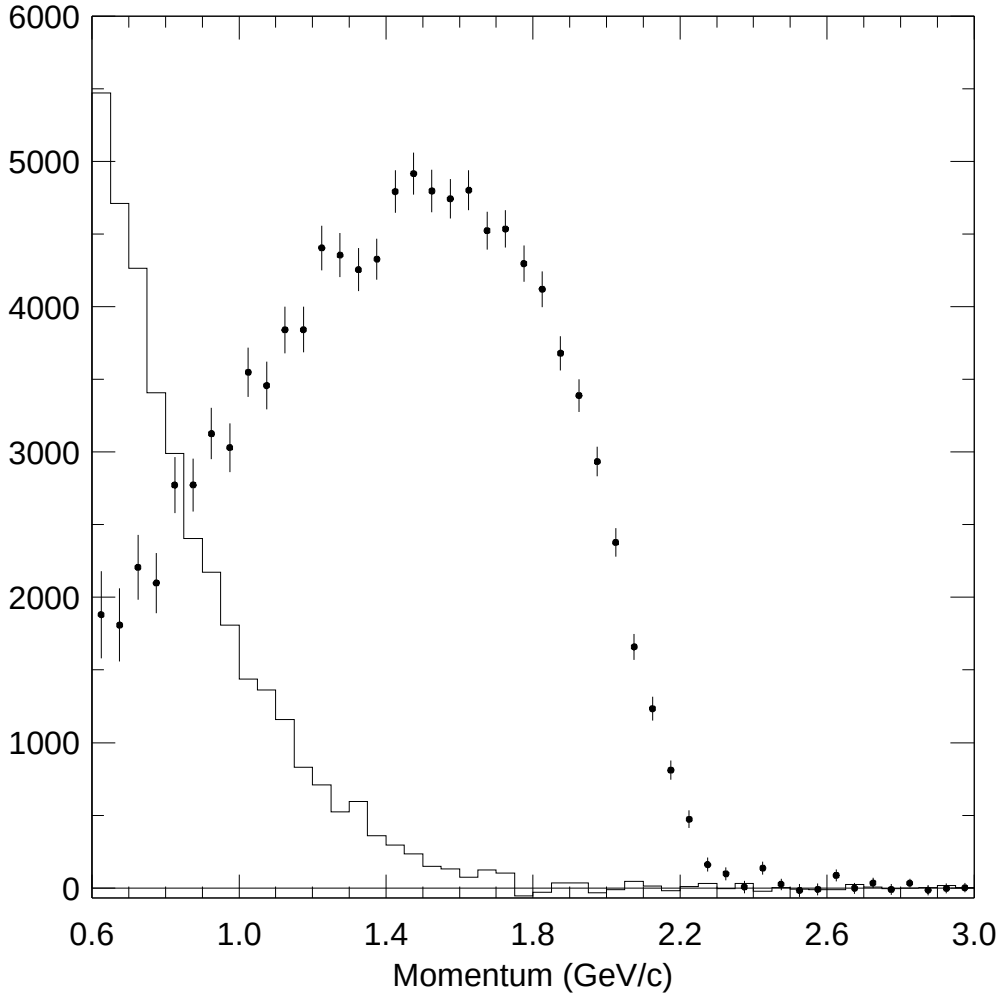

Figure 4.21: Primary (points) and secondary spectra (histogram).

The primary spectrum in Fig. 4.21 is used as shown to measure the $B \to Xe\nu$ branching ratio (see Chap. 6). One correction to this spectrum, the subtraction of semileptonic $B \to X_u \ell\nu$ decays, must be made before we can extract moments (see Chap. 7).

4.7 Cross-Checks of the Semileptonic Spectra

Throughout our analysis cross-checks with Monte Carlo have provided an invaluable tool for validating the techniques we have used and the specific implementations in our code. These tests also provide useful feedback on the overall accuracy of our Monte Carlo generators in predicting the shape and scale of the semileptonic decay spectrum for secondary charm. These studies are described in Sec. 4.7.1.

Once we have generated our lepton spectra it is also reasonable to ask if we get consistent results when we subdivide the data sample in obvious ways. In Sec. 4.7.4 we give the results separately for electrons with electron and muon tags, positive and negative tags, high-momentum and low-momentum tags, and for CLEO II and CLEO II.V.

4.7.1 Analyzing Monte Carlo as Data

Since the Monte Carlo is a data set for which we have access to the "final answer," we use it to test our analysis package. We treat the full-`CLEOG` Monte Carlo sample (Sec. 4.2.1) as if it were data, apply the various corrections (mostly determined with the same Monte Carlo sample), and then see if our analysis package delivers the

correct "final answer." We took advantage of the ability to peek at the true answer at intermediate stages of the analysis as well, although not all of the critical steps could be checked. For example, this procedure provides no useful information about the correction for fake leptons.

Fig. 4.22 shows the fully-corrected unlike- and like-sign spectra from the MC-as-data analysis, compared to what QQ says they should be at that point in the analysis. The agreement is nearly perfect, as it should be.

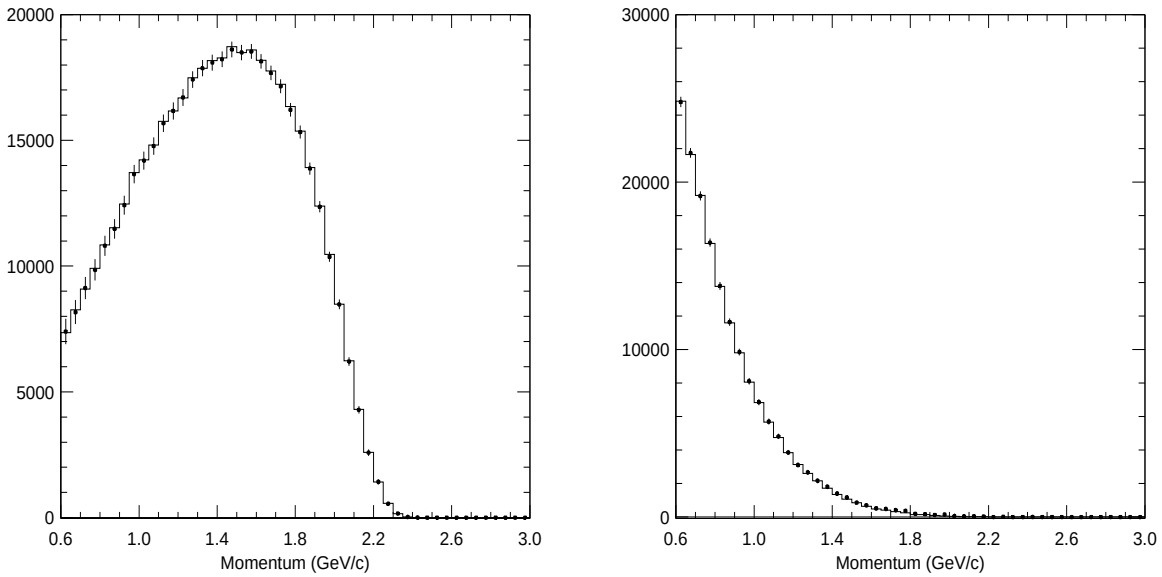

Figure 4.22: Results of MC-as-data analysis (points) compared to QQ (solid line) for the fully-corrected unlike-sign (left) and like-sign spectra.

The MC-as-data analysis started as a check on our bookkeeping abilities: to ensure that efficiency corrections, background corrections, and algebra were being done properly. It proved also to be a very useful aid in the development of our analysis

tools and their implementation. It also allowed us to test some assumptions of the analysis method itself. In trying to reproduce the primary spectrum, we determined that we needed to incorporate the $\Delta(p)$ factor in Eqs. 4.8 and 4.9 (Sec. 4.6.1), while trying to extract the branching ratio uncovered a problem with the relative event selection efficiency correction (Sec. 6.1.2) in the previous analysis.

The MC-as-data analysis also provides a good laboratory for studying the ability of the Monte Carlo to model secondary lepton production by comparing distributions of tracks flagged as secondaries by the analysis procedure in the data and in the MC-as-data. We study two sources of secondaries this way. By looking at what is eliminated by the diagonal cut (Sec. 4.1.1), we learn about same-B secondaries, and by comparing the final secondary spectrum (the solution to Eq. 4.9), we learn about the opposite-B secondaries.

4.7.2 MC as Data Study of Same-B Secondaries

The diagonal cut was designed to suppress signal electrons coming from the charmed daughter of the same B that decayed semileptonically to produce the tag lepton. Therefore it follows that the sample of signal electrons failing the cut will be enriched in these same-B secondaries. Since about 98% of the same-B secondaries fail the diagonal cut, examining these events in data and in Monte Carlo will give us a handle on our correction for same-B secondary events leaking through the diagonal cut. We have already used this handle in Sec. 4.4.2 to determine the normalization of the same-side-secondary background, which was estimated by Monte Carlo. The shapes were shown to agree quite well both in the two-dimensional space of cosine of opening angle

vs. momentum and in the projections onto momentum and `CZCD`, which are shown in Fig. 4.10. The fit was reasonable, with a χ^2 of 1166 for 980-2 degrees of freedom. The normalization of the same-side-secondary component of the fit was 0.2121, while the expected value from dead-reckoning was 0.2102 (based on the known numbers of $B\bar{B}$ events). Because the normalization of the opposite-B component was also free in this fit, it is somewhat difficult to interpret the agreement quantitatively. It appears to be within about 10%, however, which is quite good.

4.7.3 MC as Data Study of Opposite-B Secondaries

We can also look at the "other" solution of Eqs. 4.8 and 4.9 to test the Monte Carlo's simulation of the opposite-B secondaries measured in data. Fig. 4.23 shows the one-parameter fit of the Monte Carlo prediction of the secondary spectrum to the measured data points. The χ^2 of is 21 for 28-1 degrees of freedom, and the normalization parameter of 0.2196 compares to a dead-reckoned expectation of 0.2102. The Monte Carlo reproduces the shape of the spectrum quite well, and while it has too few opposite-B secondaries, the difference is remarkably small. Quantitatively, the ratio of data to Monte Carlo is 1.045 ± 0.013 (statistical error only) for the full spectrum, and above 1.0 GeV/c the ratio is 1.07 ± 0.03.

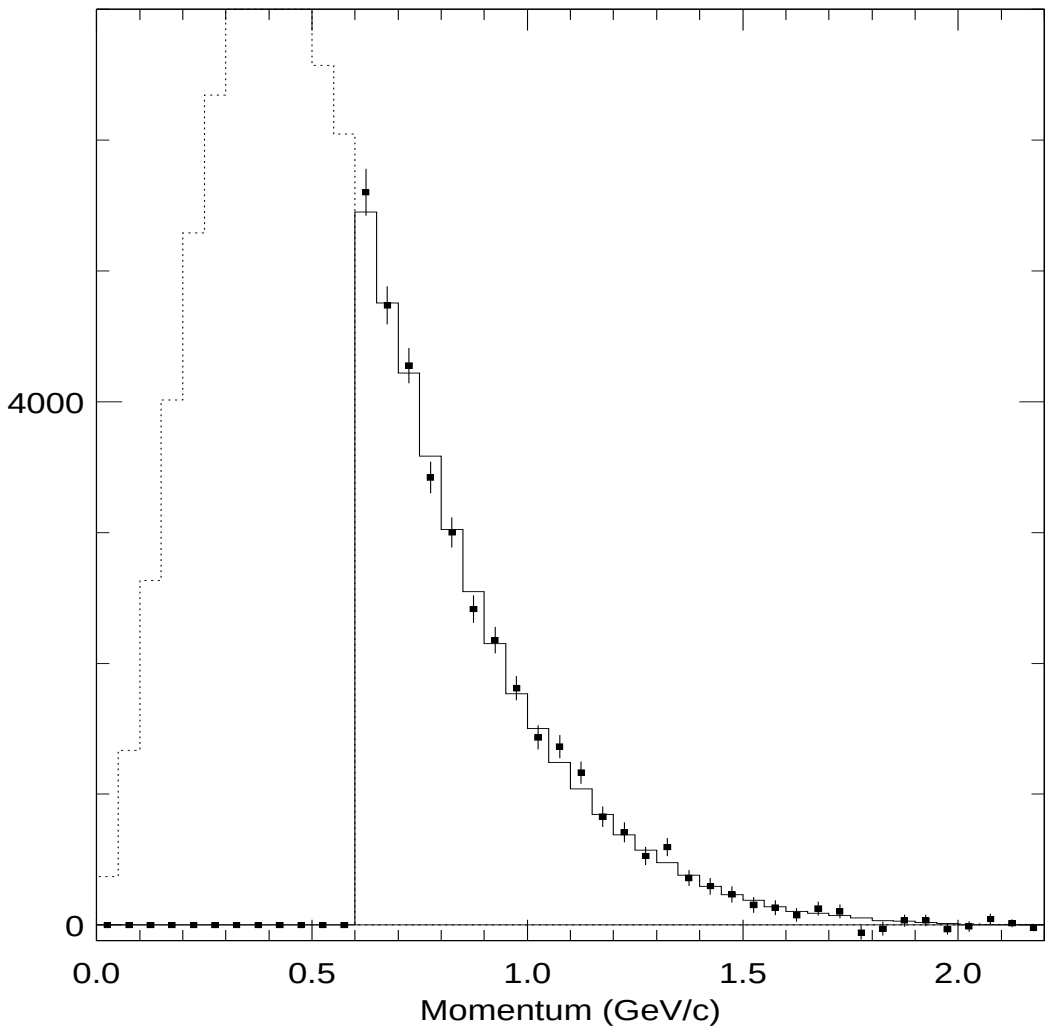

Figure 4.23: Fit of the secondary electron spectrum from the opposite-B sample. The points are data and the fitted histogram is the Monte Carlo.

4.7.4 Consistency Checks: Splitting the Data Sample

CLEO II vs II.V

In analyzing our data we keep CLEO II and CLEO II.V separate up to the point of final processing ($B \to X_u \ell \nu$ subtraction, computation of the yield and moments). Fig. 4.24 shows the separate primary-spectrum measurements for CLEO II and CLEO II.V, normalized to unit area. There is generally excellent agreement. Even at the low-energy end, where material differences between the two detector configurations should be most pronounced, the points agree within *statistical* errors, which are considerably smaller than the systematic uncertainties.

Electron vs Muon Tags

Throughout our analysis, we make no distinction between events with electron tags and those with muon tags (except for the purposes of applying fake-lepton corrections and vetoes). We certainly expect no significant differences between them, even though the momentum-dependent acceptance of the muon detector should result in a higher mean energy for muon tags than for electron tags. The electron-tagged primary spectrum and muon-tagged primary spectrum are plotted in Fig. 4.25, both normalized to unity. This figure illustrates that the shapes of the distributions agree very well, and the efficiency-corrected yields are consistent within 0.7% ($\sim 0.5\ \sigma$).

Positive vs Negative Tags

We also make no distinction at all between events with positively- and negatively-charged tags. In splitting the data this way we did not have charge-separated fake rates available, so a small disagreement between the spectrum with positive tags and the spectrum with negative tags is expected. As can be seen in Fig 4.26, the negatively-tagged primary spectrum and the positively-tagged primary spectrum agree very well.

High vs Low-Momentum Tags

The last dataset splitting exercise was to partition the data by tag momentum in two bins; tag momentum above and below 1.75 GeV (which gave us a roughly equal partition). Again, we expect no disgreement between the two samples. And again, the agreement between the high-p-tagged primary spectrum and low-p-tagged primary spectrum is remarkable ($\chi^2 = 19.7$ for $40 - 1$ d.o.f.). The spectra, both normalized by their respective number of tags, are shown in Fig 4.27.

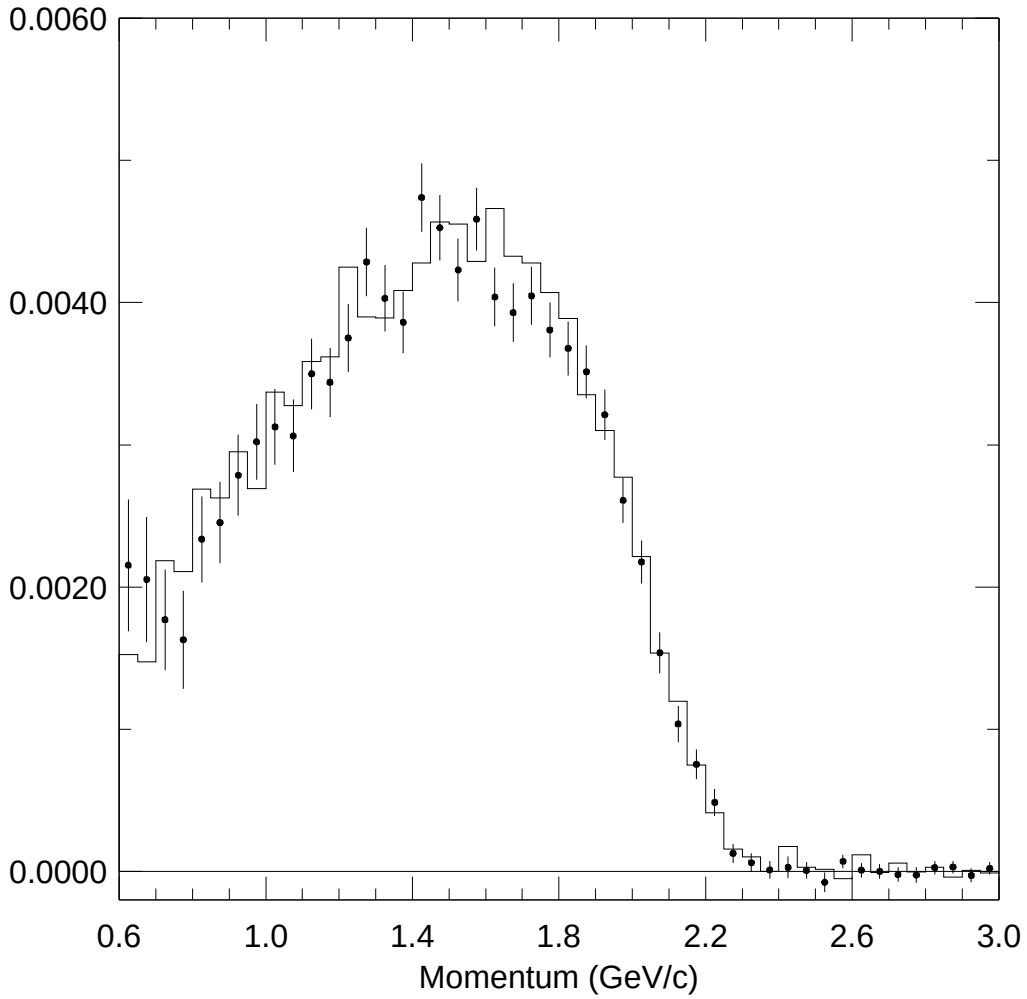

Figure 4.24: Primary spectra from CLEO II (points) and CLEO II.V (histogram) events. Plots are normalized to their respective number of tags.

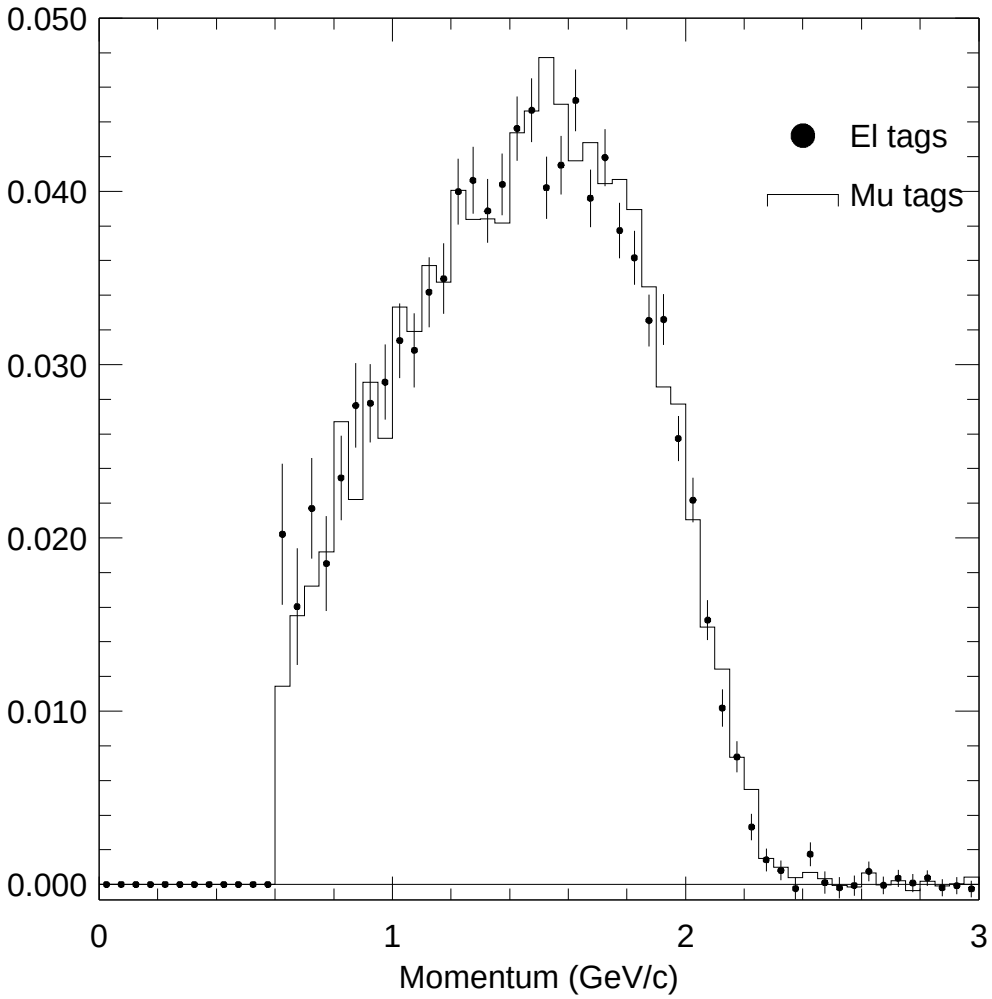

Figure 4.25: Primary spectra from electron-tag (points) and muon-tag (histogram) events. Plots are normalized to equal areas.

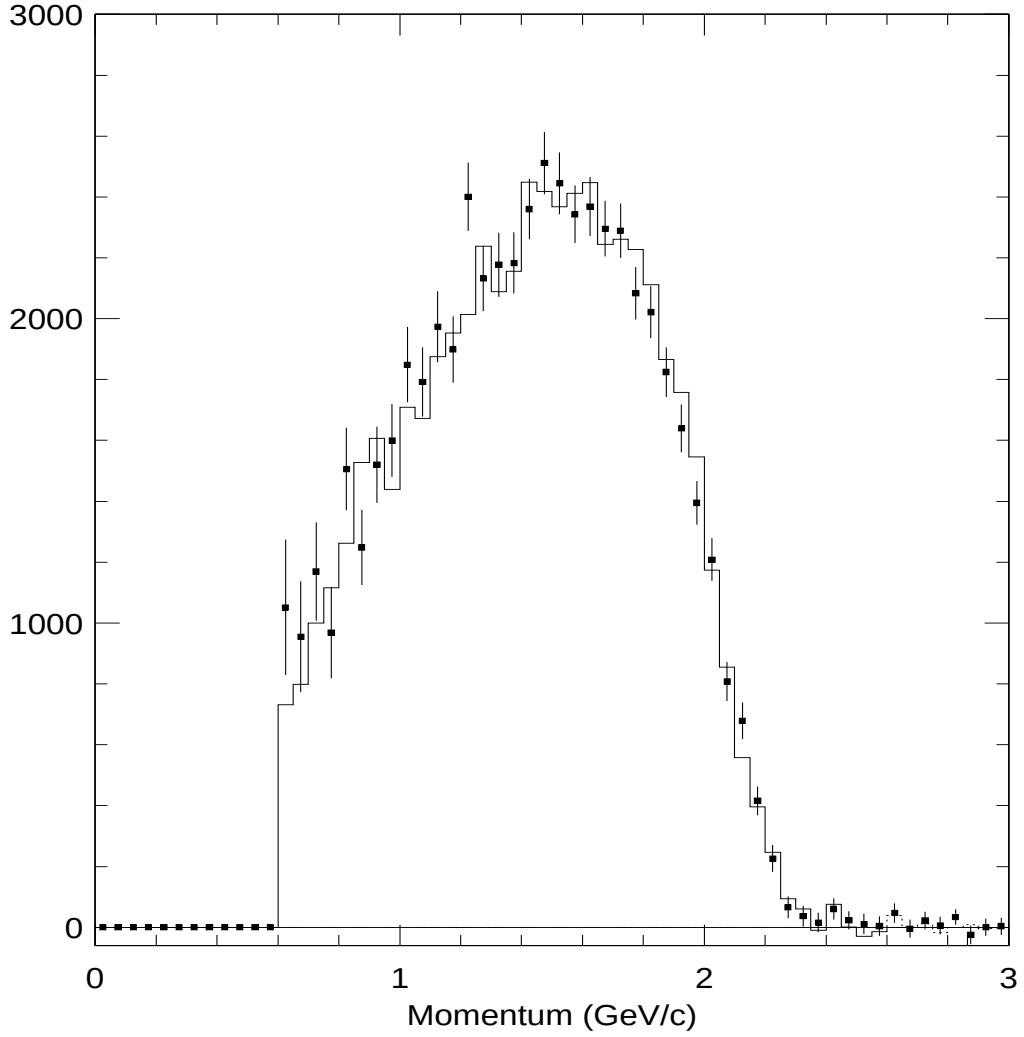

Figure 4.26: Primary spectra from positive tag (points) and negative tag (histogram) events. Plots are not normalized.

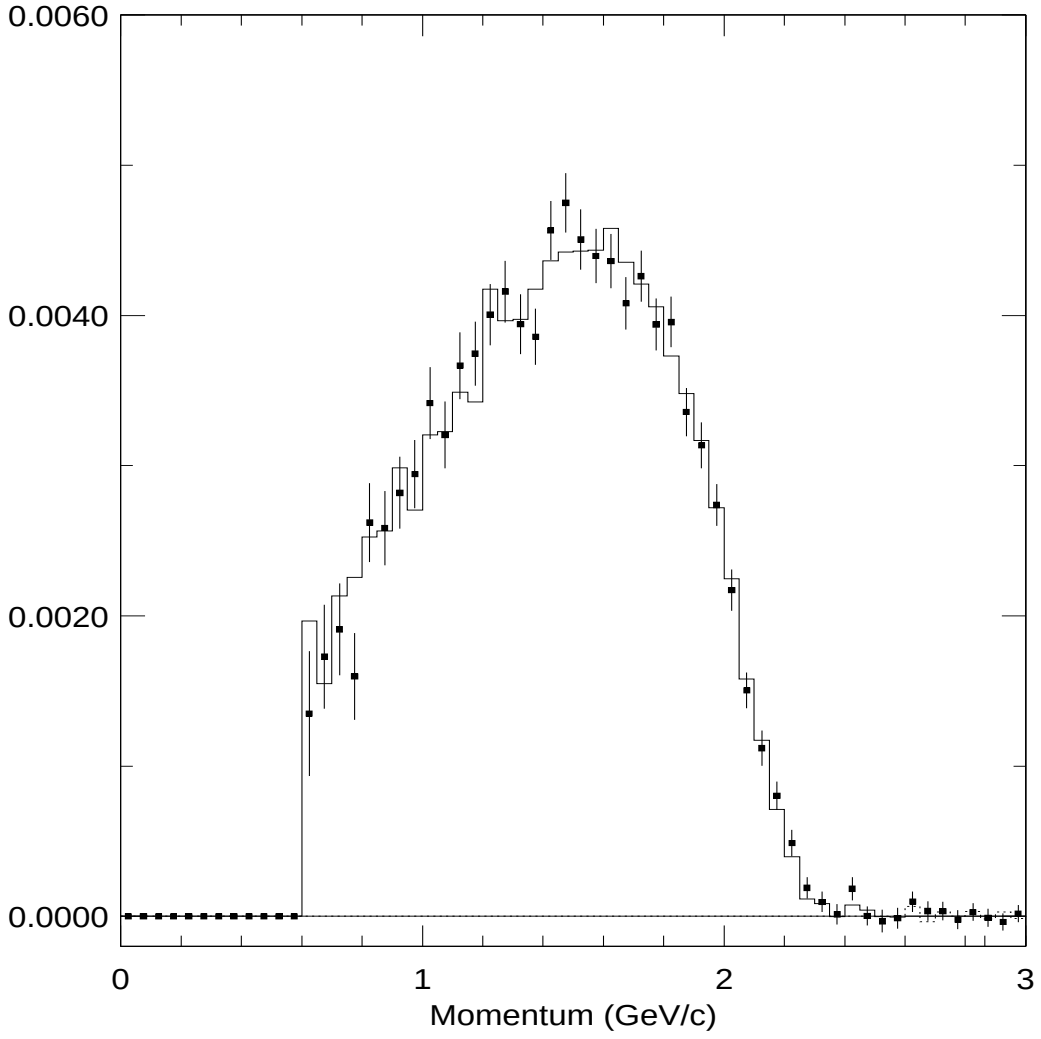

Figure 4.27: Primary spectra from high-p tag (points) and low-p tag (histogram) events. Plots are normalized to their respective number of tags.

CHAPTER 5

Systematic Errors

Our experimental observables, the B semileptonic branching fraction and the lepton-energy moments, are subject to systematic uncertainty from a large set of potential sources. In this section, we describe these sources and the techniques that we use to assess their effects on the observables. The actual systematic uncertainty estimates are presented in Chap. 6 and Chap. 7 for the branching fraction and the moments, respectively.

5.1 Veto-Leakage Corrections

These corrections are computed using momentum spectra determined from Monte Carlo with normalizations obtained by fitting data, as was described in Sect. 4.4. This procedure renders our corrections insensitive to uncertainty in the rates of the contributing processes, but leaves us with uncertainty in the detailed descriptions, for example of the momentum spectra. In the case of the J/ψ veto, we are very confident in the modeling in `QQ` and `CLEOG`, since the mixture of decays has been tuned to agree with exclusive branching ratios and the inclusive J/ψ momentum spectrum. We believe our estimate of a $\pm 5\%$ systematic uncertainty on the subtraction of unvetoed

J/ψ's to be quite conservative. For the π^0 and photon-conversion vetoes, there is more uncertainty in the simulation of the detector response, and we take $\pm 20\%$. For each of these, we have fluctuated the correction upward and downward by these amounts and taken the systematic uncertainty to be one half of the difference between them.

5.2 Diagonal Cut Leakage Correction

The background due to same-B secondaries that are not eliminated by the diagonal cut is also computed with Monte Carlo normalized to data. In this case, the 98% of the same-B secondaries that are successfully cut are used to estimate the 2% that leak through, so the statistical uncertainty is very small. The quality of the fit (Sect. 4.7.2) in the two dimensions of opening angle vs. momentum shows that both the normalization (which we don't use) and the detailed distributions (which we do) are very well represented in Monte Carlo. We take a conservative 15% uncertainty in the same-B secondary leakage to account for possible errors in these details.

5.3 Non-Vetoed Background Corrections

Similar to the method of determining the systematic errors attached to veto leakage, we trust the Monte Carlo to simulate the shapes of the momentum spectra for these backgrounds. For each component we have attempted to assess a reasonable uncertainty based on world-average branching fractions and other information. In all cases we take as the systematic uncertainty one half of the difference between the variation

up and variation down.

Upper-vertex charm is the largest of these sources. It subdivides into final states that include a D_s-meson and another charmed particle and those that have two non-strange charmed mesons. We treat these independently, since their estimates are largely based on different experimental and theoretical inputs. While the semileptonic branching fraction $\mathcal{B}(D_s \to Xe\nu)$ is not well measured, the D^0 and D^+ semileptonic branching fractions can be combined with lifetime data to estimate $\mathcal{B}(D_s \to Xe\nu) \simeq 8\%$. This is consistent with the value in CLEO's standard `decay.dec`, and is probably reliable at the 10% level. This uncertainty is essentially negligible, however, compared to that in the branching fraction for $B \to D_s X$, which has been estimated to be $9.8 \pm 3.7\%$ [41] based on a variety of exclusive measurements. CLEO's default Monte Carlo is consistent with this number, and we take the overall systematic uncertainty on the contribution of semileptonic decays of upper-vertex D_s to be $\pm 40\%$.

The upper-vertex D contribution is somewhat better known, with well measured semileptonic branching fractions and an estimated rate for $B \to \bar{D}D^{(*)}X$ of $8.2 \pm 1.3\%$ [41]. We have determined that CLEO Monte Carlo agrees with these numbers and assign a systematic uncertainty on the electrons from upper-vertex non-strange charmed mesons of $\pm 25\%$.

The estimated contributions of $B \to \tau \to e$ and $B \to \psi' \to e^+e^-$ are both based on world-average measured branching fractions. Both are assigned systematic errors of $\pm 15\%$, taking into account the errors of those branching fractions, with some additional uncertainty associated with the shapes of the momentum spectra.

5.4 Fake Muon Tag Correction

Since muons are only used for tags, the correction for fake muons only enters our results through the normalization of our primary spectrum. We take an overall systematic uncertainty on the muon fakes of ±25%. As is discussed in Sect. 5.5, our preferred approach for determining the systematic uncertainty in our electron identification efficiency also incorporates the uncertainty in the associated fake correction.

5.5 Electron Identification Systematic Errors

The usual techniques for estimating the uncertainty in the electron-ID efficiency involve analyses of independent control samples: radiative Bhabha scatters ($e^+e^-\gamma$, both "raw" and "embedded" into hadronic events), π^0 Dalitz decays and conversions, and J/ψ decays. The statistics and momentum coverage of these are limited, and each carries its own systematic uncertainties. In CBX 95-35 [42], a variety of studies were described that led to the conclusion that the CEID efficiency measured with embedded radiative Bhabhas could be relied on to 3%, subject to the caveat that sufficient care be taken that the conditions of the efficiency measurement (track-quality criteria, event topologies, etc.) be compatible with the details of the signal selection. Since we measure all of our own efficiencies, we have satisfied this condition.

In the predecessor to this analysis [25, 26], the combined uncertainty due to tracking and CEID efficiency was estimated to be 2%, based on a careful comparison of efficiencies for embedded and unembedded radiative Bhabha electrons. This systematic uncertainty was 30% of the *inefficiency* of electron ID, and was judged to be

appropriately conservative. We feel very confident that the efficiency of our current package, TEID, is known at least to this 2% level, since it has been demonstrated to be immune to some of the problems that plague the efficiency determination for CEID in CLEO II and CLEO II.V data.

For past studies, most notably the first-generation lepton-tagged analysis [25, 26], the primary results were yields and branching fractions, which are sensitive only to the momentum-averaged efficiency. It was therefore unnecessary to scrutinize carefully the reliability of the measured momentum dependence of the EID efficiency. Our determination of the spectral moments of the electron energy spectrum is much more demanding in this regard. As has been described in Sect. 4.3, the incompletely understood momentum-dependent behavior of the radiative-Bhabha-measured CEID efficiency and the need to have an electron-ID efficiency with a reliably determined momentum-dependent efficiency were principal motivations for developing the TEID algorithm.

The event sample for determining the efficiency for TEID is identical to that used for CEID: radiative Bhabha events embedded into hadronic events, with reweighting to an approximately flat angular distribution (Sect. 4.5.2). Quantitatively assessing the systematic uncertainties in our observables (branching fraction, moments) remains a major challenge.

Our initial approach involved the application of "skewing" functions to the measured efficiencies, introducing distortions subject to the overall $\pm 2\%$ uncertainty. The philosophy is to explore "worst-case" scenarios, which can be visualized as a line with positive slope, a line with negative slope, a "Λ", and a"V". Skewing in this man-

ner needs to be done separately for each choice of minimum energy for the moment computations, so it is quite tedious.

For estimating the systematic uncertainty associated with the fake electron correction, our initial approach was to vary the total fake probability in three momentum ranges: $\pm 25\%$ for 0.6 - 1.0 GeV/c, $\pm 50\%$ for 1.0 - 1.8 GeV/c, and $\pm 100\%$ for 1.8 - 3.0 GeV/c. To calculate the uncertainty due to fakes for a given observable, all three ranges were varied up and down in the following combinations: up-up-up, down-down-down, up-none-down, down-none-up, up-down-down, and down-up-up. For each variation, the quantity is recalculated, and half of the biggest difference between the values from any two variations is taken as the error on that observable.

We find these procedures to be quite unsatisfying. They seem arbitrary and provide no quantitative basis for assessing a "one-sigma" systematic uncertainty. We have therefore explored alternative approaches. Despite their shortcomings, we keep the skewing results in mind as a benchmark for comparison with other estimates. As is discussed below, our preferred approach for determining the systematic uncertainty in our electron identification efficiency also incorporates the uncertainty in the associated fake rate.

One advantage of the TEID algorithm is that it is "factorizable" into its distinct components. We use the likelihood-based analysis of CEID only below 1.0 GeV, where the power of multiple experimental inputs helps to suppress difficult backgrounds from kaons and antiprotons, and where past studies have revealed no systematic problem in the determination of the efficiency. In the region above 1.0 GeV, TEID is SEID plus a high-side E/p cut, with a TF cut also applied below 1.6 GeV. The relative

simplicity of this procedure, especially above 1.0 GeV, led us to explore whether Monte Carlo could be used as a tool to transfer measured efficiency information from embedded radiative Bhabha events to signal events. Beginning with the E/p cut, we compared distributions for real and simulated radiative Bhabha events, both bare and embedded. The agreement was quite reasonable in both cases, within about 1% for unembedded radiative Bhabha electrons over the full energy range, and varying from about 2% near 1 GeV to less than 1% above 2 GeV for embedded radiative Bhabhas. This sounds pretty good, except that the signs of the two effects are opposite: MC is better (higher efficiency) than data for bare radiative Bhabhas and worse than data for the embedded. Our conclusion from this observation and the lack of real dE/dx simulation is that MC could never provide better than a 3% or 4% test of the TEID efficiency.

Our second attempt was inspired by the "knob-turning" studies that have been standard issue for a number of analyses using neutrino identification. It is conceptually easy to adjust the selection criteria of TEID and recompute the the total yield and spectral moments. The procedure is to rerun the *entire* analysis with the altered TEID cuts. This requires recalculating the fake rates from the tagged $\pi/K/p$ samples and the efficiencies from the embedded radiative Bhabha events.

There are four components of TEID that offer knobs to be turned: below 1 GeV, where TEID is just CEID, there is just the `R2ELEC` cut; above 1 GeV there are separate cuts on E/p, dE/dx, and time of flight (the last only for electron energies up to 1.6 GeV). We turn these four knobs one at a time and generate new final spectra equivalent, except for the altered cut, to our standard TEID spectrum. Since

the four different knobs represent independent components of the electron selection, we combine their systematic uncertainties in quadrature. Note that these knobs simultaneously probe the reliability of the efficiency and the fake probabilities, so the resulting systematic uncertainty covers both sources.

This leaves us with the question of how far to turn the knobs. Our TEID cut values were chosen either based on conventional usage (CEID/`R2ELEC` and SEID as originally defined) or based on our own "optimizations," where we attempted to choose cut values that were effective in rejecting fake backgrounds while remaining on the "plateau" of efficiency. Each cut separately has a well-defined inefficiency that is no more than a few percent. For the less powerful components of TEID (dE/dx and time of flight), we simply took our alternatives to be the cases where those component cuts were turned off. For the two other cases this was not practical, since CEID with no `R2ELEC` cut and SEID with no E/p cut are not effective electron ID's. For these we made the assumption that we could estimate the systematic uncertainty by comparing the values obtained for standard TEID with those obtained for alternative cuts that had double the standard inefficiencies.

Fig. 5.1 shows the spectra obtained with our alternative electron identification packages. The effects on the yields and moments are given in Chapters **??** and **??**. The alternative cases to standard TEID are "TEID-TF" (TEID with the time-of-flight cut eliminated); "TEID-DX" (TEID with the dE/dx cut eliminated; "TEID-EpLo" and "TEID-EpHi" (TEID with E/p cuts that are made twice as hard either by pushing up on the low side or pushing down on the high side of the E/p distribution; and "TEID-CEID-hard" (TEID with a cut on `R2ELEC` of 4.83, which doubles the

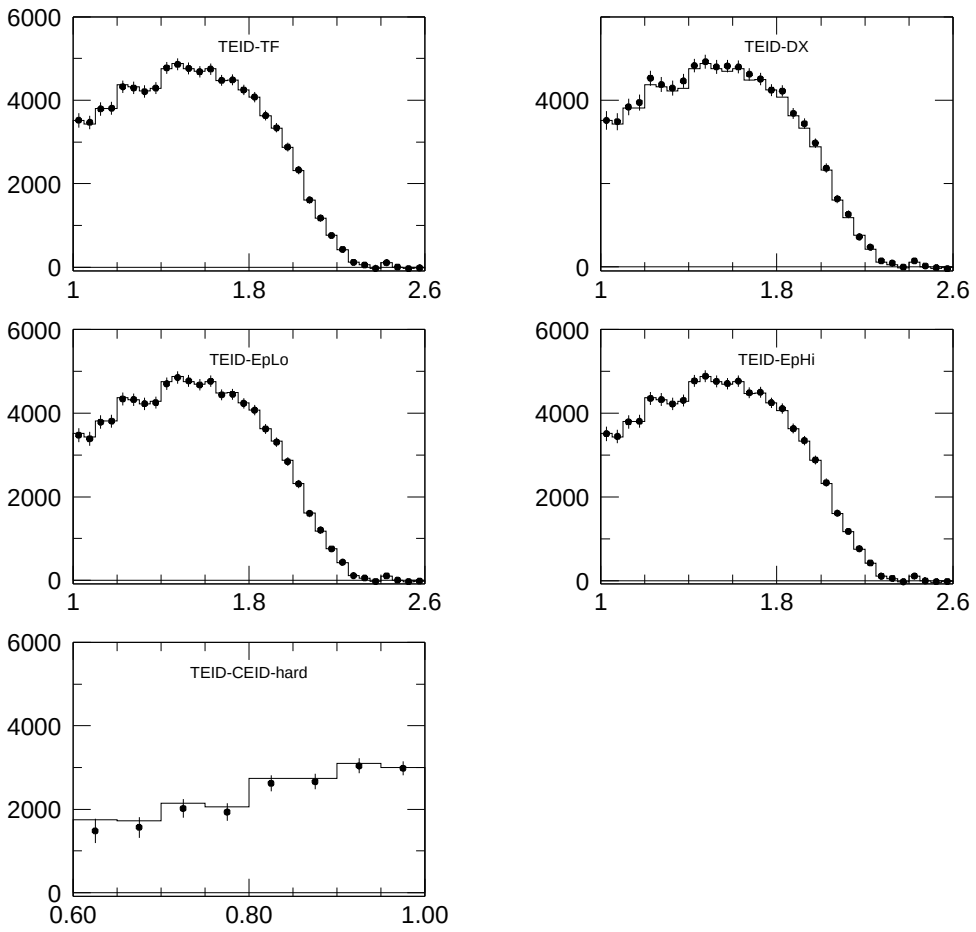

Figure 5.1: The final $b \to ce\nu$ momentum spectra with the alternative EID packages (points) overlaid with standard TEID spectrum (solid line). Note the limits on the momentum axes; only momentum ranges where the spectra differ are shown.

inefficiency between 0.6 and 1.0 GeV).

The efficiencies and fake rates corresponding to these cases are shown in Figs. 5.2 and 5.3. The agreement among the spectra is impressive. In particular, the stability in the shape of the low-momentum part of the electron spectrum under rather extreme variations is a very significant demonstration of the reliability of our efficiency and fake-rate determinations. In an earlier version of this study it was observed that the efficiency for "TEID-EpHi" showed a significant dip above 1.8 GeV. This was reminiscent of the "`PVRTX`" effect that plagues the measurement of the CEID efficiency with radiative Bhabhas. In fact, the merging of energy from the photon of a radiative Bhabha with the electron shower does affect the E/p cut. Our high-side cut value of 1.1 is quite loose, however, so this effect was believed to be small. We were surprised in our initial "TEID-EpHi" study because we mistakenly tightened the high-side E/p by much too large an increment. This distorted the efficiency and resulted in overestimates of the sensitivity of the observables to this cut. It was a good reminder, however, that pushing the cut up from the low side and down from the high side probe different aspects of the physics of electron identification. We therefore decided that they should both be used as independent contributions to the overall systematic uncertainty.

5.6 Tracking Efficiency

The systematic error from the efficiency of our track-quality cuts was estimated by taking the difference of the uncorrected spectrum and the spectrum corrected by the

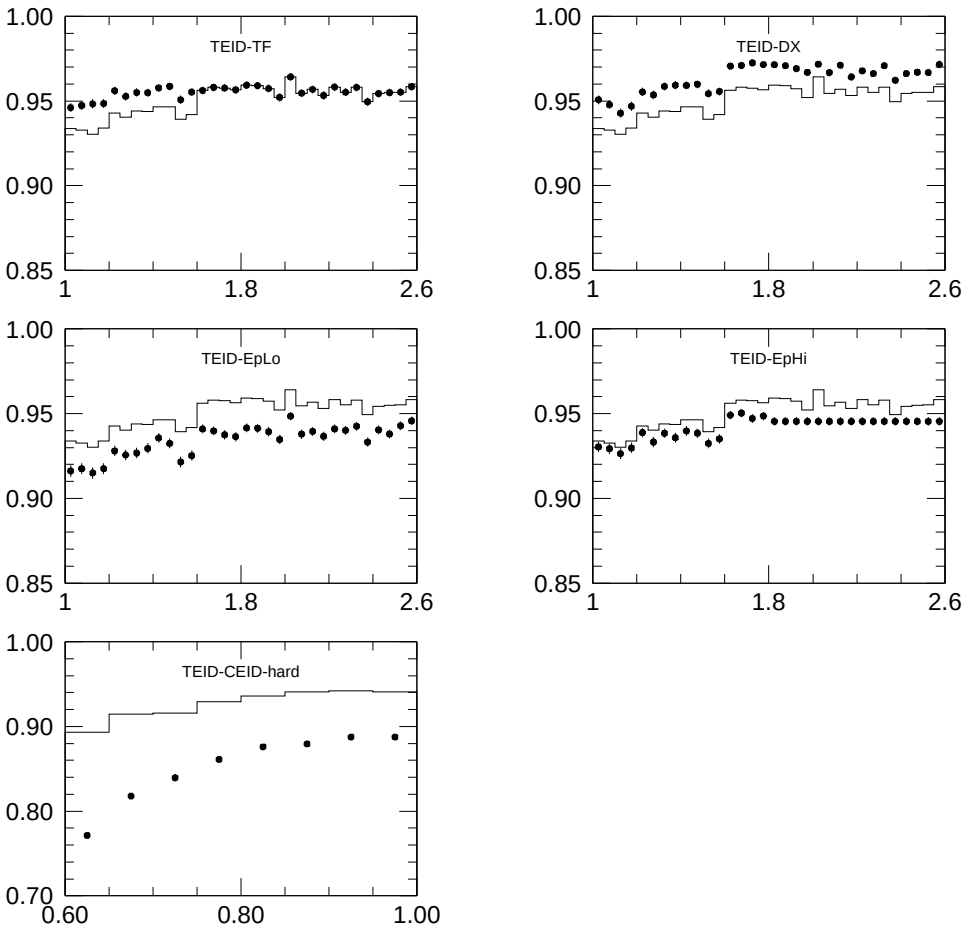

Figure 5.2: The efficiencies of the alternative EID packages (points) overlaid with standard TEID efficiency (solid line). Note the limits on the momentum axes; only momentum ranges where the efficiencies differ are shown.

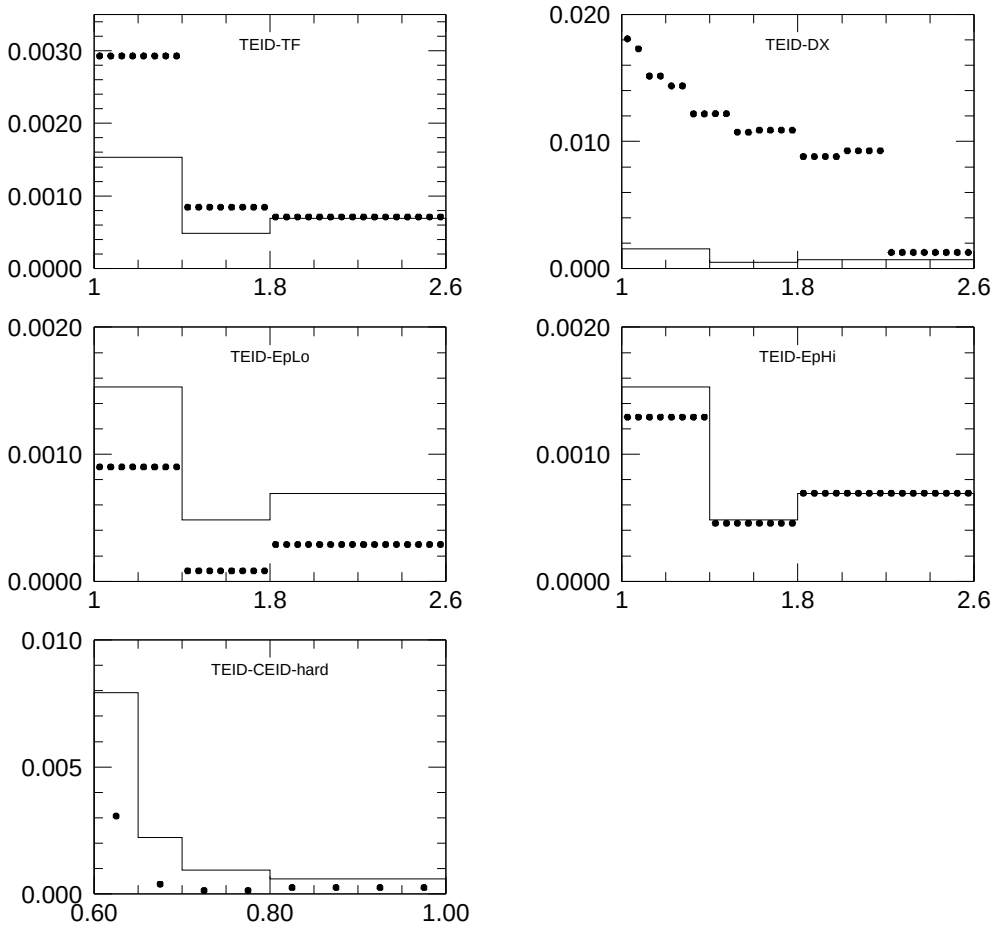

Figure 5.3: The total fake probabilities of the alternative EID packages (points) overlaid with standard TEID fake probability (solid line). Note the limits on the momentum axes; only momentum ranges where the fake probabilities differ are shown.

data/Monte Carlo ratio determined in the embedding study as described in Sect. 4.5.2.

5.7 Diagonal Cut Efficiency

We set the systematic uncertainty due to the efficiency of the diagonal cut based on extreme variations of the mixture of semileptonic B decays in our standard "BBLEP" Monte Carlo. No internal modifications, such as form factors governing the decays to D and D^*, or the models for the decays to D^{**} and nonresonant final states, were made. The approach was similar to that of the CLEO measurement of hadronic-mass moments [43], where the mixtures considered ranged from the "hardest possible" primary spectrum ($B \to D^* e\nu$ increased by 6%; $B \to D^{**} e\nu$ increased by 30%; $B \to De\nu$ decreased by 8%; nonresonant $B \to D^{(*)} X e\nu$ decreased by 30%) to the "softest possible" primary spectrum (reverse of the above variations). For each case we computed a new diagonal cut efficiency, rederived the final spectrum, and calculated new values for the observables. Half the difference between the two extremes was used as the systematic uncertainty associated with the diagonal cut efficiency.

5.8 Veto Efficiency

We calculate the systematic error due to the efficiency correction of the $J/\psi, \pi^0$, and γ-conversion by using the "hardest" and "softest" primary-spectrum variations described in Sect. 5.7. We then take as the error half the difference between the "hardest" and "softest" variations, plus 10% of itself. This extra 10% on the error

accounts for the fact that we only vary about 90% of the primary spectrum when we reweight the unlike-sign spectrum; the other 10% of the primary spectrum is in the like-sign spectrum (due to mixing).

One possible source of apprehension is the effect of the J/ψ veto in events with an unlike-sign electron tag; in these events, the tag electron is allowed to be the "second track" in the veto calculation of the signal electron, and vice versa. This gives us a lower and more momentum dependent efficiency than the other vetoes (Fig. 5.4). However, it is merely kinematics that gives rise to this momentum dependence; the

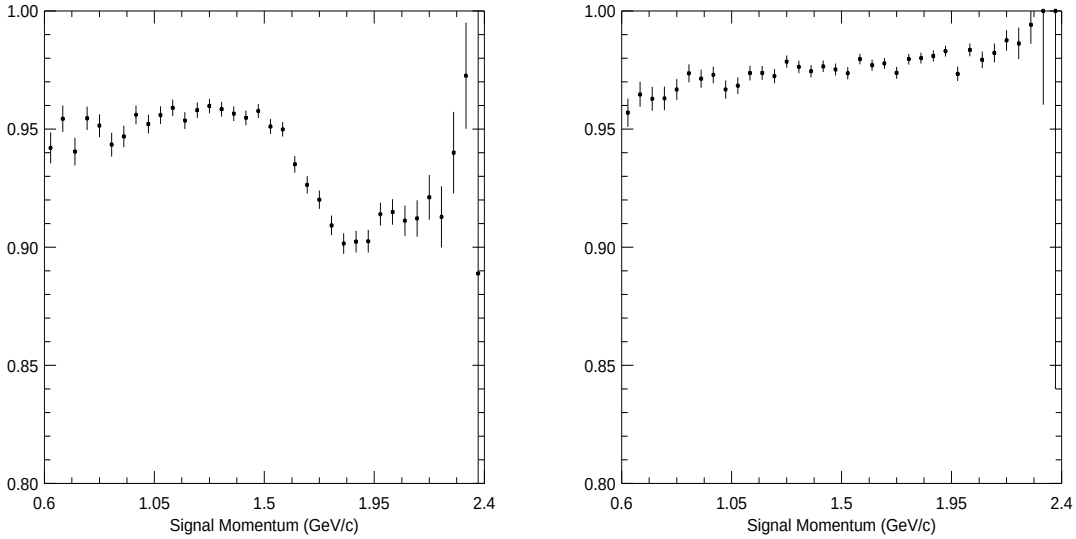

Figure 5.4: J/ψ veto efficiencies for unlike-sign events with electron (left) and muon (right) tags.

diagonal cut and the high-momentum tag requirement together limit the range of invariant masses a tag-signal pair can reach. The limit is dependent on the signal momentum, and as Fig. 5.5 shows, the Monte Carlo simulates the effect very well.

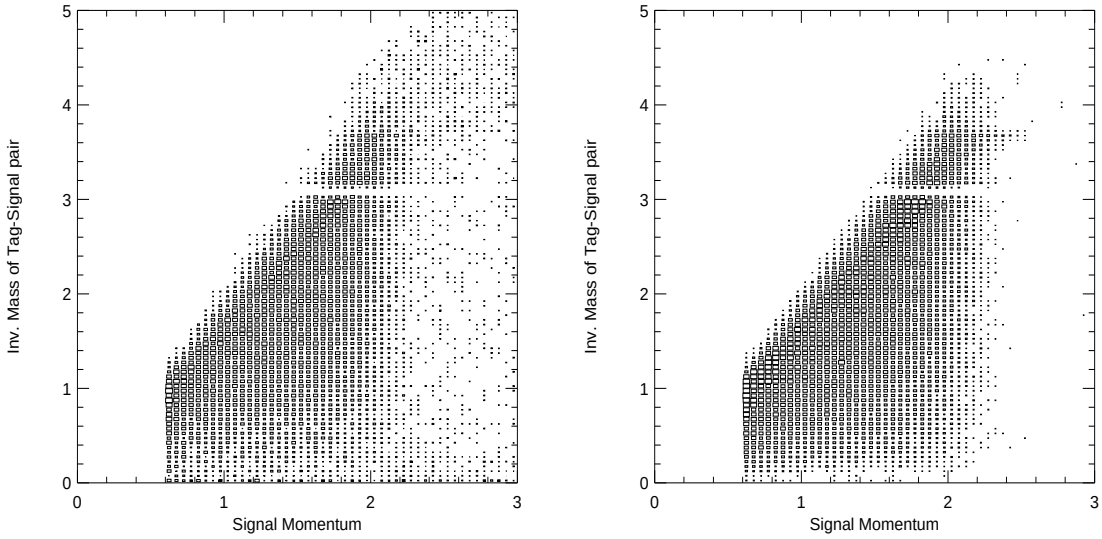

Figure 5.5: Invariant mass of tag and signal track pair vs. signal momentum in data (left) and Monte Carlo (right) for events with an unlike-sign electron tag. The diagonal cut is applied. The effect of the J/ψ veto is clearly seen, as is the range in signal momentum in which it appears.

Therefore, we make no special allowance for this effect in the determination of the systematic uncertainty associated with this efficiency.

5.9 $\Delta(p)$ and $B^0\bar{B}^0$ Mixing

For the systematic error on the factor $\Delta(p)$, we solve Eqs. 4.8 and 4.9 with $\Delta(p) = 1$, thereby taking the case that was standard before we recognized the need for $\Delta(p)$. We take half the difference between these cases as the systematic uncertainty.

The uncertainty on the mixing parameter χ was determined from relevant input data, as is described in Sect. 4.1.2. The effect on measured quantites was determined by solving for the spectra with values of χ that were shifted up and down by 1σ.

5.10 Summary of Sources of Systematic Uncertainty

The list below tabulates the sources of systematic uncertainty in the lepton-spectrum measurement and how each was quantified:

Corrections common to both measurements:

- J/ψ: $\pm 5\%$
- π^0: $\pm 20\%$
- γ: $\pm 20\%$
- Same B secondaries: $\pm 15\%$

- Upper vertex D_s: $\pm 40\%$
- Upper vertex D: $\pm 25\%$
- τ: $\pm 15\%$
- ψ': $\pm 15\%$
- Other backgrounds: $\pm 15\%$
- Tag from secondaries: $\pm 15\%$
- Muon tags from fakes: $\pm 25\%$ total muon fake subtraction
- EID: alternative EID packages ($\pm 2\%$ with skewing as backup)
- Continuum subtraction: $\alpha_{\mathcal{L}}$ scaled $\pm 1\%$.
- Non-EID efficiencies: hardest vs. softest primary spectrum
- $B^0\bar{B}^0$ mixing: $\chi = 0.089 \pm 0.004$
- $\Delta(p)$: half the difference with $\Delta(p) = 1$

In addition to these uncertainties, there were a number of others that exclusively affected the determination of the yield of leptons (branching fraction) or the shape of the momentum spectrum (moments). These are explained in more detail in the descriptions of the extraction of these quantities in the following sections.

Corrections specific to branching ratio measurement:

- Spectral fraction: Fits to the measured spectrum

- Relative event selection efficiency: Variations of the multiplicity distribution of signal MC

Corrections specific to the moments measurement:

- $b \to u$: $\pm 12\%$ magnitude of subtraction (based on the error in the lepton-energy endpoint measurement [34]. See Sect. 7.1.
- Electroweak radiative corrections: half the difference of Atwood/Marciano and PHOTOS, as described in Sect. 7.3
- B boost: $|\vec{p}_B|$ varied with reweighting by ± 10 MeV/c as described in Sect. 7.2.

CHAPTER 6

Results: Semileptonic Branching Ratio

In this chapter we describe the determination of the B semileptonic branching fraction $\mathcal{B}_{SL}$. By extracting the efficiency-corrected spectrum for semileptonic B decays in events with tags, we have done most of the work for the branching ratio measurement. The total area of the spectrum is the "primary count," which is the numerator of the branching fraction. It is $109,914 \pm 903$, where the error is statistical only.

The denominator of the branching ratio calculation is the "tag count," the *effective* number of tags in our data sample. Its determination is described in the next section.

6.1 Effective Number of Tags

The first step is simply to count the leptons in hadronic events in CLEO II and II.V data that pass the criteria for tag selection given in Sect. 4.3.5. After continuum subtraction, there is a total of $1,191,562 \pm 1,627$ raw lepton tags in our full data sample.

6.1.1 Corrections To Raw Tag Count

We must correct the raw tag count for backgrounds from processes other than semileptonic B decays. These represent the same sources and are computed by the same techniques as are described in Sect. 4.4.

The tag background corrections are tabulated in Table 6.1. After all subtractions, we obtain $N_\ell = 1,137,042 \pm 1,631$, where the error is statistical only. Systematic uncertainties associated with the background corrections are evaluated by the techniques of Sect. 5. They are included in the systematic uncertainties tabulated in Table 6.4.

6.1.2 Event Selection Efficiency Correction

Note that it is not necessary to correct the tag count for any of the efficiencies of lepton selection: track quality, lepton identification, etc. The reason for this is that the selection of events with tags provides us with a sample of $B\bar{B}$ events in which one B is known to have decayed semileptonically. It is the fraction of these events in which the other B decayed to an electron that gives us the semileptonic branching fraction. The only necessary corrections to the tag count are for effects that might cause us preferentially to gain or lose events in which that second B decayed semileptonically. We must therefore account for possible differences in the event-selection efficiencies for events with different numbers of leptons. We select hadronic events by CLEO's standard event classification, a very loose cut, and then suppress QED backgrounds with a fairly tight charged-multiplicity cut of at least five tracks that pass our track-

Source	μ	e	$\mu + e$
ON $\Upsilon(4S)$	828,155 ± 910	837,002 ± 915	1,665,157 ± 1,290
Scaled Continuum	261,667 ± 737	212,146 ± 664	473,813 ± 992
Cont. Subtracted	566,488 ± 1,171	624,856 ± 1,131	1,191,344 ± 1,628
Fake Leptons	11,385 ± 61	936 ± 4	12,321 ± 61
J/ψ	3,397 ± 28	4,451 ± 31	7,848 ± 42
π^0	N/A	190 ± 8	190 ± 8
γ	N/A	116 ± 6	116 ± 6
Secondary Charm	10,484 ± 47	13,347 ± 52	23,831 ± 70
Upper-Vertex D	330 ± 9	417 ± 9	747 ± 13
Upper-Vertex D_s	2,364 ± 22	818 ± 13	3,182 ± 26
τ	1,947 ± 20	2,538 ± 22	4,485 ± 30
ψ'	588 ± 11	609 ± 11	1,197 ± 16
Other Backgrounds	356 ± 9	29 ± 3	385 ± 9
Total	535,637 ± 1,174	601,405 ± 1,132	1,137,042 ± 1,631

Table 6.1: Yields and backgrounds for tag count. Errors are statistical only.

quality cuts, as described in Sect. 4.3.1.

We expect that a $B\bar{B}$ event with a lepton tag and a second semileptonic decay will tend to have lower multiplicity than an event with a tag and an accompanying B that decayed hadronically. (The mean multiplicity of hadronic B decays is greater than that of semileptonic decays.) We evaluate this effect with CLEO's generic $B\bar{B}$ Monte Carlo sample. The event-selection efficiency for any event with a lepton tag from semileptonic B decay is 95.8%, while that for events with a lepton tag **and** a second semileptonic B decay is 91.0%. The relative event selection efficiency is therefore 95.0%. This shows that our tag count is an overestimate of the number of events with tags that could enter into our primary count, and the effective number of tags is $N_\ell = 1,079,901 \pm 1,549$ (statistical error only).

This event-selection efficiency introduces systematic uncertainty into the branching fraction that depends on how well the Monte Carlo simulates the multiplicity of B decays in general, and semileptonic B decays in particular. We believe that `CLEOG` provides a good description of the response of the detector, and that the standard CLEO Monte Carlo represents the state-of-the-art understanding of B decay, but it is necessary to test these assumptions.

We compared the multiplicity distributions for CLEO Monte Carlo and data by binning our results (the yields of primary and tag leptons) in `NTRKGD`, the number of tracks that passed the track-quality cuts described in Sect. 4.3.1. The six bins we used for this study were `NTRKGD` = 5, 6, 7, 8, 9, and ≥ 10. Comparisons of the resulting distributions for $B\bar{B}$ data and Monte Carlo tags and primaries are shown in Fig. 6.1. For the primary signal events, the Monte Carlo reproduces very well the

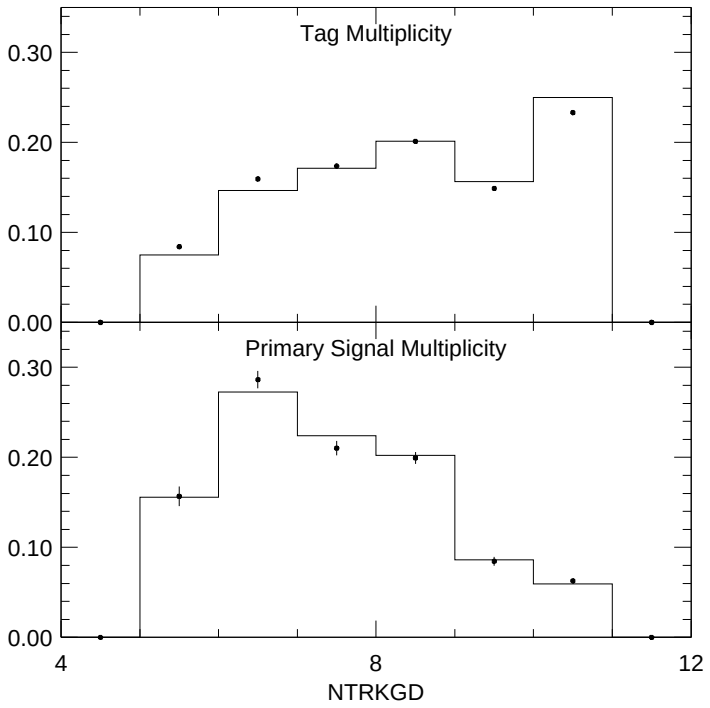

Figure 6.1: Multiplicity of good track-quality tracks in data (points) and Monte Carlo (histogram) for tag events (top) and primary signal events (bottom). The `NTRKGD`=10 bin in both plots is the sum of all events with `NTRKGD`$\geq$ 10.

average multiplicity (data average = 7.456, MC = 7.468). For tag events, there is a disagreement of about 0.1 unit (data = 8.370, MC = 8.468). Note that these average multiplicities are for the described binning scheme, and should not be interpreted as "true" multiplicities. The difference in the accuracy of the multiplicity modeling for hadronic and semileptonic decays is not surprising. Hadronic decays of B are less precisely modeled than semileptonic, because less of the total rate is in well-measured exclusive modes.

While we do not have enough confidence in this test to correct our results based on it, we take the difference between data and Monte Carlo as a reasonable indication of the systematic uncertainty in the determination of the relative event-selection efficiency. We estimated it by reweighting the Monte Carlo to get the tag-event multiplicity to agree with data. (The difference for primary events was judged to be too small to warrant such an exercise.)

For this study we went back to the parent samples of events with tags that had not been subjected to the `NTRKGD` cut. It was found by iteration that decrementing `NTRKGD` by one unit in 17% of the tag events (randomly chosen) brought the average `NTRKGD` in the Monte Carlo into agreement with the data (Fig. 6.2). The selection efficiency for tag events in this reweighted Monte Carlo sample is 94.6%, giving a relative event-selection efficiency of 96.1%. The difference between this and the central value given above is 1.2%, which we take as the systematic uncertainty.

We should also note here that there was a misconception in the previous version of this analysis. When calculating the relative event-selection efficiency, the signal electron in the numerator was **not** required to be a primary decay (i.e. $B \to X_c e \nu$).

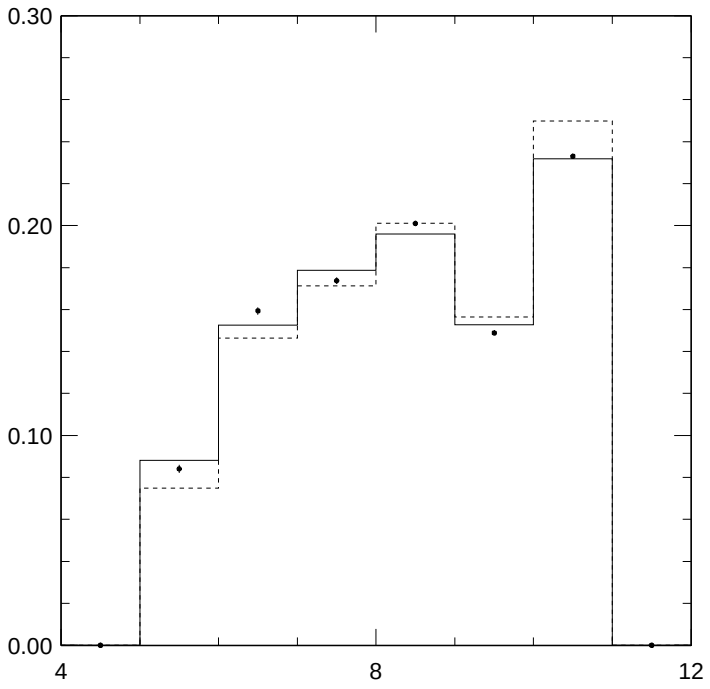

Figure 6.2: Multiplicity of good track-quality tracks in data (points), reweighted Monte Carlo (solid histogram), and standard Monte Carlo (dashed histogram) for tag events. The Monte Carlo has been reweighted as described in the text. The `NTRKGD`=10 bin in both plots is the sum of all events with `NTRKGD`$\geq$10.

Including all dilepton events in the numerator has the effect of raising the average charged multiplicity in those events, since it admits cases where an electron is produced further down the decay chain and is thus accompanied by more hadrons. When calculated in this incorrect way, the relative event-selection efficiency is overestimated and the branching ratio underestimated by a few percent.

6.2 Fraction Below 600 MeV/c

To determine the fraction of the primary spectrum below 600 MeV/c, we fit with a mixture of predicted spectra from Monte Carlo for the modes $B \to De\nu$, $B \to D^* e\nu$, $B \to D^{**} e\nu$, $B \to DXe\nu$, and charmless decays $B \to X_u e\nu$. All spectra were generated using a modified version of CLEO's generic $B\bar{B}$ Monte Carlo that included QED radiative corrections as described by the PHOTOS algorithm [30]. The decays $B \to D^* e\nu$ were generated with CLEO-measured form-factor parameters [44]. $B \to De\nu$ decays were generated with the ISGW2 [33] model, and then reweighted to correspond to HQET with the form factor ρ^2 as measured by CLEO [45]. These $B \to De\nu$ and $B \to D^* e\nu$ components of the fit are constrained to be within $\pm 2\sigma$ of the measured exclusive branching fractions [10]. The third fit component, denoted $B \to D^{**} e\nu$, is a mixture of higher-mass charmed mesons, as described by ISGW2 [33]. The fourth component is nonresonant $B \to DXe\nu$, as described by the model of Goity and Roberts [46]. These last two are constrained in the fit only to the extent that they are not allowed to go negative. The final component is $B \to X_u e\nu$ decays modeled with the INCLGEN generator [31]. The normalization of the $B \to X_u e\nu$ component

was fixed by the partial branching fraction in the 2.2-2.6 GeV/c momentum region measured in CLEO's 2002 end-point analysis [34].

The standard (STD) fit performed according to these specifications is shown in Fig. 6.3. The quality of the fit is quite good (χ^2=33.8/36 d.o.f), although we note that the $B \to De\nu$ and $B \to D^* e\nu$ branching fractions are pinned at their $\pm 2\sigma$ limits. With this fit, we determine that 93.6% of the total $B \to Xe\nu$ spectrum has $p_e \geq 600$ MeV/c.

We assess the systematic uncertainty associated with the correction for the spectral fraction by performing a large number of variations of the STD fit. In each case we refit with only one ingredient changed. The difference between the STD value for the spectral fraction and that for the modified fit is recorded as the systematic uncertainty associated with that ingredient. These results are tabulated in Table 6.2.

For $B \to De\nu$, we reweighted our standard ISGW2 Monte Carlo sample in q^2 and lepton momentum to get the HQET spectra with the values of ρ^2 increased and decreased by 1σ. These variations were designated DRHOUP and DRHODN.

For $B \to D^* e\nu$, we generated new spectra with `QQ` using altered values of the three form-factor parameters, consistent with CLEO's measurements. Alternative spectra were generated for six sets of parameters: $(R1 \pm 1\sigma, R2, \rho^2)$, $(R1, R2 \pm 1\sigma, \rho^2)$, and $(R1, R2, \rho^2 \pm 1\sigma)$, labeled as DSTR1UP(DN), DSTR2UP(DN), and DSTRHOUP(DN), respectively. Correlations among the form-factor measurements were taken into account in estimating the associated systematic uncertainties in the spectral fraction.

We also consider extreme variations in the less well known D^{**} and nonresonant components. For the HIDDUB and LODDUB fits, we fixed the normalization of the

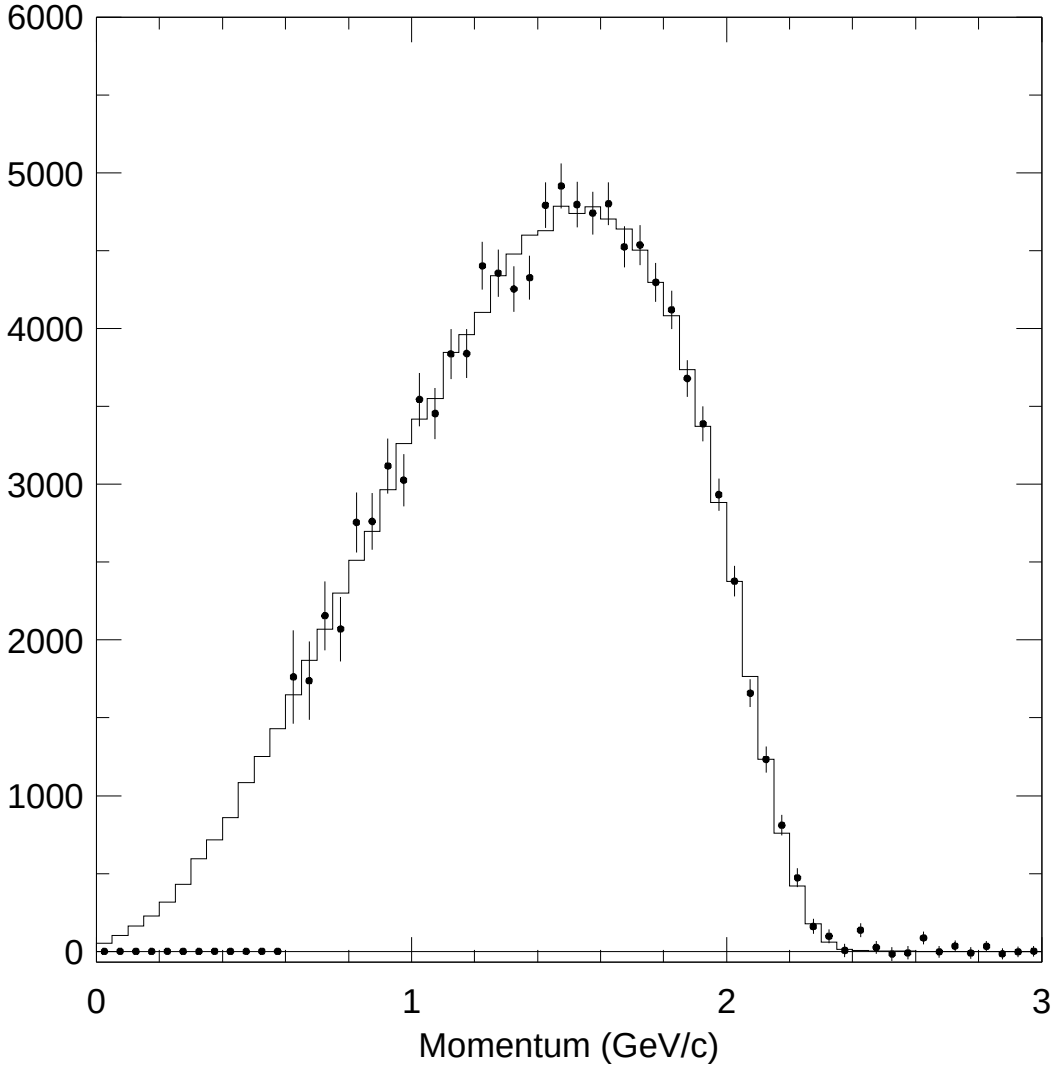

Figure 6.3: Results of fitting the final $B \to Xe\nu$ spectrum.

D^{**} component to be $\pm 1\sigma$ above and below the value preferred by the STD fits. This corresponds to an 89% shift in the D^{**} rate. The HINR and LONR fits are similarily done for the nonresonant component, corresponding to a 67% shift in the nonresonant rate. We use half the difference between the HIDDUB and LODDUB (HINR and LONR) fits as estimates for the systematic error due to uncertainty in the modeling of the D^{**} (DX) component.

We also consider variations in the amount of the fixed $B \to X_u e\nu$ in the fits. We vary the normalization by $\pm 1\sigma$, using the overall uncertainty in the 2002 result. These cases are designated as B2UHI and B2ULO. We take as the systematic error the bigger difference from STD of these two variations.

To assess the uncertainty in the QED radiative corrections to the spectral fraction, we do the NOFSR fit, using spectra generated without PHOTOS. This is clearly an extreme variation, so we use one-third of the resulting variation in the lepton yield as an estimate of the QED-related systematic error. (This is the approximate difference between PHOTOS and Atwood/Marciano.)

We also allow for a conservative ($\sim$ 10 MeV/c) variation in the scale of the B momentum used for the boost with the BPUP and BPDN fits [29]. We take half the difference between BPUP and BPDN as the systematic error related to the B boost.

There was one additional variation on $B \to De\nu$ and $B \to D^* e\nu$, which we included in response to concerns that the range of cases considered was not sufficiently broad. In the fit labelled "PDG," we locked the $B \to De\nu$ and $B \to D^* e\nu$ to their measured branching fractions, also using measured central values for their respective form-factor parameters. This gives a very poor fit to the spectrum (χ^2=87.2/38 d.o.f),

and has by far the largest effect on the spectral fraction of any case considered. It will be seen later, however, that this still does not make it a significant contributor to the overall systematic uncertainty.

To compute the total systematic error for the spectral fraction below 600 MeV/c, we take the quadrature sum of all of the variations considered. These results are summarized in Table 6.3.

6.3 The Branching Ratio

With the yield from the primary spectrum with $p_e \geq 600$ MeV/c and the effective tag count given in the preceding sections, we obtain the partial branching ratio:

$$\mathcal{B}_{SL}(p_e > 0.6 \text{ GeV}/c) = (10.21 \pm 0.08 \text{ (stat.)} \pm 0.22 \text{ (syst.)})\% \tag{6.1}$$

Correcting for the fraction below 600 MeV/c, we determine the total B semileptonic branching ratio to be

$$\mathcal{B}_{SL} = (10.91 \pm 0.09 \text{ (stat.)} \pm 0.24 \text{ (syst.)})\%. \tag{6.2}$$

A breakdown of the systematic error on the total semileptonic branching fraction is given in Table 6.4. Note that the contributions to the systematic uncertainty for the background corrections are not separately determined for primaries and tags. When assumptions are varied, the effects on both numerator and denominator are propagated through to the branching fraction, thereby properly accounting for correlations. Table 6.4 also includes estimated systematic uncertainties in the final steps

	$\mathcal{B}_{SL}$	Frac.	χ^2	$\mathcal{B}(D)$	$\mathcal{B}(D^*)$	$\mathcal{B}(D^{**})$	$\mathcal{B}(NR)$	$\mathcal{B}(b \to u)$	$\Delta\mathcal{B}_{SL}$
STD	10.868	0.936	33.8/38	*2.43	*5.82	2.00	0.41	*0.177	–
BPUP	10.878	0.935	31.8/36	1.72	6.51	1.13	1.36	*0.177	0.010
BPDN	10.866	0.936	32.6/36	2.23	6.26	0.87	1.27	*0.177	-0.002
DDSTFIX	10.863	0.937	32.0/37	2.61	6.06	0.94	1.08	*0.177	-0.005
DDSTUP	10.859	0.937	32.1/37	2.84	5.94	0.91	1.00	*0.177	-0.009
DDSTDN	10.867	0.936	31.9/37	2.36	6.19	0.97	1.17	*0.177	-0.001
DSTR1UP	10.870	0.936	31.7/36	3.07	5.37	1.64	0.63	*0.177	0.002
DSTR1DN	10.857	0.937	28.8/36	0.26	8.35	0.00	2.07	*0.177	-0.01
DSTR2UP	10.875	0.936	30.1/36	2.28	5.98	1.10	1.36	*0.177	0.007
DSTR2DN	10.868	0.936	30.6/36	0.73	7.80	0.53	1.63	*0.177	0.000
DSTRHOUP	10.867	0.936	28.2/36	1.24	7.02	0.00	2.43	*0.177	-0.001
DSTRHODN	10.876	0.935	30.7/36	1.66	6.63	1.87	0.55	*0.177	0.008
DRHOUP	10.867	0.936	31.9/36	2.06	6.38	0.81	1.45	*0.177	-0.001
DRHODN	10.874	0.936	32.3/46	2.05	6.35	1.12	1.19	*0.177	0.006
B2UFLT	10.863	0.937	31.5/35	2.59	6.20	0.66	1.28	0.13	-0.005
B2UHI	10.859	0.937	33.3/35	1.61	6.45	1.39	1.23	*0.225	-0.009
B2ULO	10.862	0.937	31.5/35	2.60	6.20	0.65	1.28	*0.129	-0.006
NOFSR	10.842	0.938	32.6/36	1.84	6.41	1.58	0.82	*0.177	-0.026
OLD STD	10.871	0.936	31.9/36	2.11	6.32	1.02	1.26	*0.177	0.003
LODDUB	10.864	0.937	32.9/37	2.69	6.22	*0.16	0.016	*0.177	-0.004
HIDDUB	10.878	0.935	32.9/37	1.50	6.43	*1.96	0.857	*0.177	0.010
LONR	10.847	0.938	32.9/37	3.31	5.55	1.42	*0.37	*0.177	-0.021
HINR	10.895	0.934	32.9/37	0.91	7.09	0.61	*2.14	*0.177	0.027
PDG	10.940	0.930	87.2/38	*2.13	*4.95	3.64	0.00	*0.177	0.072
Total									0.078

Table 6.2: Results for $b \to c\ell\nu$ fits to determine systematic error due to estimate of measured spectral fraction. Explanations of the fit labels in the first row are given in the text. Entries denoted with a "*" have been fixed for that fit. Values for branching ratios are in percent.

Source	$\Delta\mathcal{B}_{SL}(\%)$
$\langle p_B \rangle$	0.003
D^* FF's	0.010
$D\rho^2$	-0.003
$b \to u$	-0.009
No final state rad.	-0.009
D^{**} BR	-0.007
Non-res. BR	-0.024
PDG BR's	0.072
Total	0.078

Table 6.3: Systematic errors on the spectral fraction below 600 MeV from the fitting study.

of disentangling the spectra and in computing the semileptonic branching fraction, which have all been described.

Source	$\Delta\mathcal{B}_{SL}(\%)$
J/ψ	0.003
π^0	0.006
γ	0.023
Same B secondaries	0.052
Upper Vertex D_s	0.091
Upper Vertex D	0.065
τ	0.041
$\psi(2S)$	0.005
Other Backgrounds	0.003
Tags from Secondaries	0.014
Electron Identification	0.113
Mixing Parameter	0.035
Continuum Subtraction	0.028
Track Quality Efficiency	0.001
Diagonal Cut Efficiency	0.008
Veto Efficiency	0.006
Muon Fake Rate	0.001
$\Delta(p)$	0.021
Event Selection Ratio	0.128
Fit Extrapolation	0.078
Total	0.236

$\Longrightarrow$

EID Source	$\Delta\mathcal{B}_{SL}(\%)$
TEID-TOF	0.002
TEID-dE/dx	0.064
$E/p \geq 0.91$	0.047
$E/p \leq 1.07$	0.055
CEID-HARD	0.042
Total	0.105

Table 6.4: **Left:** Breakdown of systematic errors on $\mathcal{B}_{SL}$. **Right:** Details of electron identification systematic error on $\mathcal{B}_{SL}$.

CHAPTER 7

Results: Lepton Energy Moments

Following the notation of Bauer *et al.* [11], the general expression for the moments is defined as follows:

$$R[n, E_{\ell_1}, m, E_{\ell_2}] = \frac{\int_{E_{\ell_1}}^{E_{max}} E_\ell^n \frac{d\Gamma}{dE_\ell} dE_\ell}{\int_{E_{\ell_2}}^{E_{max}} E_\ell^m \frac{d\Gamma}{dE_\ell} dE_\ell} \tag{7.1}$$

where $E_\ell^{max} = 2.5$ GeV. For convenience, we will denote $R[1, E_{min}, 0, E_{min}]$ and $R[2, E_{min}, 0, E_{min}]$, as $\langle E_\ell \rangle$ and $\langle E_\ell^2 \rangle$, with E_{min} as a subscript when necessary. We will use the variance of the spectrum $\langle (E_\ell - \langle E_\ell \rangle)^2 \rangle$ as an alternative second moment, as it is less strongly correlated with $\langle E_\ell \rangle$ than $\langle E_\ell^2 \rangle$. We also report results for the third moment (or "skew") $\langle (E_\ell - \langle E_\ell \rangle)^3 \rangle$.

We have chosen to compute the moments of the electron-energy spectrum by direct integration of our final spectrum (Fig. 7.2). Obtained in this way, the experimental moments are not precisely equivalent to the theoretical computations of moments given in the literature. Because our moments are measured in the $\Upsilon(4S)$ rest frame, so we must correct for the boost of the spectrum from the B rest frame, where theoretical predictions are calculated. Our moments also show the effect of final-state radiation, which is not by default included in the theoretical results, so we must use calculations of electroweak radiative corrections to correct our moments for this effect. The techniques for determining these corrections are described in the next sections.

7.1 $B \to X_u e\nu$ Correction

One last background subtraction needs to be made before we can get moments: the subtraction of the electrons from $B \to X_u e\nu$ decays. To get this spectrum, we use the Monte Carlo sample generated with the hybrid inclusive/exclusive model `INCLGEN` (see Sec. 4.2.1). The scale for the subtraction was set by normalizing the `INCLGEN` spectrum to CLEO's measured partial branching fraction [29, 34] in the best-measured region of 2.2-2.6 GeV/c. The resulting $B \to X_u e\nu$ spectrum (Fig. 7.1) is subtracted from the primary spectrum (Fig. 4.21) to produce the final $B \to X_c e\nu$ spectrum in Fig. 7.2, which is ready for the computation of the moments.

To assess systematic uncertainties associated with the $B \to X_u e\nu$ correction, we vary the normalization by $\pm 1\sigma$, as determined by the total error on the partial branching fraction in the 2.2-2.6 GeV/c region [29, 34]. This corresponds to a $\pm 12\%$ variation of the $B \to X_u e\nu$ correction. We have also considered alternative $B \to X_u e\nu$ spectra based on reweighting the exclusive and inclusive components of the `INCLGEN` sample to increase and decrease the portion of the 2.2-2.6 GeV/c yield allocated to $B \to (\pi/\rho/\eta/\omega)e\nu$. By using the measured branching ratios of these exclusive modes [47] in the 2.2-2.6 GeV endpoint region and spectral fractions determined by the average of several models, the fraction of the endpoint region due to these modes was estimated to be approximately 0.55 with an error of about 30%. `INCLGEN` quite remarkably delivers this fraction as 0.58. The alternative $B \to X_u e\nu$ shapes are shown in Fig. 7.1. We take as the systematic error half the difference between the upward and downward variations.

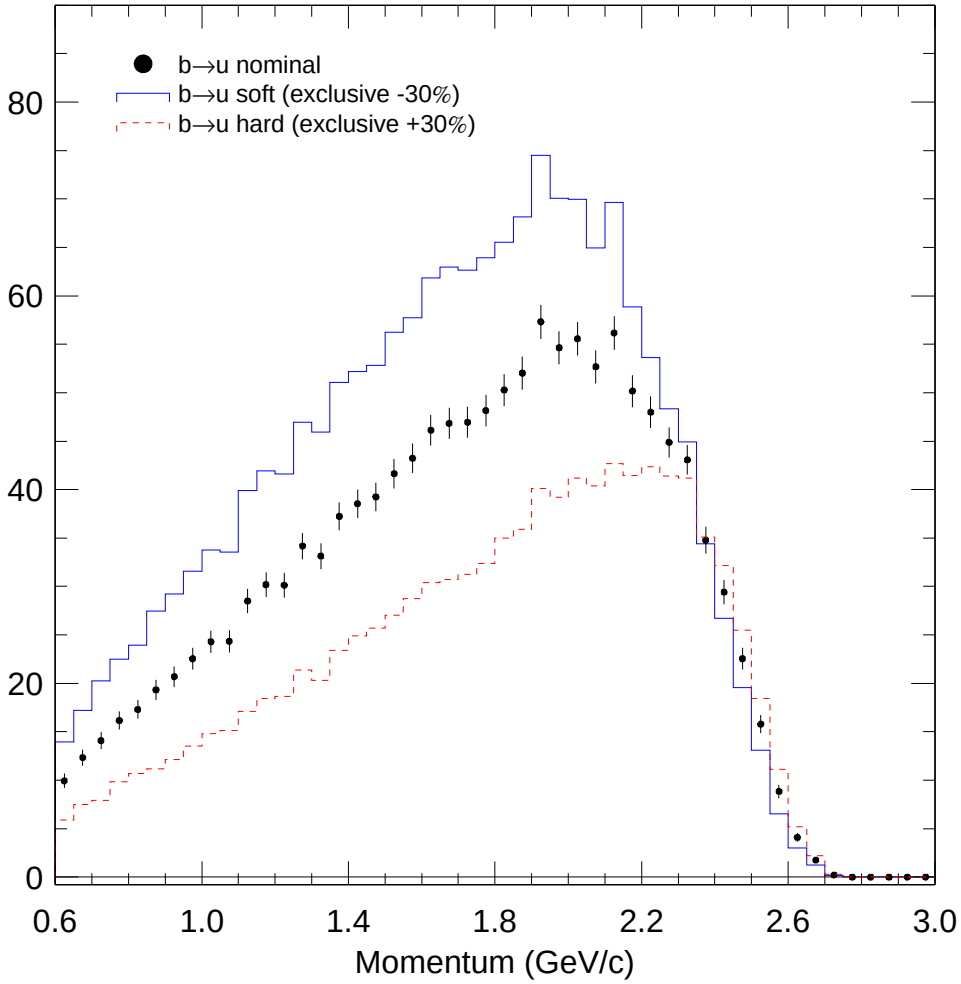

Figure 7.1: Spectrum of electrons from $B \rightarrow X_u e\nu$ decays from the `INCLGEN` Monte Carlo sample reweighted to enhance(red dashed)/degrade(blue solid) the $B \rightarrow \pi/\rho/\eta/\omega e\nu$ portion of the 2.2-2.6 GeV endpoint region by 30%.

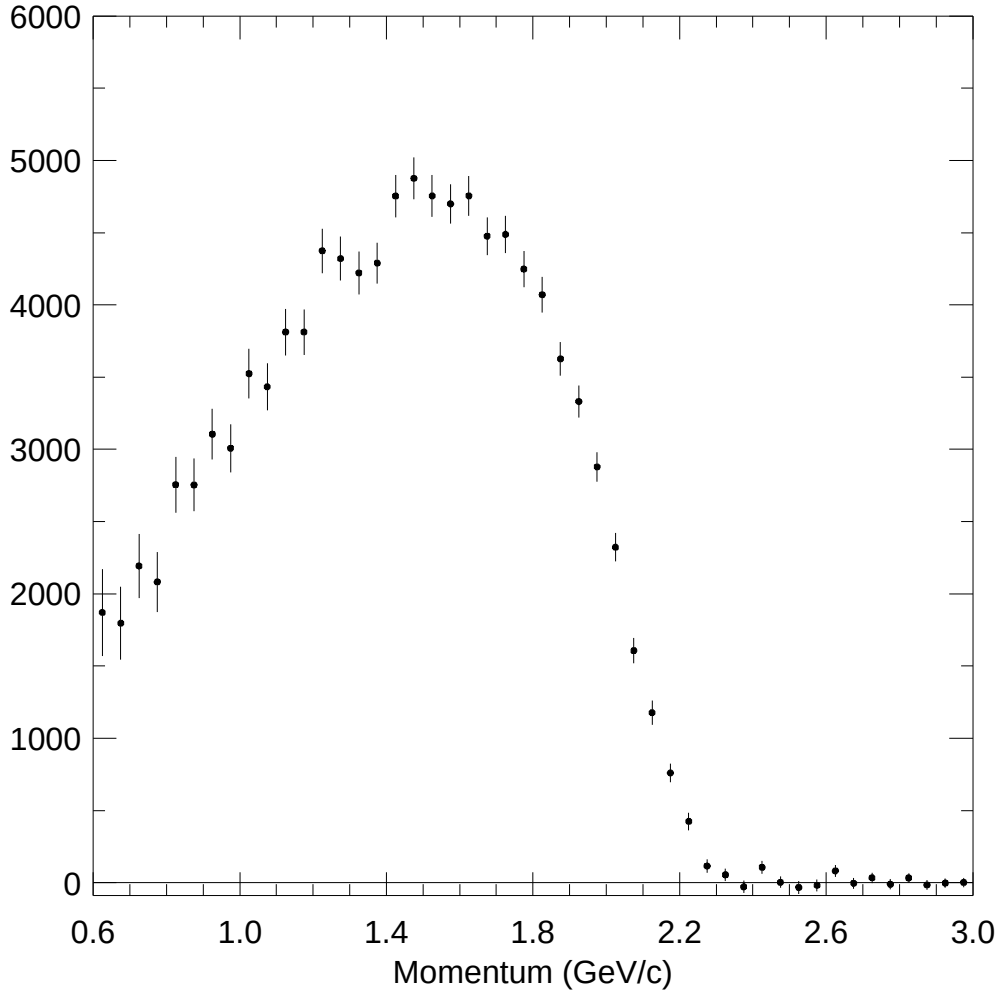

Figure 7.2: The final $B \to X_c \ell \nu$ spectrum.

7.2 Boost Correction

The B mesons produced at the $\Upsilon(4S)$ are not exactly at rest; they typically have momenta of approximately 300 MeV/c. Using Monte Carlo, we obtain an additive correction to a moment by comparing the value of the moment obtained from a QQ spectrum of primary electrons in the lab frame with the value obtained from a spectrum of the same electrons in which each electron's momentum is boosted back to its parent B's rest frame. The difference of these two values is taken as the correction. Since we use a Monte Carlo sample corresponding to the entire CLEO II and CLEO II.V data set, we are guaranteed to get the appropriate distribution of nominal beam energies.

The systematic error associated with boosting the spectrum back to the B-rest frame is obtained by reweighting the QQ sample to achieve a ± 10 MeV/c shift in the mean B momentum. The moment is then calculated with the spectrum from these reweighted samples, and half the difference from the +10 and -10 MeV/c shifted samples is the taken as the systematic error.

7.3 Electroweak Correction

We obtain an additive correction for QED final-state radiation using the PHOTOS algorithm [30] implemented in QQ. We generated spectra of primary electrons with and without final-state radiation, and calculated the moments for both spectra with EW radiation on and off. The difference between these is taken as the correction. For comparison and assessment of the systematic error associated with this correction,

we also used Atwood and Marciano [48].

The systematic error for the electroweak correction was obtained by comparing the value of the correction from Atwood and Marciano with that calculated using PHOTOS to model the final-state radiation. The difference between the corrections from the two models is taken as the systematic uncertainty.

7.4 Moments

From our final spectrum, we extract values for moments with $E_\ell \geq 600$ MeV:

$$\langle E_\ell \rangle_{0.6} = (1.4261 \pm 0.0043 \text{ (stat.)} \pm 0.0105 \text{ (syst.)}) \text{ GeV}$$

$$\langle (E_\ell - \langle E_\ell \rangle)^2 \rangle_{0.6} = (0.1526 \pm 0.0021 \text{ (stat.)} \pm 0.0031 \text{ (syst.)}) \text{ GeV}^2$$

Systematic uncertainties in the moment values have been assessed with the techniques described in Chap. 5 (background and efficiency corrections) and earlier in this section (moment extraction). The systematic uncertainties for $\langle E_\ell \rangle$, $\langle E_\ell^2 \rangle$, $\langle (E_\ell - \langle E_\ell \rangle)^2 \rangle$, and $\langle (E_\ell - \langle E_\ell \rangle)^3 \rangle$ are summarized for all of our choices of minimum lepton energy in Tables 7.1, 7.2, 7.3, and 7.4, respectively.

7.4.1 Errors and Correlations on the Moments

The calculations of the errors on each moment are relatively straightforward: each source of systematic error is assumed to be independent of all the others, and therefore they are all added in quadrature to determine the total systematic error. The

E_ℓ cut (GeV) $\rightarrow$	**0.6**	**0.7**	**0.8**	**0.9**	**1.0**	**1.1**	**1.2**	**1.3**	**1.4**	**1.5**
Uncorr. Moment	1.4118	1.4384	1.4676	1.5032	1.5411	1.5827	1.6268	1.6765	1.7248	1.7800
Boost Corr.	-0.0025	-0.0024	-0.0029	-0.0028	-0.0030	-0.0033	-0.0034	-0.0039	-0.0047	-0.0051
A&M Corr.	0.0108	0.0099	0.0090	0.0081	0.0072	0.0064	0.0056	0.0048	0.0041	0.0034
PHOTOS Corr.	0.0168	0.0149	0.0132	0.0115	0.0102	0.0090	0.0080	0.0068	0.0055	0.0043
Continuum Sub.	0.0004	0.0001	0.0000	0.0001	0.0001	0.0001	0.0002	0.0002	0.0002	0.0002
J/ψ	0.0001	0.0001	0.0001	0.0001	0.0001	0.0001	0.0000	0.0000	0.0000	0.0000
π^0	0.0003	0.0002	0.0001	0.0001	0.0000	0.0000	0.0000	0.0000	0.0000	0.0000
γ	0.0013	0.0007	0.0004	0.0002	0.0001	0.0001	0.0000	0.0000	0.0000	0.0000
Same B Sec.	0.0029	0.0014	0.0006	0.0003	0.0001	0.0000	0.0000	0.0000	0.0001	0.0001
Upper Vertex D_s	0.0047	0.0031	0.0021	0.0013	0.0008	0.0005	0.0003	0.0002	0.0001	0.0001
Upper Vertex D	0.0036	0.0022	0.0013	0.0008	0.0004	0.0002	0.0001	0.0001	0.0000	0.0000
τ	0.0018	0.0014	0.0010	0.0007	0.0005	0.0003	0.0002	0.0001	0.0001	0.0001
$\psi(2S)$	0.0004	0.0004	0.0004	0.0004	0.0004	0.0004	0.0004	0.0004	0.0004	0.0004
Other Bckg	0.0001	0.0000	0.0000	0.0000	0.0000	0.0000	0.0000	0.0000	0.0000	0.0000
Secondary Tags	0.0002	0.0000	0.0001	0.0002	0.0003	0.0003	0.0003	0.0003	0.0003	0.0003
$\mathcal{B}(b \rightarrow ue\nu)$	0.0004	0.0004	0.0004	0.0004	0.0004	0.0004	0.0004	0.0004	0.0004	0.0005
$b \rightarrow ue\nu$ Shape	0.0004	0.0004	0.0004	0.0003	0.0003	0.0003	0.0003	0.0003	0.0003	0.0003
EID	0.0046	0.0040	0.0033	0.0026	0.0021	0.0017	0.0017	0.0019	0.0025	0.0024
Fake μ Tags	0.0002	0.0001	0.0001	0.0000	0.0000	0.0000	0.0000	0.0000	0.0000	0.0000
Track Quality Eff.	0.0001	0.0000	0.0000	0.0000	0.0000	0.0000	0.0000	0.0000	0.0000	0.0000
Diagonal Cut Eff.	0.0003	0.0003	0.0002	0.0003	0.0001	0.0001	0.0001	0.0001	0.0001	0.0000
Veto Eff.	0.0002	0.0001	0.0001	0.0001	0.0001	0.0001	0.0000	0.0000	0.0001	0.0000
B Boost	0.0005	0.0004	0.0003	0.0003	0.0006	0.0003	0.0003	0.0005	0.0005	0.0003
Electroweak Rad.	0.0060	0.0050	0.0042	0.0033	0.0030	0.0026	0.0025	0.0020	0.0014	0.0009
B^0 Mixing χ	0.0010	0.0007	0.0004	0.0003	0.0002	0.0001	0.0001	0.0001	0.0000	0.0000
$\Delta(p)$	0.0010	0.0007	0.0004	0.0003	0.0002	0.0001	0.0001	0.0001	0.0000	0.0000
Corrected Moment	1.4261	1.4509	1.4779	1.5119	1.5483	1.5884	1.6315	1.6794	1.7256	1.7792
Statistical Error	0.0043	0.0035	0.0031	0.0028	0.0026	0.0024	0.0023	0.0022	0.0021	0.0021
Systematic Error	0.0105	0.0079	0.0061	0.0047	0.0039	0.0033	0.0031	0.0029	0.0030	0.0027
Total Error	0.0113	0.0086	0.0068	0.0054	0.0047	0.0041	0.0039	0.0037	0.0037	0.0035

Table 7.1: Breakdown of corrections and errors on $\langle E_\ell \rangle$ at various lower lepton energy cuts. All numbers are in GeV.

E_ℓ cut (GeV) $\rightarrow$	**0.6**	**0.7**	**0.8**	**0.9**	**1.0**	**1.1**	**1.2**	**1.3**	**1.4**	**1.5**
Uncorr. Moment	2.1484	2.2086	2.2783	2.3681	2.4685	2.5839	2.7126	2.8641	3.0181	3.2019
Boost Corr.	-0.0095	-0.0096	-0.0110	-0.0109	-0.0118	-0.0129	-0.0135	-0.0155	-0.0183	-0.0203
A&M Corr.	0.0308	0.0290	0.0271	0.0251	0.0230	0.0209	0.0187	0.0166	0.0146	0.0125
PHOTOS Corr.	0.0467	0.0429	0.0392	0.0352	0.0323	0.0293	0.0268	0.0234	0.0195	0.0157
Continuum Sub.	0.0007	0.0002	0.0001	0.0003	0.0004	0.0005	0.0006	0.0007	0.0007	0.0008
J/ψ	0.0001	0.0001	0.0002	0.0002	0.0002	0.0001	0.0001	0.0001	0.0000	0.0000
π^0	0.0008	0.0004	0.0003	0.0002	0.0001	0.0001	0.0001	0.0000	0.0000	0.0000
γ	0.0030	0.0017	0.0010	0.0005	0.0003	0.0002	0.0001	0.0000	0.0000	0.0000
Same B Sec.	0.0068	0.0034	0.0015	0.0007	0.0002	0.0000	0.0001	0.0001	0.0002	0.0002
Upper Vertex D_s	0.0117	0.0081	0.0056	0.0038	0.0025	0.0016	0.0010	0.0006	0.0004	0.0003
Upper Vertex D	0.0089	0.0057	0.0035	0.0022	0.0012	0.0007	0.0004	0.0002	0.0001	0.0001
τ	0.0046	0.0036	0.0027	0.0020	0.0014	0.0010	0.0007	0.0005	0.0003	0.0002
$\psi(2S)$	0.0012	0.0012	0.0013	0.0013	0.0013	0.0013	0.0014	0.0014	0.0014	0.0015
Other Bckg	0.0002	0.0000	0.0000	0.0000	0.0000	0.0000	0.0000	0.0000	0.0000	0.0000
Secondary Tags	0.0002	0.0003	0.0006	0.0008	0.0010	0.0011	0.0011	0.0012	0.0013	0.0013
$\mathcal{B}(b \rightarrow ue\nu)$	0.0015	0.0015	0.0015	0.0015	0.0015	0.0015	0.0016	0.0016	0.0017	0.0018
$b \rightarrow ue\nu$ Shape	0.0011	0.0011	0.0011	0.0011	0.0011	0.0011	0.0011	0.0010	0.0010	0.0009
EID	0.0129	0.0116	0.0102	0.0087	0.0073	0.0063	0.0066	0.0074	0.0095	0.0097
Fake μ Tags	0.0004	0.0003	0.0001	0.0001	0.0000	0.0001	0.0001	0.0001	0.0001	0.0001
Track Quality Eff.	0.0001	0.0001	0.0000	0.0000	0.0000	0.0001	0.0000	0.0001	0.0001	0.0000
Diagonal Cut Eff.	0.0007	0.0007	0.0005	0.0007	0.0003	0.0004	0.0004	0.0003	0.0002	0.0000
Veto Eff.	0.0006	0.0004	0.0003	0.0002	0.0002	0.0002	0.0001	0.0001	0.0001	0.0001
B Boost	0.0014	0.0012	0.0009	0.0009	0.0019	0.0010	0.0012	0.0016	0.0018	0.0011
Electroweak Rad.	0.0159	0.0138	0.0121	0.0100	0.0093	0.0084	0.0080	0.0068	0.0050	0.0031
B^0 Mixing χ	0.0025	0.0017	0.0012	0.0008	0.0006	0.0004	0.0003	0.0002	0.0001	0.0001
$\Delta(p)$	0.0024	0.0018	0.0012	0.0009	0.0006	0.0004	0.0003	0.0002	0.0001	0.0000
Corrected Moment	2.1856	2.2419	2.3066	2.3923	2.4890	2.6003	2.7259	2.8720	3.0192	3.1972
Statistical Error	0.0112	0.0097	0.0090	0.0085	0.0082	0.0080	0.0078	0.0078	0.0079	0.0081
Systematic Error	0.0271	0.0216	0.0177	0.0144	0.0127	0.0111	0.0109	0.0106	0.0112	0.0107
Total Error	0.0293	0.0237	0.0199	0.0168	0.0151	0.0136	0.0134	0.0132	0.0137	0.0134

Table 7.2: Breakdown of corrections and errors on $\langle E_\ell^2 \rangle$ at various lower lepton energy cuts. All numbers are in GeV^2.

E_ℓ cut (GeV) $\rightarrow$	**0.6**	**0.7**	**0.8**	**0.9**	**1.0**	**1.1**	**1.2**	**1.3**	**1.4**	**1.5**
Uncorr. Moment	0.1552	0.1396	0.1246	0.1084	0.0934	0.0791	0.0660	0.0535	0.0432	0.0336
Boost Corr.	-0.0027	-0.0027	-0.0025	-0.0026	-0.0025	-0.0025	-0.0025	-0.0024	-0.0023	-0.0023
A&M Corr.	0.0003	0.0005	0.0006	0.0007	0.0007	0.0007	0.0006	0.0006	0.0005	0.0004
PHOTOS Corr.	0.0000	0.0005	0.0008	0.0010	0.0009	0.0008	0.0007	0.0006	0.0005	0.0004
Continuum Sub.	0.0003	0.0002	0.0001	0.0001	0.0001	0.0001	0.0001	0.0001	0.0001	0.0001
J/ψ	0.0000	0.0000	0.0000	0.0000	0.0000	0.0000	0.0000	0.0000	0.0000	0.0000
π^0	0.0001	0.0001	0.0000	0.0000	0.0000	0.0000	0.0000	0.0000	0.0000	0.0000
γ	0.0006	0.0002	0.0001	0.0001	0.0000	0.0000	0.0000	0.0000	0.0000	0.0000
Same B Sec.	0.0014	0.0006	0.0002	0.0001	0.0001	0.0000	0.0000	0.0000	0.0000	0.0000
Upper Vertex D_s	0.0017	0.0009	0.0005	0.0003	0.0001	0.0000	0.0000	0.0000	0.0000	0.0000
Upper Vertex D	0.0014	0.0008	0.0003	0.0002	0.0001	0.0000	0.0000	0.0000	0.0000	0.0000
τ	0.0005	0.0003	0.0002	0.0001	0.0001	0.0000	0.0000	0.0000	0.0000	0.0000
$\psi(2S)$	0.0002	0.0002	0.0002	0.0002	0.0002	0.0001	0.0001	0.0001	0.0001	0.0001
Other Bckg	0.0001	0.0000	0.0000	0.0000	0.0000	0.0000	0.0000	0.0000	0.0000	0.0000
Secondary Tags	0.0003	0.0003	0.0002	0.0001	0.0001	0.0001	0.0001	0.0001	0.0001	0.0001
$\mathcal{B}(b \rightarrow ue\nu)$	0.0002	0.0002	0.0002	0.0002	0.0002	0.0002	0.0002	0.0002	0.0002	0.0002
$b \rightarrow ue\nu$ Shape	0.0001	0.0001	0.0001	0.0001	0.0001	0.0001	0.0001	0.0001	0.0000	0.0000
EID	0.0013	0.0010	0.0009	0.0008	0.0010	0.0011	0.0012	0.0011	0.0010	0.0010
Fake μ Tags	0.0001	0.0001	0.0001	0.0000	0.0000	0.0000	0.0000	0.0000	0.0000	0.0000
Track Quality Eff.	0.0000	0.0000	0.0000	0.0000	0.0000	0.0000	0.0000	0.0000	0.0000	0.0000
Diagonal Cut Eff.	0.0000	0.0000	0.0000	0.0000	0.0000	0.0000	0.0000	0.0000	0.0000	0.0000
Veto Eff.	0.0001	0.0000	0.0000	0.0000	0.0000	0.0000	0.0000	0.0000	0.0000	0.0000
B Boost	0.0001	0.0001	0.0001	0.0001	0.0000	0.0001	0.0001	0.0000	0.0000	0.0000
Electroweak Rad.	0.0003	0.0000	0.0001	0.0003	0.0002	0.0001	0.0000	0.0000	0.0000	0.0000
B^0 Mixing χ	0.0004	0.0002	0.0001	0.0000	0.0000	0.0000	0.0000	0.0000	0.0000	0.0000
$\Delta(p)$	0.0003	0.0002	0.0001	0.0001	0.0000	0.0000	0.0000	0.0000	0.0000	0.0000
Corrected Moment	0.1526	0.1374	0.1228	0.1068	0.0918	0.0775	0.0642	0.0516	0.0413	0.0316
Statistical Error	0.0021	0.0015	0.0013	0.0011	0.0010	0.0009	0.0009	0.0008	0.0008	0.0008
Systematic Error	0.0031	0.0018	0.0012	0.0010	0.0011	0.0012	0.0012	0.0011	0.0010	0.0010
Total Error	0.0037	0.0024	0.0017	0.0015	0.0015	0.0015	0.0015	0.0014	0.0013	0.0013

Table 7.3: Breakdown of corrections and errors on $\langle (E_\ell - \langle E_\ell \rangle)^2 \rangle$ at various lower lepton energy cuts. All numbers are in GeV^2.

E_ℓ cut (GeV) $\rightarrow$	**0.6**	**0.7**	**0.8**	**0.9**	**1.0**	**1.1**	**1.2**	**1.3**	**1.4**	**1.5**
Uncorr. Moment	-0.0062	-0.0021	0.0008	0.0029	0.0041	0.0046	0.0046	0.0043	0.0038	0.0031
Boost Corr.	-0.0015	-0.0014	-0.0014	-0.0013	-0.0012	-0.0011	-0.0010	-0.0009	-0.0008	-0.0007
A&M Corr.	-0.0013	-0.0011	-0.0009	-0.0007	-0.0005	-0.0003	-0.0002	-0.0001	-0.0001	-0.0000
PHOTOS Corr.	-0.0022	-0.0018	-0.0014	-0.0011	-0.0008	-0.0006	-0.0004	-0.0003	-0.0001	-0.0001
Continuum Sub.	0.0001	0.0001	0.0001	0.0001	0.0000	0.0000	0.0000	0.0000	0.0000	0.0000
J/ψ	0.0000	0.0000	0.0000	0.0000	0.0000	0.0000	0.0000	0.0000	0.0000	0.0000
π^0	0.0000	0.0000	0.0000	0.0000	0.0000	0.0000	0.0000	0.0000	0.0000	0.0000
γ	0.0000	0.0000	0.0000	0.0000	0.0000	0.0000	0.0000	0.0000	0.0000	0.0000
Same B Sec.	0.0001	0.0000	0.0000	0.0000	0.0000	0.0000	0.0000	0.0000	0.0000	0.0000
Upper Vertex D_s	0.0002	0.0002	0.0002	0.0001	0.0001	0.0000	0.0000	0.0000	0.0000	0.0000
Upper Vertex D	0.0001	0.0001	0.0001	0.0001	0.0000	0.0000	0.0000	0.0000	0.0000	0.0000
τ	0.0002	0.0001	0.0001	0.0001	0.0000	0.0000	0.0000	0.0000	0.0000	0.0000
$\psi(2S)$	0.0000	0.0000	0.0000	0.0000	0.0000	0.0000	0.0000	0.0000	0.0000	0.0000
Other Bckg	0.0000	0.0000	0.0000	0.0000	0.0000	0.0000	0.0000	0.0000	0.0000	0.0000
Secondary Tags	0.0000	0.0000	0.0000	0.0000	0.0000	0.0000	0.0000	0.0000	0.0000	0.0000
$\mathcal{B}(b \rightarrow ue\nu)$	0.0001	0.0001	0.0001	0.0001	0.0001	0.0001	0.0001	0.0001	0.0001	0.0001
$b \rightarrow ue\nu$ Shape	0.0001	0.0000	0.0000	0.0000	0.0000	0.0000	0.0000	0.0000	0.0000	0.0000
EID	0.0004	0.0005	0.0005	0.0006	0.0006	0.0005	0.0005	0.0004	0.0004	0.0004
Fake μ Tags	0.0000	0.0000	0.0000	0.0000	0.0000	0.0000	0.0000	0.0000	0.0000	0.0000
Track Quality Eff.	0.0000	0.0000	0.0000	0.0000	0.0000	0.0000	0.0000	0.0000	0.0000	0.0000
Diagonal Cut Eff.	0.0000	0.0000	0.0000	0.0000	0.0000	0.0000	0.0000	0.0000	0.0000	0.0000
Veto Eff.	0.0000	0.0000	0.0000	0.0000	0.0000	0.0000	0.0000	0.0000	0.0000	0.0000
B Boost	0.0000	0.0000	0.0000	0.0000	0.0000	0.0000	0.0000	0.0000	0.0000	0.0000
Electroweak Rad.	0.0009	0.0007	0.0006	0.0004	0.0003	0.0003	0.0002	0.0001	0.0001	0.0000
B^0 Mixing χ	0.0000	0.0000	0.0000	0.0000	0.0000	0.0000	0.0000	0.0000	0.0000	0.0000
$\Delta(p)$	0.0001	0.0001	0.0001	0.0000	0.0000	0.0000	0.0000	0.0000	0.0000	0.0000
Corrected Moment	-0.0099	-0.0053	-0.0020	0.0004	0.0020	0.0029	0.0032	0.0031	0.0028	0.0023
Statistical Error	0.0008	0.0007	0.0006	0.0006	0.0005	0.0005	0.0004	0.0004	0.0004	0.0003
Systematic Error	0.0010	0.0009	0.0008	0.0007	0.0007	0.0006	0.0005	0.0005	0.0004	0.0004
Total Error	0.0013	0.0011	0.0010	0.0009	0.0008	0.0008	0.0007	0.0006	0.0006	0.0005

Table 7.4: Breakdown of corrections and errors on $\langle (E_\ell - \langle E_\ell \rangle)^3 \rangle$ at various lower lepton energy cuts. All numbers are in GeV^3.

E_ℓ cut (GeV) →	**0.6**	**0.7**	**0.8**	**0.9**	**1.0**	**1.1**	**1.2**	**1.3**	**1.4**	**1.5**
No TOF	0.0003	0.0003	0.0003	0.0003	0.0003	0.0006	0.0006	0.0003	0.0002	0.0003
No dE/dx	0.0037	0.0033	0.0029	0.0024	0.0018	0.0014	0.0015	0.0018	0.0024	0.0024
Low E/p	0.0001	0.0001	0.0003	0.0004	0.0006	0.0002	0.0003	0.0003	0.0004	0.0002
High E/p	0.0008	0.0008	0.0008	0.0007	0.0007	0.0007	0.0005	0.0003	0.0003	0.0003
CEID tightened	0.0027	0.0020	0.0012	0.0003	0.0000	0.0000	0.0000	0.0000	0.0000	0.0000
EID	0.0046	0.0040	0.0033	0.0026	0.0021	0.0017	0.0017	0.0019	0.0025	0.0024

Table 7.5: Breakdown of electron ID systematic errors on $\langle E_\ell \rangle$ at various lower lepton energy cuts. All numbers are in GeV.

E_ℓ cut (GeV) →	**0.6**	**0.7**	**0.8**	**0.9**	**1.0**	**1.1**	**1.2**	**1.3**	**1.4**	**1.5**
No TOF	0.0010	0.0010	0.0011	0.0011	0.0012	0.0021	0.0021	0.0010	0.0008	0.0010
No dE/dx	0.0108	0.0101	0.0093	0.0081	0.0066	0.0055	0.0059	0.0072	0.0093	0.0095
Low E/p	0.0005	0.0007	0.0010	0.0014	0.0019	0.0009	0.0011	0.0013	0.0014	0.0007
High E/p	0.0025	0.0024	0.0024	0.0022	0.0021	0.0021	0.0017	0.0012	0.0012	0.0013
CEID tightened	0.0066	0.0050	0.0031	0.0008	0.0001	0.0000	0.0000	0.0000	0.0000	0.0000
EID	0.0129	0.0116	0.0102	0.0087	0.0073	0.0063	0.0066	0.0074	0.0095	0.0097

Table 7.6: Breakdown of electron ID systematic errors on $\langle E_\ell^2 \rangle$ at various lower lepton energy cuts. All numbers are in GeV^2.

E_ℓ cut (GeV) →	**0.6**	**0.7**	**0.8**	**0.9**	**1.0**	**1.1**	**1.2**	**1.3**	**1.4**	**1.5**
No TOF	0.0002	0.0002	0.0002	0.0002	0.0001	0.0000	0.0000	0.0001	0.0001	0.0001
No dE/dx	0.0004	0.0005	0.0006	0.0008	0.0010	0.0011	0.0012	0.0011	0.0010	0.0009
Low E/p	0.0003	0.0003	0.0002	0.0001	0.0001	0.0002	0.0002	0.0001	0.0001	0.0002
High E/p	0.0001	0.0001	0.0001	0.0001	0.0001	0.0000	0.0001	0.0001	0.0001	0.0001
CEID tightened	0.0011	0.0008	0.0005	0.0001	0.0000	0.0000	0.0000	0.0000	0.0000	0.0000
EID	0.0013	0.0010	0.0009	0.0008	0.0010	0.0011	0.0012	0.0011	0.0010	0.0010

Table 7.7: Breakdown of electron ID systematic errors on $\langle (E_\ell - \langle E_\ell \rangle)^2 \rangle$ at various lower lepton energy cuts. All numbers are in GeV^2.

E_ℓ cut (GeV) →	**0.6**	**0.7**	**0.8**	**0.9**	**1.0**	**1.1**	**1.2**	**1.3**	**1.4**	**1.5**
No TOF	0.0000	0.0000	0.0000	0.0000	0.0000	0.0000	0.0000	0.0000	0.0000	0.0000
No dE/dx	0.0004	0.0004	0.0005	0.0006	0.0006	0.0005	0.0005	0.0004	0.0004	0.0004
Low E/p	0.0001	0.0001	0.0001	0.0001	0.0001	0.0001	0.0001	0.0001	0.0001	0.0001
High E/p	0.0001	0.0001	0.0001	0.0000	0.0000	0.0000	0.0000	0.0000	0.0000	0.0000
CEID tightened	0.0001	0.0001	0.0000	0.0000	0.0000	0.0000	0.0000	0.0000	0.0000	0.0000
EID	0.0004	0.0005	0.0005	0.0006	0.0006	0.0005	0.0005	0.0004	0.0004	0.0004

Table 7.8: Breakdown of electron ID systematic errors on $\langle (E_\ell - \langle E_\ell \rangle)^3 \rangle$ at various lower lepton energy cuts. All numbers are in GeV^3.

statistical error is independent of the systematic error, and therefore also to be added in quadrature in the total error determination.

However, since each moment is calculated from the same spectrum, their errors are all correlated. Before we can use multiple moments in the determination of the HQET parameters, we need to quantatively determine the correlations between them. The method for obtaining the correlation matrices given in Tables 7.9-7.18 is described here.

To get the statistical errors and the correlations between two moments a and b, we use a toy Monte Carlo. We first obtain a "varied" spectrum by rolling a new value for each momentum bin according to the central value and statistical error of the measured spectrum, and the differences δa and δb between a and b from the varied spectrum and from the measured spectrum are calculated. The average δa and δb from $n = 10,000$ "varied" spectra are used to build the covariance matrix $C(a, b)$:

$$C(a,b) = \frac{1}{n}\sum_{i=1}^{n}\begin{pmatrix} (\delta a)_i^2 & (\delta a)_i(\delta b)_i \\ (\delta a)_i(\delta b)_i & (\delta b)_i^2 \end{pmatrix}. \tag{7.2}$$

The total systematic error on each moment is just the quadrature sum of the individual systematic errors for that moment as reported in Tables 7.1-7.4.

The calculation of the covariance of the systematic errors on moments a and b is similar in form to the method used for the statistical correlations. Instead of randomly generating our "varied" spectra, we use each systematic variation as a "varied" spectrum, and calculate the covariance matrix as described above. We include the statistical errors in this method as just another "varied" spectrum, and therefore obtain the total (systematic and statistical) covariance matrix. With this method, the

	0.6	**0.7**	**0.8**	**0.9**	**1.0**	**1.1**	**1.2**	**1.3**	**1.4**	**1.5**
0.6	1.000	0.951	0.888	0.807	0.722	0.662	0.624	0.587	0.525	0.455
0.7		1.000	0.955	0.886	0.808	0.750	0.715	0.680	0.618	0.543
0.8			1.000	0.949	0.881	0.825	0.792	0.758	0.696	0.618
0.9				1.000	0.945	0.888	0.852	0.817	0.753	0.674
1.0					1.000	0.940	0.902	0.858	0.779	0.686
1.1						1.000	0.948	0.881	0.782	0.693
1.2							1.000	0.934	0.837	0.746
1.3								1.000	0.928	0.843
1.4									1.000	0.938
1.5										1.000

Table 7.9: Correlations between measurements of $\langle E_\ell \rangle$ for various lower lepton energy cuts.

correlation of a and b due to any single variation is assumed to be 100%, but because each of the variations will yield a different ratio of δa to δb, the total covariance matrix will not 100% correlated.

We report the correlation matrices $\mathcal{C}(a,b)$ between various moments and lepton energy cuts in Tables 7.9-7.16 below. The correlation matrix is related to the covariance matrix by the relation

$$\mathcal{C}(a,b) = \sum_{i=1}^{n} \begin{pmatrix} \frac{(\delta a)_i^2}{\sigma_a^2} & \frac{(\delta a)_i (\delta b)_i}{\sigma_a \sigma_b} \\ \frac{(\delta a)_i (\delta b)_i}{\sigma_a \sigma_b} & \frac{(\delta b)_i^2}{\sigma_b^2} \end{pmatrix}, \tag{7.3}$$

where $\sigma_a = \sqrt{\sum_i^n (\delta a)_i^2}$ and $\sigma_b = \sqrt{\sum_i^n (\delta b)_i^2}$ are the total errors on a and b.

	0.6	**0.7**	**0.8**	**0.9**	**1.0**	**1.1**	**1.2**	**1.3**	**1.4**	**1.5**
0.6	0.996	0.939	0.871	0.790	0.713	0.658	0.619	0.578	0.515	0.447
0.7	0.966	0.996	0.944	0.874	0.802	0.749	0.713	0.672	0.608	0.535
0.8	0.918	0.968	0.996	0.941	0.878	0.827	0.792	0.751	0.685	0.610
0.9	0.850	0.915	0.962	0.996	0.944	0.892	0.854	0.811	0.744	0.666
1.0	0.773	0.847	0.906	0.954	0.996	0.941	0.900	0.848	0.766	0.676
1.1	0.716	0.794	0.857	0.906	0.948	0.995	0.941	0.868	0.768	0.681
1.2	0.682	0.763	0.830	0.880	0.921	0.959	0.995	0.923	0.824	0.735
1.3	0.650	0.735	0.804	0.855	0.891	0.913	0.953	0.996	0.918	0.834
1.4	0.592	0.679	0.749	0.801	0.825	0.834	0.880	0.949	0.998	0.934
1.5	0.522	0.606	0.675	0.727	0.743	0.756	0.802	0.880	0.951	0.999

Table 7.10: Correlations between measurements of $\langle E_\ell \rangle$ (rows) and $\langle E_\ell^2 \rangle$ (columns) for various lower lepton energy cuts.

	0.6	**0.7**	**0.8**	**0.9**	**1.0**	**1.1**	**1.2**	**1.3**	**1.4**	**1.5**
0.6	-0.651	-0.436	-0.163	0.132	0.274	0.323	0.310	0.301	0.299	0.299
0.7	-0.457	-0.369	-0.090	0.212	0.354	0.402	0.386	0.375	0.372	0.371
0.8	-0.285	-0.164	-0.011	0.287	0.421	0.468	0.449	0.439	0.436	0.434
0.9	-0.126	0.024	0.194	0.343	0.466	0.515	0.497	0.488	0.486	0.484
1.0	-0.003	0.164	0.340	0.482	0.461	0.511	0.487	0.477	0.474	0.473
1.1	0.066	0.240	0.422	0.569	0.557	0.488	0.465	0.463	0.466	0.459
1.2	0.122	0.304	0.496	0.657	0.657	0.607	0.513	0.511	0.514	0.507
1.3	0.171	0.363	0.570	0.747	0.768	0.752	0.687	0.624	0.624	0.619
1.4	0.214	0.409	0.624	0.808	0.860	0.876	0.842	0.805	0.758	0.752
1.5	0.242	0.434	0.647	0.827	0.899	0.920	0.908	0.893	0.869	0.820

Table 7.11: Correlations between measurements of $\langle E_\ell \rangle$ (rows) and $\langle (E_\ell - \langle E_\ell \rangle)^2 \rangle$ (columns) for various lower lepton energy cuts.

	0.6	**0.7**	**0.8**	**0.9**	**1.0**	**1.1**	**1.2**	**1.3**	**1.4**	**1.5**
0.6	-0.412	-0.407	-0.297	-0.163	-0.060	0.021	0.080	0.146	0.195	0.241
0.7	-0.507	-0.408	-0.286	-0.142	-0.030	0.058	0.123	0.196	0.250	0.301
0.8	-0.521	-0.436	-0.275	-0.124	-0.004	0.090	0.161	0.239	0.298	0.352
0.9	-0.486	-0.412	-0.279	-0.114	0.013	0.114	0.190	0.273	0.335	0.391
1.0	-0.461	-0.397	-0.288	-0.160	-0.033	0.073	0.154	0.242	0.310	0.371
1.1	-0.421	-0.362	-0.266	-0.163	-0.069	0.029	0.121	0.217	0.288	0.348
1.2	-0.334	-0.266	-0.169	-0.075	0.005	0.077	0.153	0.253	0.327	0.390
1.3	-0.180	-0.096	0.010	0.105	0.179	0.238	0.285	0.360	0.434	0.498
1.4	0.021	0.121	0.235	0.333	0.405	0.455	0.485	0.528	0.571	0.631
1.5	0.170	0.275	0.388	0.484	0.550	0.593	0.617	0.645	0.661	0.692

Table 7.12: Correlations between measurements of $\langle E_\ell \rangle$ (rows) and $\langle (E_\ell - \langle E_\ell \rangle)^3 \rangle$ (columns) for various lower lepton energy cuts.

	0.6	**0.7**	**0.8**	**0.9**	**1.0**	**1.1**	**1.2**	**1.3**	**1.4**	**1.5**
0.6	1.000	0.961	0.908	0.839	0.768	0.716	0.681	0.642	0.582	0.514
0.7		1.000	0.965	0.909	0.846	0.798	0.766	0.730	0.670	0.599
0.8			1.000	0.961	0.909	0.864	0.835	0.800	0.740	0.668
0.9				1.000	0.960	0.917	0.887	0.853	0.793	0.720
1.0					1.000	0.956	0.925	0.886	0.816	0.734
1.1						1.000	0.961	0.906	0.824	0.747
1.2							1.000	0.949	0.871	0.794
1.3								1.000	0.944	0.874
1.4									1.000	0.950
1.5										1.000

Table 7.13: Correlations between measurements of $\langle E_\ell^2 \rangle$ for various lower lepton energy cuts.

	0.6	**0.7**	**0.8**	**0.9**	**1.0**	**1.1**	**1.2**	**1.3**	**1.4**	**1.5**
0.6	-0.581	-0.367	-0.093	0.201	0.340	0.387	0.373	0.364	0.361	0.360
0.7	-0.391	-0.286	-0.011	0.284	0.419	0.465	0.447	0.437	0.434	0.432
0.8	-0.227	-0.091	0.075	0.360	0.486	0.529	0.509	0.498	0.495	0.492
0.9	-0.079	0.083	0.264	0.421	0.533	0.576	0.556	0.547	0.544	0.541
1.0	0.031	0.208	0.396	0.548	0.538	0.580	0.555	0.545	0.541	0.538
1.1	0.096	0.279	0.473	0.631	0.631	0.572	0.548	0.543	0.545	0.537
1.2	0.145	0.335	0.538	0.707	0.718	0.678	0.594	0.590	0.591	0.584
1.3	0.188	0.385	0.598	0.779	0.810	0.801	0.744	0.688	0.686	0.680
1.4	0.224	0.420	0.638	0.823	0.881	0.900	0.872	0.839	0.797	0.790
1.5	0.248	0.440	0.654	0.834	0.910	0.935	0.926	0.914	0.894	0.850

Table 7.14: Correlations between measurements of $\langle E_\ell^2 \rangle$ (rows) and $\langle (E_\ell - \langle E_\ell \rangle)^2 \rangle$ (columns) for various lower lepton energy cuts.

	0.6	**0.7**	**0.8**	**0.9**	**1.0**	**1.1**	**1.2**	**1.3**	**1.4**	**1.5**
0.6	-0.406	-0.386	-0.269	-0.130	-0.023	0.062	0.125	0.194	0.246	0.294
0.7	-0.476	-0.376	-0.249	-0.102	0.013	0.103	0.170	0.245	0.301	0.353
0.8	-0.475	-0.387	-0.228	-0.076	0.043	0.138	0.209	0.289	0.348	0.403
0.9	-0.429	-0.351	-0.217	-0.057	0.068	0.167	0.242	0.325	0.387	0.443
1.0	-0.397	-0.326	-0.212	-0.085	0.038	0.141	0.220	0.306	0.373	0.432
1.1	-0.349	-0.280	-0.178	-0.071	0.023	0.117	0.204	0.296	0.364	0.423
1.2	-0.263	-0.186	-0.083	0.016	0.097	0.168	0.240	0.335	0.404	0.464
1.3	-0.118	-0.027	0.083	0.181	0.257	0.316	0.361	0.432	0.499	0.559
1.4	0.063	0.166	0.282	0.383	0.455	0.505	0.535	0.577	0.616	0.672
1.5	0.200	0.307	0.423	0.520	0.587	0.631	0.655	0.683	0.699	0.727

Table 7.15: Correlations between measurements of $\langle E_\ell^2 \rangle$ (rows) and $\langle (E_\ell - \langle E_\ell \rangle)^3 \rangle$ (columns) for various lower lepton energy cuts.

	0.6	**0.7**	**0.8**	**0.9**	**1.0**	**1.1**	**1.2**	**1.3**	**1.4**	**1.5**
0.6	1.000	0.848	0.673	0.475	0.342	0.289	0.271	0.268	0.266	0.261
0.7		1.000	0.846	0.659	0.523	0.468	0.443	0.438	0.435	0.429
0.8			1.000	0.850	0.725	0.669	0.639	0.630	0.626	0.616
0.9				1.000	0.900	0.842	0.803	0.788	0.781	0.769
1.0					1.000	0.939	0.905	0.892	0.885	0.871
1.1						1.000	0.968	0.947	0.934	0.924
1.2							1.000	0.977	0.962	0.952
1.3								1.000	0.984	0.972
1.4									1.000	0.986
1.5										1.000

Table 7.16: Correlations between measurements of $\langle (E_\ell - \langle E_\ell \rangle)^2 \rangle$ for various lower lepton energy cuts.

	0.6	**0.7**	**0.8**	**0.9**	**1.0**	**1.1**	**1.2**	**1.3**	**1.4**	**1.5**
0.6	0.222	0.340	0.332	0.288	0.260	0.242	0.234	0.229	0.227	0.224
0.7	0.388	0.370	0.385	0.360	0.347	0.342	0.346	0.354	0.362	0.368
0.8	0.437	0.476	0.452	0.450	0.454	0.463	0.477	0.499	0.517	0.533
0.9	0.381	0.467	0.522	0.526	0.542	0.561	0.583	0.616	0.644	0.669
1.0	0.385	0.493	0.589	0.650	0.669	0.683	0.701	0.730	0.751	0.773
1.1	0.394	0.509	0.621	0.707	0.757	0.776	0.781	0.799	0.815	0.835
1.2	0.434	0.550	0.663	0.755	0.813	0.845	0.851	0.854	0.859	0.871
1.3	0.451	0.565	0.679	0.772	0.833	0.871	0.889	0.897	0.892	0.895
1.4	0.453	0.567	0.680	0.776	0.838	0.879	0.905	0.924	0.924	0.917
1.5	0.452	0.566	0.681	0.778	0.843	0.887	0.917	0.940	0.948	0.946

Table 7.17: Correlations between measurements of $\langle (E_\ell - \langle E_\ell \rangle)^2 \rangle$ (rows) and $\langle (E_\ell - \langle E_\ell \rangle)^3 \rangle$ (columns) for various lower lepton energy cuts.

	0.6	**0.7**	**0.8**	**0.9**	**1.0**	**1.1**	**1.2**	**1.3**	**1.4**	**1.5**
0.6	1.000	0.942	0.900	0.838	0.774	0.711	0.657	0.592	0.538	0.490
0.7		1.000	0.972	0.925	0.868	0.811	0.759	0.697	0.645	0.600
0.8			1.000	0.979	0.940	0.895	0.850	0.796	0.749	0.708
0.9				1.000	0.986	0.958	0.923	0.878	0.837	0.801
1.0					1.000	0.990	0.966	0.931	0.896	0.865
1.1						1.000	0.991	0.966	0.938	0.911
1.2							1.000	0.990	0.969	0.945
1.3								1.000	0.992	0.975
1.4									1.000	0.993
1.5										1.000

Table 7.18: Correlations between measurements of $\langle (E_\ell - \langle E_\ell \rangle)^3 \rangle$ for various lower lepton energy cuts.

CHAPTER 8

Interpretation and Conclusions

In this thesis a new measurement of the inclusive momentum spectrum for semileptonic B-meson decays using events with a high-momentum lepton tag and a signal electron in the full data sample collected with the CLEO II detector has been presented. Improvements in the understanding of background processes and optimized electron-identification procedures have resulted in significant improvements in systematic uncertainties relative to the previous CLEO measurement [25].

8.1 Branching Ratio

We have used the normalization of the measured spectrum and an extrapolation for $0 < E_\ell < 0.6$ GeV based on a detailed model calculation constrained by data to obtain a new measurement of the B semileptonic branching fraction, $\mathcal{B}(B \to Xe\nu) = (10.91 \pm 0.09 \pm 0.24)\%$, as described in Chapter 6. Fig 8.1 shows that this result is in excellent agreement with other recent measurements at the $\Upsilon(4S)$ [49, 50] and has better overall precision. These results have diminished the level of disagreement between measurements made at the $\Upsilon(4S)$ and those from Z^0 decays [51]. The difference of this measurement and the measurement made by CLEO in 1995 [25]

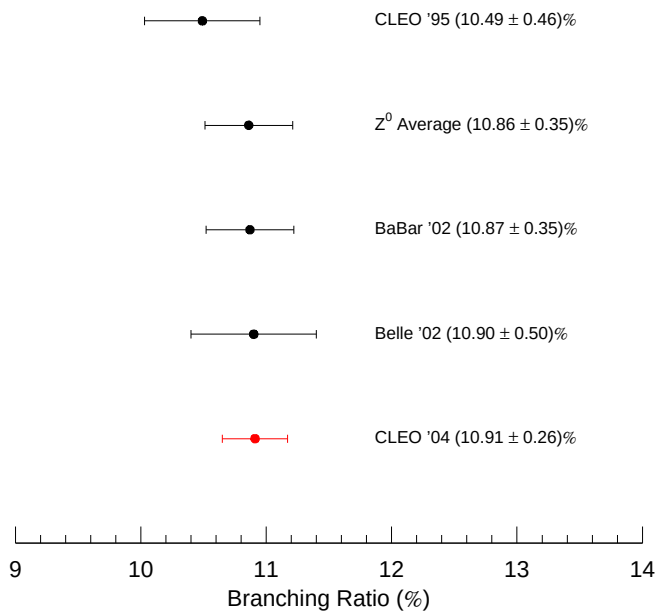

Figure 8.1: Measurements of the semileptonic branching ratio. The measurement presented in this thesis is shown in red.

using the same tagging strategy as this thesis can be partially attributed to the problem with the relative event selection efficiency described in Sect. 6.1.2. When corrected for this effect, the 1995 measurement becomes 10.82%, within 0.3 total σ of the result presented here.

For several years, the measured B semileptonic branching ratio has been below the theoretical calculations [52]. These began with a niave expectation of $\mathcal{B}(B \to X\ell\nu) \sim 15\%$, which after inclusion of hadronic effects, becomes $\sim 12.5\%$. Possible explanations of this discrepancy include

- larger than expected non-perturbative corrections increasing the width for $b \to c\bar{c}s$ transitions,

- rates for flavor-changing-neutral current (FCNC) proceses, such as $b \to s\gamma$, $b \to sg$, or $b \to sq\bar{q}$, that are larger than Standard Model predictions, and
- the intervention of new physics in B decay.

The first of these explanations, an increase in $\Gamma(b \to c\bar{c}s)$ to compensate for the "missing" rate left by the low semileptonic rate, would lead to an increase in the number of charm quarks per B decay $\langle n_c \rangle$, which was expected to be about 1.3. The experimental value of this number, however, is *already lower* than this prediction, with CLEO [53] measuring $\langle n_c \rangle = 1.10 \pm 0.05$.[1] . Thus, any mechanism that increases the expected $\langle n_c \rangle$ exacerbates the "charm counting" problem. Experiment seems to rule out an enhancement of FCNC [55] as a solution, as measurements are in agreement with Standard Model predictions. The third explanation, physics beyond the Standard Model, is exciting but unlikely, as an effect large enough to resolve both the semileptonic banching fraction and charm counting problems would almost certainly have a noticeable signature in other aspects of b decays. There may be no single dramatic explanation of this discrepancy. Indeed, since the alarm about these problems was first sounded, measurements of both $\langle n_c \rangle$ and the branching ratio have lessened (but not eliminated) disagreement with theory.

8.1.1 The Semileptonic Rate

To obtain the semileptonic decay rate, we need three ingredients: the semileptonic branching fraction measured here, the B-meson lifetime, and the branching frac-

[1]The LEP experiments give a consistent measurement of the number of charm quarks per b decay at the Z^0 of $n_c = 1.15 \pm 0.06$ [54]

tion for $B \to X_u \ell\nu$. First, the small contribution from $B \to X_u \ell\nu$ decays must be subtracted from the measured branching ratio, as Eq. 2.31 requires the rate for $B \to X_c \ell\nu$. We now encounter a small subtlety in the extraction of the $B \to X_c \ell\nu$ rate from the $B \to X_c \ell\nu$ branching fraction. Because of isospin symmetry, we can assume that the rates for both B^+ and B^0 are equal. The branching ratios are not the same, however, since the lifetimes are not equal, $\tau_{B^+} = 1.542 \pm 0.0016 \neq \tau_{B^0} = 1.674 \pm 0.0018$ [10]. Since our analysis procedure does not discriminate between charged and neutral B's, our measurement of the semileptonic branching ratio is "charge-averaged," and applies specifically to the proportions of charged-B and neutral-B events produced at the $\Upsilon(4S)$. Taking this into account, the expression for the rate is

$$\Gamma(B \to X_c \ell\nu) = \frac{\hbar}{c} \frac{\mathcal{B}(B \to X_c \ell\nu)}{f_{+-}\tau_{B^+} + f_{00}\tau_{B^0}} \tag{8.1}$$

where f_{+-} and f_{00} are the fractions of charged-B and neutral-B events at the $\Upsilon(4S)$, respectively. Using the measured ratio of these fractions, $f_{+-}/f_{00} = 1.04 \pm 0.08$ [10], and the constraint $f_{+-} + f_{00} = 1$, we can obtain the rate $\Gamma(B \to X_c \ell\nu)$ from charge-averaged branching ratios measurements at the $\Upsilon(4S)$ from Eq. 8.1.

8.2 Moments, HQET Parameters, and $|V_{cb}|$

We have also used the measured spectrum to determine the moments of the electron-energy spectrum in semileptonic B decays with minimum energies ranging from 0.6 GeV to 1.5 GeV (Chap. 7). The measured value for the mean energy with $E_{min} = 1.5$ GeV/c, $\langle E_\ell \rangle_{1.5} = (1.7792 \pm 0.0021 \pm 0.0026)$ GeV, is in good agreement

with the previous CLEO measurement of this quantity [56], (1.7810±0.0007±0.0009) GeV. The earlier measurement was more precise because it used the entire inclusive spectrum for semileptonic B decays, without a lepton-tag requirement. That technique does not allow for measurements with smaller values of E_{min}, however, because of the large contribution of secondary charm decays. While electron-energy moments were not presented for the previous CLEO lepton-tagged measurement of $\mathcal{B}(B \to Xe\nu)$ [25], moment values computed from fits to that spectrum are consistent with the current measurements.

Measurements of moments of different quantities have sensitivity to different regions of phase space, and provide an ideal opportunity to test the description of inclusive B decays provided by the HQET/OPE methodology. Using the approach described in Chapter 2, expressions for many inclusive properties of B decays have been derived [11, 19], including the moments[2]. of the lepton energy and recoil hadronic mass in $B \to X_c \ell \nu$ and of the photon energy in $B \to X_s \gamma$.

Physical observables in HQET are expressed as expansions in Λ_{QCD}/M_B, with new parameters emerging at each order. Two formulations of the HQET expansion calculated to third order in Λ_{QCD}/M_B will be discussed in the following sections. The first formulation discussed is the that of Bauer, *et al.* in the "pole-mass" scheme presented in Ref. [11]. The second formulation discussed is that of Uraltsev, *et al.* in

[2]In what follows, I adopt a similar notation convention as used for the electron-energy moments. From here on, the first moment of the hadronic-mass-squared spectrum in semileptonic B decays will be written as $\langle M_X^2 - \bar{M}_D^2 \rangle$ and the first moment of the photon-energy spectrum for $B \to X_s \gamma$ decays will be written as $\langle E_\gamma \rangle$, with subscripts denoting minimum lepton-energy and photon-energy cuts in GeV, respectively.

the "kinetic" scheme, presented in Ref. [19]. For both, expressions for the semileptonic decay width and the moments of the various kinematic distributions are presented. These expressions provide an excellent opportunity to constrain the non-perturbative parameters using the several measured moments, and thereby test HQET and obtain results for $|V_{cb}|$.

8.2.1 Results in the Bauer Formulation

There are several non-perturbative expansion parameters defined in the Bauer formulation: $\overline{\Lambda}$ at order Λ_{QCD}/M_B, λ_1 and λ_2 at order $(\Lambda_{QCD}/M_B)^2$, and six parameters (ρ_1, ρ_2, $\mathcal{T}_1$, $\mathcal{T}_2$, $\mathcal{T}_3$, $\mathcal{T}_4$) at order $(\Lambda_{QCD}/M_B)^3$. Values have been calculated for the $M^{(i)}$'s in Eq. 2.34 for each type of moment at various minimum energy cuts [11].

The parameter λ_2 can be calculated from the $B^* - B$ and $D^* - D$ mass splittings:

$$\lambda_2 = \frac{m_B^2 \Delta m_B - m_D^2 \Delta m_D}{2(m_B - \kappa(m_c) m_D)} = (0.1255 \pm 0.001) GeV^2, \tag{8.2}$$

where Δm_B and Δm_D are the $B^* - B$ and $D^* - D$ mass splittings and $\kappa(m_c) = (\alpha_s(m_c)/\alpha_s(m_b))/\beta_0 \approx 1.2$ [57]. The uncertainty on λ_2 shown is experimental only, and is dominated by the $B^* - B$ mass splitting. Theoretical uncertainty is about 10%, but is small compared to other sources of uncertainty in the extraction of $\overline{\Lambda}$ and λ_1. The mass splittings also supply a constraint on the third-order parameters [57]:

$$\rho_2 - \mathcal{T}_2 - \mathcal{T}_4 = \frac{\kappa(m_c) m_B^2 \Delta m_B (m_D + \overline{\Lambda}) - m_D^2 \Delta m_D (m_B + \overline{\Lambda})}{m_B + \overline{\Lambda} - \kappa(m_c)(m_D + \overline{\Lambda})}. \tag{8.3}$$

With assumptions about the $(\Lambda_{QCD}/M_B)^3$ parameters, each moment defines a constraint on HQET, expressed as a band in $\overline{\Lambda} - \lambda_1$ space. To this end, the widths of

the bands presented in this section reflect the statistical and systematic uncertainties in the moment measurements and the theoretical uncertainties in the expansion parameters. The third-order parameters $\mathcal{T}_{1-4}$ are set to zero and varied by $(\pm 0.5\ \mathrm{GeV})^3$. The ρ_1 parameter is set to $(0.5 \pm 0.5)(0.5\ \mathrm{GeV})^3$ to satisfy the constraint that ρ_1 be positive definite, as suggested by the vacuum-saturation approximation [57]. The ϵ parameter denotes terms proportional to α_s, and is varied by $\pm 25\%$, corresponding to the range $\alpha_s(m_b/2)$ to $\alpha_s(2m_b)$. The parameter ϵ^2_{BLM}, corresponding to corrections of order $\alpha_s^2\beta_0$, is varied by 100%. The bands are calculated by scanning over a range of values for $\overline{\Lambda}$; for each $\overline{\Lambda}$, several sets of Gaussian-distributed random numbers are thrown, with variances appropriate to the parameters being varied. For each set of random numbers, a value for λ_1 is calculated using the varied parameters, $\overline{\Lambda}$, and Eq. 2.34. A mean μ and a variance σ are then calculated for λ_1. The value of λ_1 for that particular $\overline{\Lambda}$ is taken to be $\mu \pm 1\sigma$, with the variance interpreted as the one-sigma error on the mean.

The plots in Fig. 8.2 show our measured values of $\langle E_\ell \rangle$ as a function of the minimum lepton energy cut and the HQET/OPE predictions for the lepton-energy moments in the Bauer formulation. The plot on the left shows the measurements and the prediction, while the plot on the right shows the difference between the measurements and the prediction. The values for $\bar{\Lambda}$ and λ_1 are constrained by $\langle E_\gamma \rangle_{2.0} = 2.346 \pm 0.034$ GeV [17] and our measurement of $\langle E_\ell \rangle_{1.5}$. The error bars on the data points represent the combined statistical and systematic uncertainties of the measurements. There is substantial correlation among the data values for the different E_{min} cases. The width of the band is set by the uncertainty in the measurements of $\bar{\Lambda}$ and λ_1, variation of the

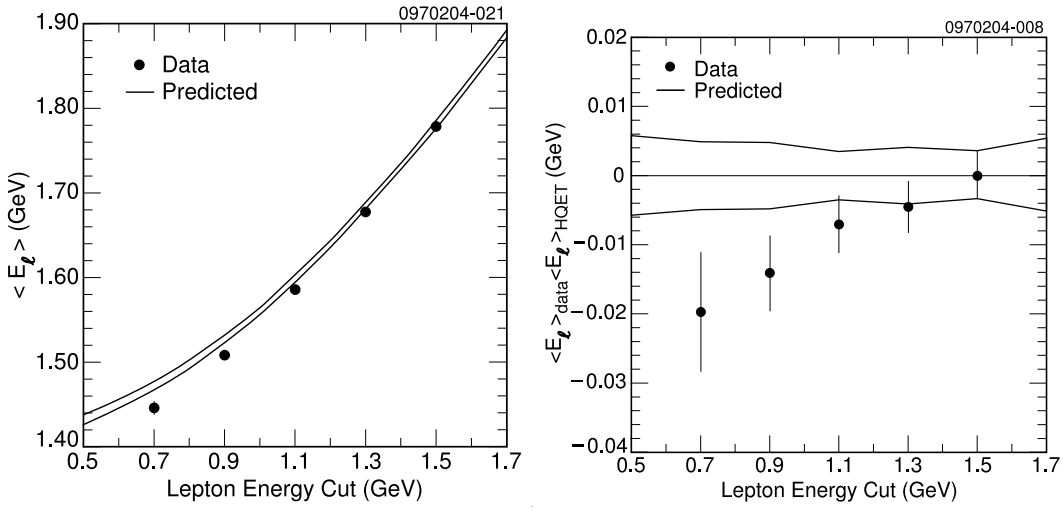

Figure 8.2: **Left:** $\langle E_\ell \rangle$ as a function of E_{min}. The points are data and the band is the $\pm 1\sigma$ prediction in the Bauer pole-mass scheme [11]. **Right:** $\langle E_\ell \rangle_{data} - \langle E_\ell \rangle_{HQET}$ as a function of E_{min}. The points are the data with the predicted moment subtacted, and the band is the $\pm 1\sigma$ prediction. Inputs for these plots were set by $\langle E_\gamma \rangle_{2.0}$ [17] and $\langle E_\ell \rangle_{1.5}$.

third-order expansion parameters, and variation of the perturbative QCD corrections.

As can be seen in Fig. 8.2, there is an increasing disagreement as E_{min} is reduced between the measured mean energy and the value extrapolated with HQET. These results have been obtained by using the PHOTOS algorithm [30] to correct for final-state radiation. There is considerable uncertainty in this correction, and if the prescription of Atwood and Marciano [48] were instead used, the disagreement between our measurement and the HQET computation would be increased by 25%. The difference between these two computations is the largest contribution to the systematic uncertainty in the measurement of the mean energy.

Fig. 8.3 shows four bands in the $\overline{\Lambda} - \lambda_1$ space. Along with bands for $\langle E_\ell \rangle_{0.7}$ and $\langle (E_\ell - \langle E_\ell \rangle)^2 \rangle_{0.7}$, bands for the difference of the mean $\langle E_\ell \rangle_{0.7} - \langle E_\ell \rangle_{1.5}$ and the difference in the variance $\langle (E_\ell - \langle E_\ell \rangle)^2 \rangle_{0.7} - \langle (E_\ell - \langle E_\ell \rangle)^2 \rangle_{1.5}$ are shown to isolate the information that is independent of the measurements of the moments with $E_\ell > 1.5$ GeV. The width of the bands indicates the combined experimental and theoretical uncertainties. As can be seen, the variance (band 2) and the difference in the variances (band 4) are compatible with other measurements [56], whereas the difference in the means (band 3) is the predominant source of disagreement between data and theory.

The HQET expansion parameters $\overline{\Lambda}$, $\lambda_{1,2}$, $\rho_{1,2}$, and $\mathcal{T}_{1-4}$ are internal to the theory; they depend on the particular renormalization scheme used in the calculation of the HQET expansion. They are useful only to the extent that they can be used to extract physical observables like decay rates and CKM matrix elements. To this end, values of the expansion parameters obtained from moments measurements can be used in Eq. 2.31 to extract $|V_{cb}|$ from the $B \to X_c \ell \nu$ decay rate.

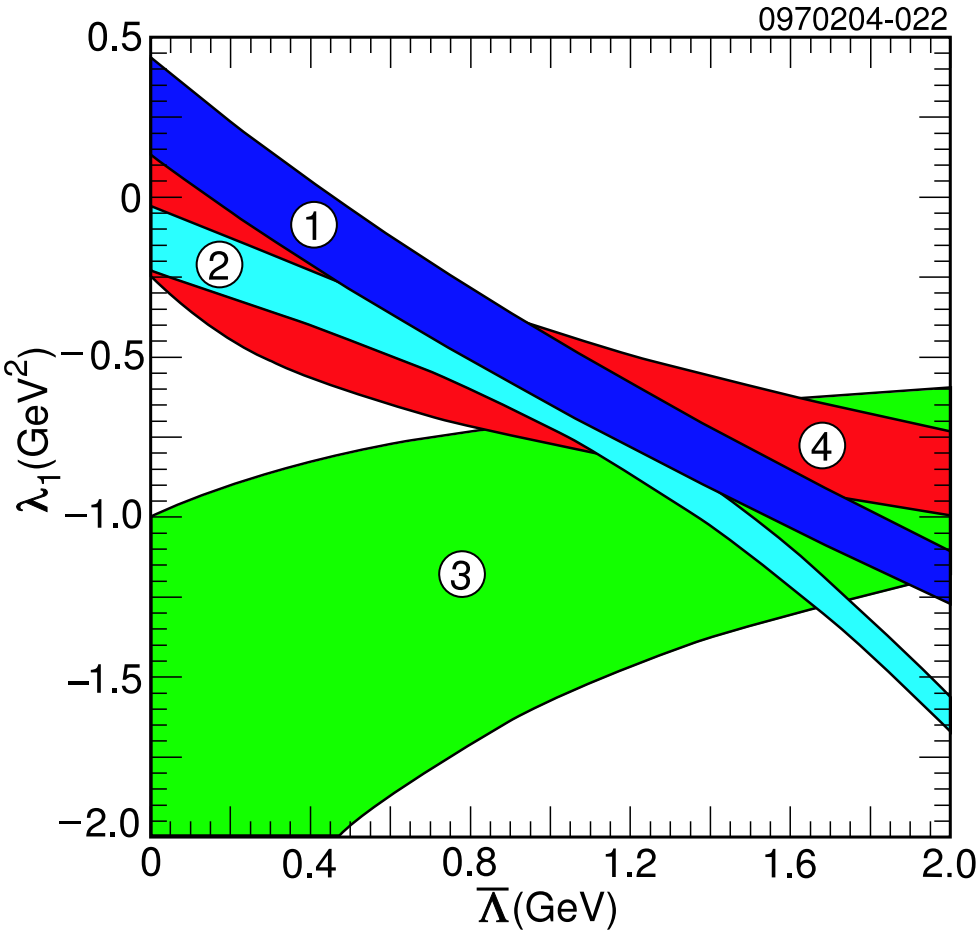

Figure 8.3: Bands in the $\overline{\Lambda} - \lambda_1$ plane from $\langle E_\ell \rangle$ with $E_\ell > 0.7$ GeV (band 1), $\langle (E_\ell - \langle E_\ell \rangle)^2 \rangle$ with $E_\ell > 0.7$ GeV (band 2), $\langle E_\ell \rangle_{1.5} - \langle E_\ell \rangle_{0.7}$ (band 3), and $\langle (E_\ell - \langle E_\ell \rangle)^2 \rangle_{0.7} - \langle (E_\ell - \langle E_\ell \rangle)^2 \rangle_{1.5}$ (band 4). The widths of the bands reflect the combined experimental and theoretical uncertainties. These bands were calculated with the Bauer pole-mass formulation [11].

$|V_{cb}|$ in the Bauer Formulation

We need values for the HQET expansion parameters before we can extract $|V_{cb}|$ from Eq. 2.31. As described in Sect. 8.2, with assumptions about the third-order parameters a moment defines a band in $\overline{\Lambda} - \lambda_1$ space. If two moments measurements admit a solution for $\overline{\Lambda}$ and λ_1, these can then be used in Eq. 2.31 to extract $|V_{cb}|$.

In the pole-mass scheme, the moment $\langle E_\gamma \rangle$ is especially useful because its expression is independent of λ_1, so it directly yields a value of $\overline{\Lambda}$. Using the previously defined values for the other expansion parameters, the CLEO measurement of $\langle E_\gamma \rangle_{2.0}$ yields the result $\overline{\Lambda} = 0.33 \pm 0.07$ GeV, and the CLEO measurement of $\langle M_X^2 - \bar{M}_D^2 \rangle_{1.5} = 0.251 \pm 0.066$ GeV^2 [14] combined with this $\overline{\Lambda}$ gives $\lambda_1 = -0.236 \pm 0.071$ GeV^2 (see Fig. 8.4). The quoted errors on $\overline{\Lambda}$ and λ_1 are from the measurement uncertainties of the moments only; in this section we do not quote uncertainties on $\overline{\Lambda}$ and λ_1 from the other expansion parameters. We will account for these uncertainties only in the determination of $|V_{cb}|$ to avoid double-counting them. The previous CLEO measurement of the B semileptonic branching ratio [25] corrected for the small $B \to X_u \ell \nu$ contribution, $\mathcal{B}(B \to X_c \ell \nu) = 10.39 \pm 0.46$, gives the semileptonic rate $\Gamma(B \to X_c \ell \nu) = 4.27 \pm 0.20 \times 10^{-14}$ GeV. Plugging these inputs into Eq. 2.31 gives

$$|V_{cb}| = (4.05 \pm 0.10 \pm 0.06 \pm 0.19) \times 10^{-2}, \tag{8.4}$$

where the errors are from the measurements of $\Gamma(B \to X_c \ell \nu)$, the measurements of $\overline{\Lambda}$ and λ_1, and the uncertainty of the ρ's, $\mathcal{T}$'s, and α_s, respectively.

The measurement of the B semileptonic branching ratio presented in this thesis gives us better information about the semileptonic rate that can be used to improve

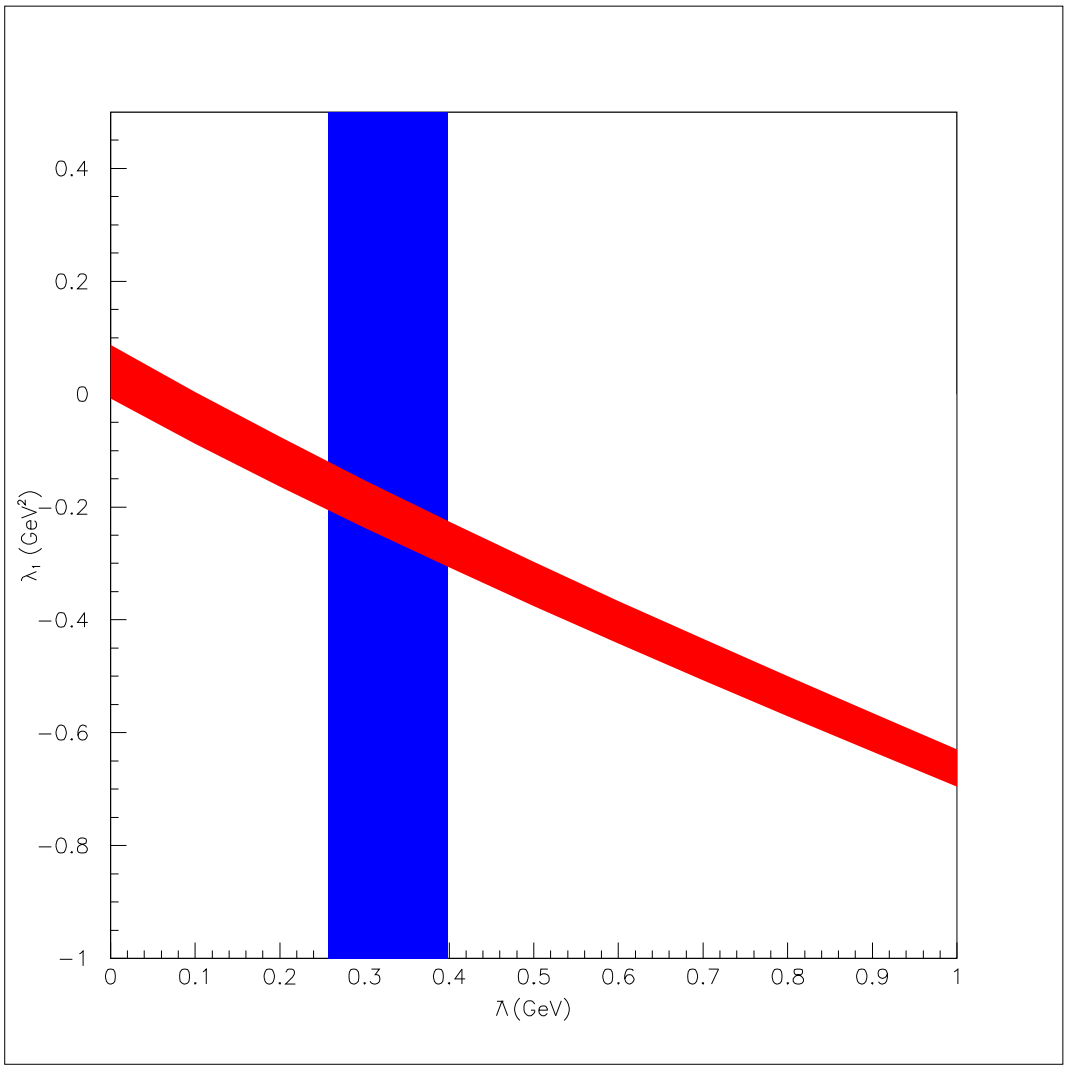

Figure 8.4: Bands in the $\overline{\Lambda} - \lambda_1$ plane for $\langle E_\gamma \rangle_{2.0}$ (blue) and $\langle M_X^2 - \bar{M}_D^2 \rangle_{1.5}$ (red). Widths of bands represent measurement uncertainty on the moments.

the precision of our determination of $|V_{cb}|$. After subtracting $\mathcal{B}(B \to X_u \ell\nu) = 0.18 \pm 0.04\%$ [34] from our measured branching ratio, we determine that the $B \to X_c \ell\nu$ decay rate is $\Gamma(B \to X_c \ell\nu) = 4.40 \pm 0.16 \times 10^{-14}$ GeV. When input into Eq. 2.31 with the $\overline{\Lambda}$ and λ_1 from $\langle M_X^2 - \bar{M}_D^2 \rangle_{1.5}$ and $\langle E_\gamma \rangle_{2.0}$ given above, we get

$$|V_{cb}| = (4.12 \pm 0.08 \pm 0.07 \pm 0.19) \times 10^{-2}, \tag{8.5}$$

while the new measurement increases the value of $|V_{cb}|$, it remains consistent within the experimental uncertainty.

The electron-energy moments reported in this thesis give us another set of constraints on HQET. When combined with $\langle E_\gamma \rangle_{2.0}$, the first electron-energy moment $\langle E_\ell \rangle_{1.5}$ [56] gives results consistent with Eq. 8.5. In principle, the moment $\langle E_\ell \rangle_{0.7}$ should be more desirable theoretically as it is more inclusive, covering more than twice as much phase space than $\langle E_\ell \rangle_{1.5}$. Thus, we expect it to be less apt to run afoul of the quark-hadron duality assumption. The bands from $\langle E_\ell \rangle_{0.7}$ and $\langle E_\gamma \rangle_{2.0}$ are shown in Fig. 8.5. With these moments, we obtain $\lambda_1 = -0.05 \pm 0.12$ GeV^2. Solving Eq. 2.31 gives

$$|V_{cb}| = (4.19 \pm 0.08 \pm 0.08 \pm 0.20) \times 10^{-2}. \tag{8.6}$$

It is interesting here to note that while the values for λ_1 given by $\langle E_\ell \rangle_{0.7}$ and $\langle M_X^2 - \bar{M}_D^2 \rangle_{1.5}$ for the value of $\overline{\Lambda}$ determined by $\langle E_\gamma \rangle_{2.0}$ differ by a fair amount, values of $|V_{cb}|$ given by these parameters agree well within quoted uncertainties.

A troubling situation occurs, however, if we use only moments measured in this thesis, namely $\langle E_\ell \rangle_{0.7}$ and $\langle (E_\ell - \langle E_\ell \rangle)^2 \rangle_{0.7} = 0.1374 \pm 0.0024$ GeV^2, we get bands in the $\overline{\Lambda} - \lambda_1$ plane as shown in Fig. 8.6. Since the bands do not cross, we cannot extract

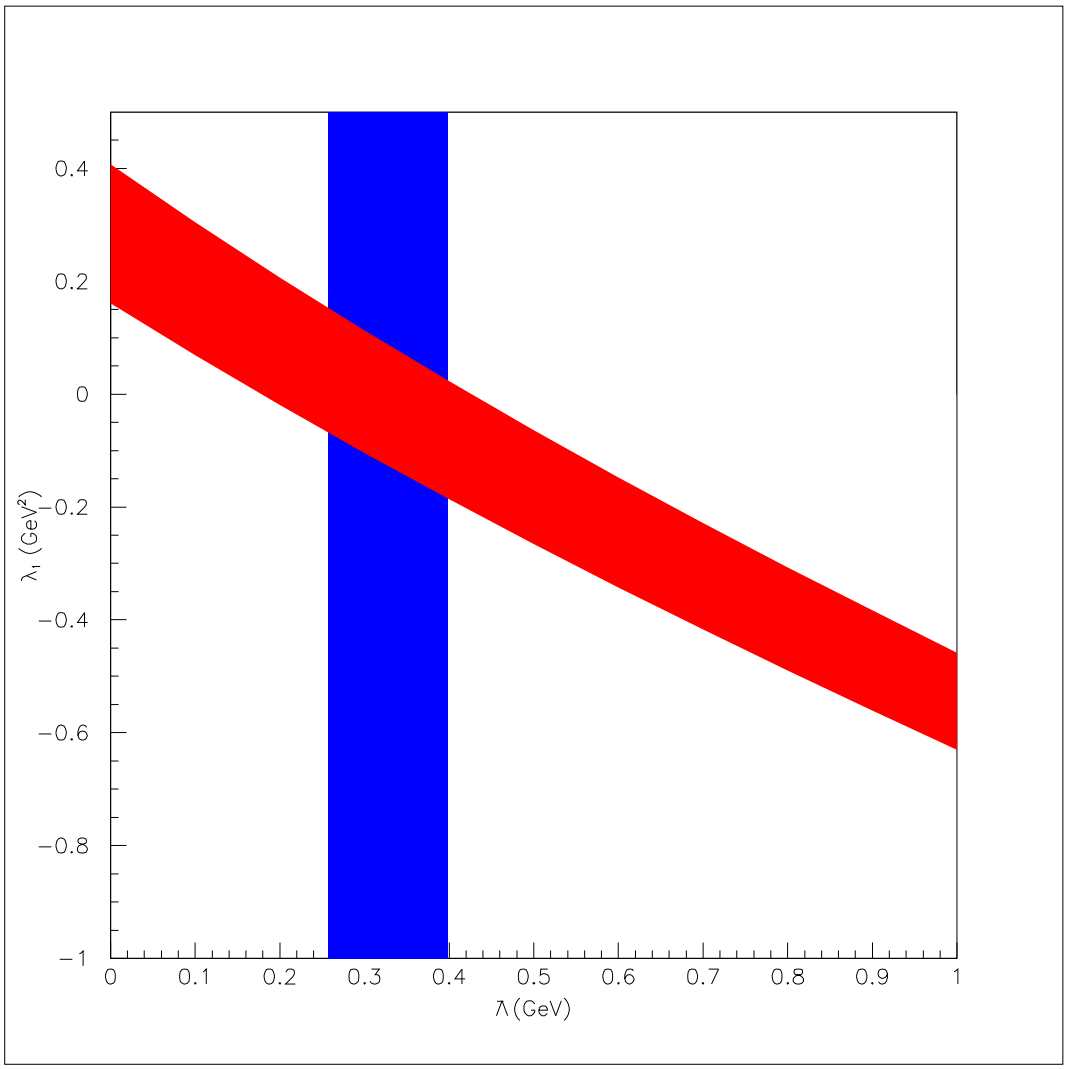

Figure 8.5: Bands in the $\overline{\Lambda} - \lambda_1$ plane for $\langle E_\gamma \rangle_{2.0}$ (blue) and $\langle E_\ell \rangle_{0.7}$ (red). Widths of bands represent measurement uncertainty on the moments.

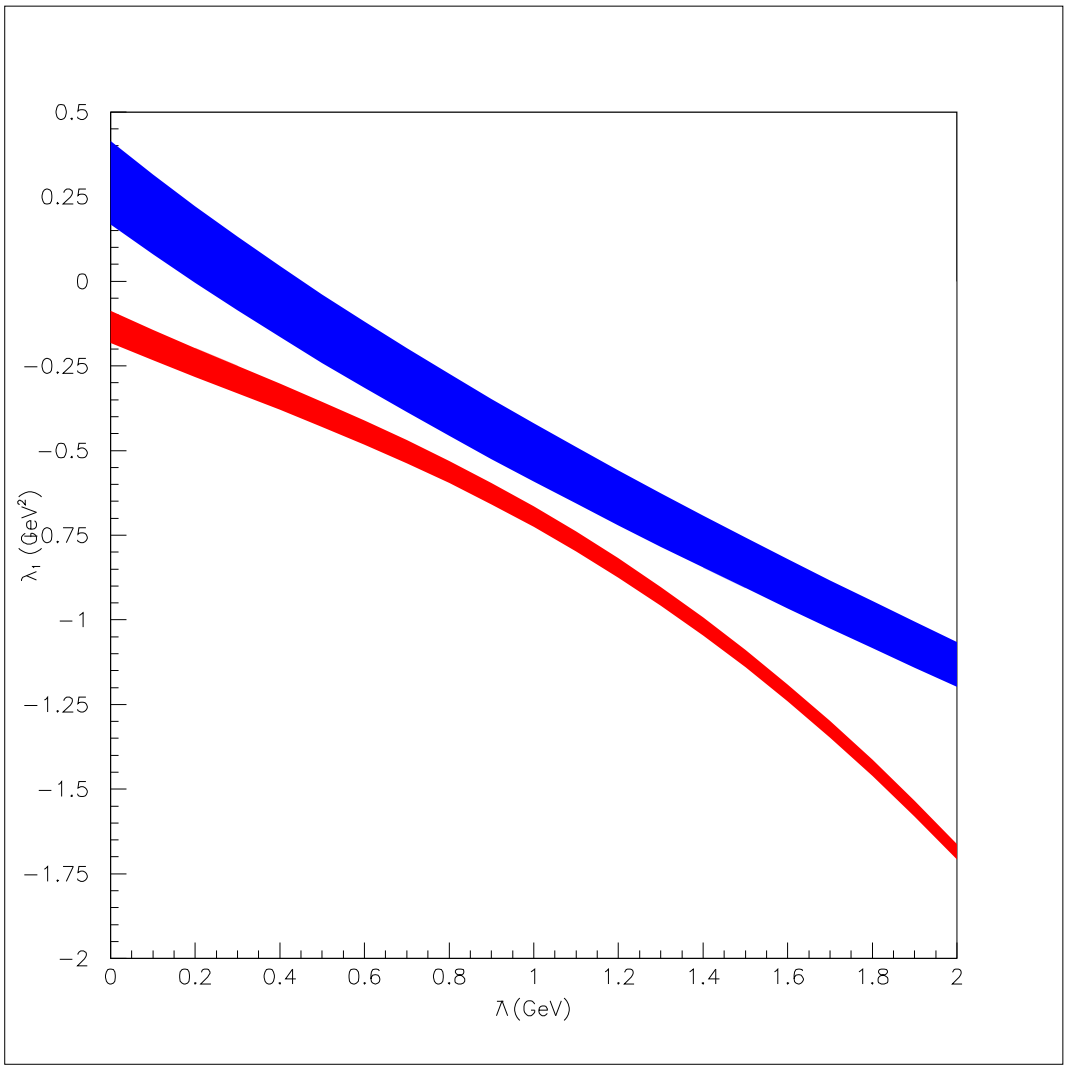

Figure 8.6: Bands in the $\overline{\Lambda} - \lambda_1$ plane for $\langle E_\ell \rangle_{0.7}$ (blue) and $\langle (E_\ell - \langle E_\ell \rangle)^2 \rangle_{0.7}$ (red). Widths of bands represent measurement uncertainty on the moments.

meaningful solutions for $\overline{\Lambda}$ and λ_1, raising serious concerns about the applicability of HQET/OPE, at least as formulated by Bauer *et al.*

8.2.2 Results in the Uraltsev Formulation

The Uraltsev formulation [19] uses different nomenclature for the HQET expansion parameters. Rather than $\overline{\Lambda}$, the quark masses m_b and m_c are used. In place of λ_1 and λ_2 are the μ_π^2 and μ_g^2 first introduced in Chap. 2. By invoking only the heavy-quark parameters relevant to inclusive decay rates, the number of third-order parameters is reduced from six to two: ρ_D^3 and ρ_{LS}^3. These parameters are related to the Bauer formulation parameters by the following relations, valid up to $\mathcal{O}(\alpha_s)$ [58]:

$$\mu_\pi^2 = -\lambda_1 - \frac{\mathcal{T}_1 + 3\mathcal{T}_3}{m_b}; \tag{8.7}$$

$$\mu_g^2 = 3\lambda_2 + \frac{\mathcal{T}_3 + 3\mathcal{T}_4}{m_b}; \tag{8.8}$$

$$\rho_D^3 = \rho_1; \tag{8.9}$$

$$\rho_{LS}^3 = 3\rho_2. \tag{8.10}$$

Similar to the Bauer formulation, the parameters μ_g^2 and ρ_{LS}^3 are constrained by meson mass splittings. For the fits that follow, we use $\mu_g^2 = (0.35 \pm 0.07)$ GeV^2 and $\rho_{LS}^3 = (-0.15 \pm 0.045)$ GeV^3, as suggested in Ref. [19].

Moments for the lepton-energy and hadronic-mass-squared distributions in the

Uraltsev formulation are related to these expansion parameters by the expression [19]

$$\begin{aligned}\mathcal{M} &= V + B(m_b - 4.6\ \text{GeV}) + C(m_c - 1.2\ \text{GeV}) \\ &+ P(\mu_\pi^2 - 0.4\ \text{GeV}^2) + D(\tilde{\rho}_D^3 - 0.1\ \text{GeV}^3) \\ &+ G(\mu_g^2 - 0.35\ \text{GeV}^2) + L(\rho_{LS}^3 + 0.15\ \text{GeV}^3) + S(\alpha_s - 0.22),\end{aligned} \tag{8.11}$$

where the coefficients V, B, C, P, D, G, L, and S have been calculated for various minimum lepton-energy cuts and presented in tables in Ref. [19]. They have also been obtained as FORTRAN functions from the authors. The new parameter $\tilde{\rho}_D^3$ is related to ρ_D^3 by $\tilde{\rho}_D^3 \simeq \rho_D^3 - 0.1$ GeV^3. Expressions for the photon-energy moments were not available at the time of this writing.

The plot in Fig. 8.7 show our measured values of $\langle E_\ell \rangle$ as a function of the minimum lepton energy cut and the HQET/OPE predictions for the lepton-energy moments in the Uraltsev formulation. To make these plots, we need assumptions about m_c and $\tilde{\rho}_D^3$. For the rest of this section, we will use $m_c = (1.2 \pm 0.02)$ GeV, $\tilde{\rho}_D^3 = (0.1 \pm 0.03)$ GeV^3. We will also use $\alpha_s = 0.22 \pm 0.07$.

$|V_{cb}|$ in the Uraltsev Formulation

With the assumptions about m_c and $\tilde{\rho}_D^3$ given above, we can obtain bands in the space of m_b and μ_π^2. The parameters μ_g^2 and ρ_{LS}^3 are set to their previously defined values. Fig. 8.8 shows the bands given by $\langle E_\ell \rangle$ and $\langle (E_\ell - \langle E_\ell \rangle)^2 \rangle$ for lepton-energy cuts $E_{min} = 0.6$, 0.9, 1.2, and 1.5 GeV. As in Sect. 8.2.1, the width of each bands represents only the measurement uncertainty for the moment defining that band; uncertainties in the other expansion parameters will be determined in the calculation

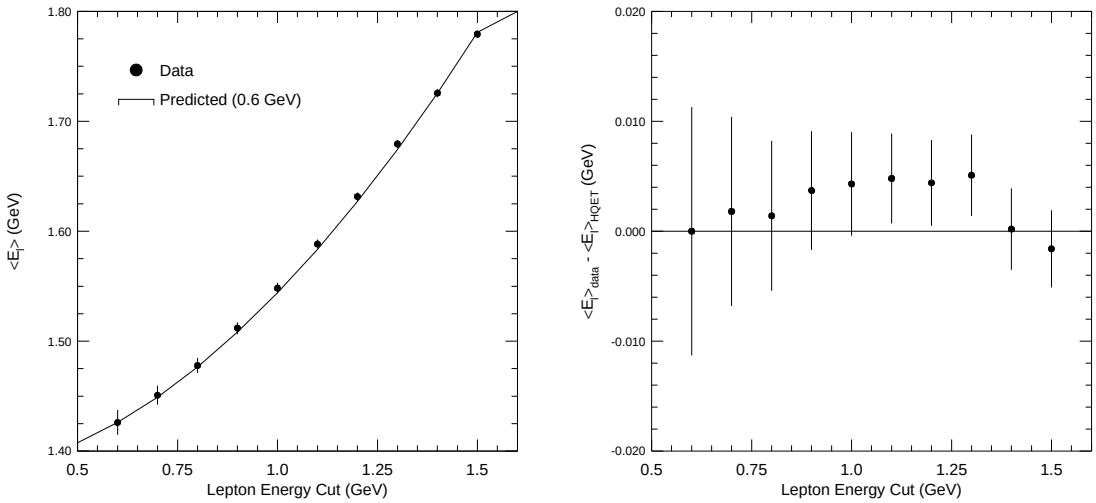

Figure 8.7: **Left:** $\langle E_\ell \rangle$ as a function of E_{min}. The points are data and the line is the prediction in the Uraltsev formulation. **Right:** $\langle E_\ell \rangle^{data} - \langle E_\ell \rangle^{HQET}$ as a function of E_{min}. The points are the data with the predicted moment subtracted. Inputs for these plots were set by $\langle E_\ell \rangle_{0.6}$ and $\langle (E_\ell - \langle E_\ell \rangle)^2 \rangle_{0.6}$. The error bars on the points in both plots represent the measurement uncertainty of the moments.

of $|V_{cb}|$ only.

In the Uraltsev formulation, $|V_{cb}|$ is given by

$$\begin{aligned}\frac{|V_{cb}|}{0.0417} &= \left(\frac{\mathcal{B}_{SL}}{0.105}\right)^{1/2}\left(\frac{1.55\text{ ps}}{\tau_b}\right)^{1/2} \\ &\times(1-4.8\,[\mathcal{B}(B\to X_u\ell\nu)-0.0018])\cdot[1+0.3(\alpha_s(m_b)-0.22)] \\ &\times[1-0.66\,(m_b-4.6\text{ GeV})+0.39\,(m_c-1.15\text{ GeV}) \\ &\quad +0.013\,(\mu_\pi^2-0.4\text{ GeV}^2)+0.09\,(\rho_D^3-\text{ GeV}^3) \\ &\quad +0.05\,(\mu_g^2-0.35\text{ GeV}^2)-0.01\,(\rho_{LS}^3-\text{ GeV}^3)].\end{aligned} \tag{8.12}$$

The values for m_b and μ_π^2 from the bands in Fig. 8.8 are given in Table 8.1, as well as each corresponding $|V_{cb}|$ calculated from Eq. 8.12. As can be seen from Table 8.1,

E_{min} (GeV)	m_b (GeV)	μ_π^2 (GeV^2)	$\lvert V_{cb}\rvert \times 10^2$
0.6	4.583 ± 0.038	0.769 ± 0.092	$4.32 \pm 0.08 \pm 0.11 \pm 0.16$
0.9	4.608 ± 0.021	0.648 ± 0.048	$4.25 \pm 0.08 \pm 0.06 \pm 0.15$
1.2	4.636 ± 0.018	0.539 ± 0.034	$4.16 \pm 0.08 \pm 0.05 \pm 0.15$
1.5	4.666 ± 0.020	0.456 ± 0.029	$4.08 \pm 0.07 \pm 0.05 \pm 0.15$

Table 8.1: Solutions for m_b, μ_π^2, and $|V_{cb}|$ in the Uraltsev formulation from $\langle E_\ell\rangle$ and $\langle(E_\ell-\langle E_\ell\rangle)^2\rangle$ with various lepton-energy cuts. The first quoted error on $|V_{cb}|$ is from the measurement uncertainties of $\mathcal{B}_{SL}$ and τ_B, the second is from the measurement uncertainties of the moments, and the third is from uncertainties in $m_c, \mu_g^2, \rho_D^3, \rho_{LS}^3$, and α_s.

over the range of lepton-energy cuts m_b varies by about 2σ and μ_π^2 varies by about 4σ, while $|V_{cb}|$ is more consistent, varying within a bit more than 1σ.

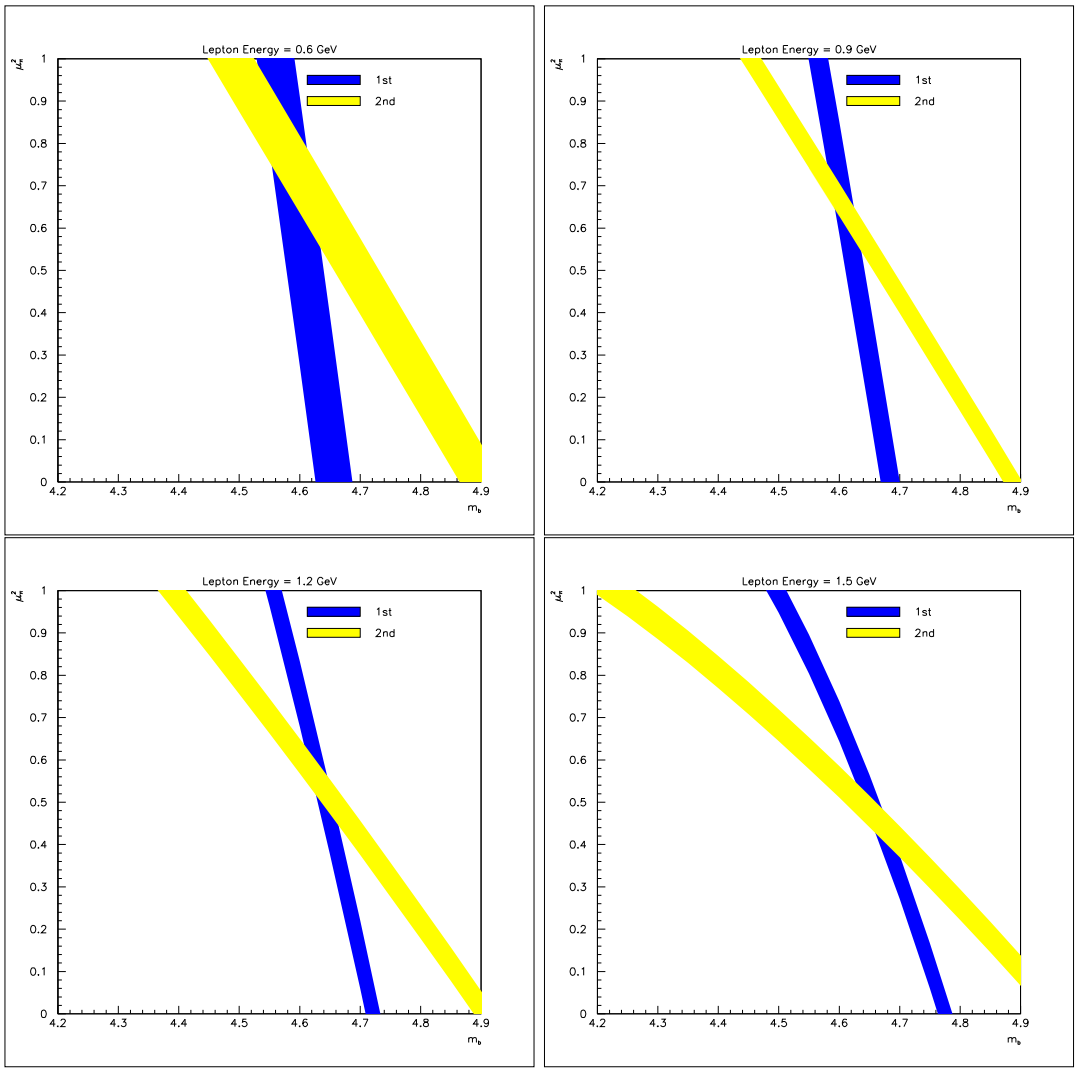

Figure 8.8: Bands in $m_b - \mu_\pi^2$ space of the Uraltsev formulation determined by $\langle E_\ell \rangle$ (blue) and $\langle (E_\ell - \langle E_\ell \rangle)^2 \rangle$ (yellow) with lepton-energy cuts of 0.6, 0.9, 1.2, and 1.5 GeV, as indicated by the title of each plot. The width of each band represents the measurement uncertainty of the moment.

while the expansion parameter μ_π^2 varies considerably, the extracted values for m_b and $|V_{cb}|$ remain fairly consistent.

8.3 Conclusion

The the recent measurements of the branching fraction from this and other experiments [49, 50] have led to an increase in the world average relative to its value a few years ago, reducing the discrepancy between data and theory from about 20% to about 11%. While still in disagreement with theory, it is becoming increasingly probable that the discrepancy will be resolved within the current theoretical framework of QCD.

As mentioned before, the non-perturbative expansion parameters have no literal physical meaning, and their values can be different for different formulations of HQET. However, in a sensible theory they should be *internally* consistent; different combinations of moments should yield similar values of these parameters.

A picture of relative consistency appears if we restrict ourselves to only looking at moments measurements with high minimum-energy cuts in the Bauer formulation [56, 14]. But when using such moments, one should proceed with caution. As the minimum-energy cuts rise, so too does the danger that an insufficient fraction of phase space is being probed to satisfy the quark-hadron duality assumption. If we are to believe that the consistency presented by the high energy-cut moments is real and quark-hadron duality is not in peril with these measurements, it is reasonable to expect the picture will *remain* consistent if we use moments with lower energy

cuts. What has arisen, however, is quite the opposite. Whereas combination of the moments $\langle E_\gamma \rangle_{2.0}$, $\langle M_X^2 - \bar{M}_D^2 \rangle_{1.5}$, and $\langle E_\ell \rangle_{1.5}$ all give solutions consistent with each other, the combination of $\langle E_\gamma \rangle_{2.0}$ and $\langle E_\ell \rangle_{0.7}$ gives a value for λ_1 that is different by about 2.5σ (if uncertainties on the $(\Lambda_{QCD}/M_B)^3$ and perturbative corrections are included). One could say that this is not so bad, since the values of $|V_{cb}|$ one obtains with these disparate λ_1's still are well within errors, but the situation seems to fall apart if one tries to use the combination of two moments that have the smallest chance of trouble with quark-hadron duality, $\langle E_\ell \rangle_{0.7}$ and $\langle (E_\ell - \langle E_\ell \rangle)^2 \rangle_{0.7}$. In this case, we do not even get a solution! If in desperation we take the "distance of closest approach" of the two bands in Fig. 8.6 as a "solution", we get $\overline{\Lambda} \approx 1.0$ GeV and $\lambda_1 \approx -0.6$ GeV^2, giving a $|V_{cb}| \approx 0.047$, values far away from those given by the high energy-cut moments.

The Uraltsev formulation appears to give a more consistent representation of HQET; while internal consistency still seems to be an issue, as it was with the Bauer interpretation, we can obtain reasonable solutions for $\langle E_\ell \rangle$ and $\langle (E_\ell - \langle E_\ell \rangle)^2 \rangle$ for all of our energy cuts, and the determined values of $|V_{cb}|$ are all within errors. We note here that the authors of Ref. [19] have expressed wariness about the accuracy of theoretical expressions for moments with high lepton-energy cuts; they suggest that one use energy cuts no higher than 1.2 GeV.

There are several possible explanations for the observed inconsistency within the Bauer formulation of HQET between the parameters extracted from our different energy-moment measurements. In light of the sizable disagreement between the PHOTOS and Atwood/Marciano treatments of electroweak radiation, we cannot exclude

an error in this correction that is outside of the quoted systematic uncertainty, although it seems unlikely. Neither does quark-hadron duality appear to be causing this inconsistency, since we run into trouble with our most inclusive moments. More likely is a problem with the specific HQET/OPE implementation or incorrect assumptions about the unknown third-order parameters.

The next step in testing HQET will be to perform a comprehensive fit, including correlations, of all published CLEO moments [17, 14, 56], the electron-energy moments in this thesis, and new measurements of the recoil hadronic mass moments in $B \to X_c \ell \nu$ [16] with minimum lepton-energy cuts $E_{min} \geq 1.0$ GeV. With this rather large pool of moments measurements to draw from, the plan is to place constraints not only on m_b and μ_π^2 (or $\overline{\Lambda}$ and λ_1), but also on the $(\Lambda_{QCD}/M)B)^3$ parameters. By leaving all the non-perturbative parameters free in the fit, one can determine if any of the HQET/OPE formulations, including the different mass schemes presented by Bauer *et al.* [11] and the kinetic mass scheme of Uraltsev *et al.* [19], can accommodate all of the data. We are currently building the machinery to perform this fit, and hope to have results by early summer 2004.

BIBLIOGRAPHY

[1] M. Kobayashi and T. Maskawa. Prog. Theor. Phys. **49**, 652 (1973).

[2] K. Hagiwara et al. (Particle Data Group). Phys. Rev. **D66**, 010001 (2002).

[3] J. Chay, H. Georgi, and B. Grinstein. Phys. Lett. **B247**, 399 (1990).

[4] I. I. Y. Bigi, M. A. Shifman, N. G. Uraltsev, and A. I. Vainshtein. Phys. Rev. Lett. **71**, 496 (1993). `hep-ph/9304225`.

[5] A. V. Manohar and M. B. Wise. Phys. Rev. **D49**, 1310 (1994). `hep-ph/9308246`.

[6] M. B. Voloshin Minnesota Univ. Minneapolis - TPI-MINN-94-18-T (94/05,rec.May) 36 p. and Minnesota Univ. Minneapolis - UMN-TH-94-1257 (94/05,rec.May) 36 p.

[7] A. V. Manohar and M. B. Wise. *Heavy Quark Physics*. Cambridge University Press (2000).

[8] M. Neubert. Phys. Lett. **B389**, 727 (1996). `hep-ph/9608211`.

[9] A. F. Falk (1996). `hep-ph/9610363`.

[10] K. Hagiwara et al. (Particle Data Group). Phys. Rev. **D66**, 010001 (2002).

[11] C. W. Bauer, Z. Ligeti, M. Luke, and A. V. Manohar (2002). `hep-ph/0210027`.

[12] R. A. Briere et al. (CLEO) (2002). `hep-ex/0209024`.

[13] A. H. Mahmood et al. CLEO collaboration, CLEO 04-02, CLNS 04/1860, submitted to Physical Review D.

[14] D. Cronin-Hennessy et al. (CLEO). Phys. Rev. Lett. **87**, 251808 (2001). `hep-ex/0108033`.

[15] B. Aubert et al. (BABAR) (2002). `hep-ex/0207084`.

[16] S. E. Csorna et al. CLEO collaboration, CLEO 04-01, CLNS 04/1859, submitted to Physical Review D.

[17] S. Chen et al. (CLEO). Phys. Rev. Lett. **87**, 251807 (2001). hep-ex/0108032.

[18] P. Koppenburg (Belle) (2004). hep-ex/0403004.

[19] P. Gambino and N. Uraltsev (2004). hep-ph/0401063.

[20] M. Tigner. IEEE Trans. Nucl. Sci. **24**, 1849 (1977).

[21] Y. Kubota et al. (CLEO). Nucl. Instrum. Meth. **A320**, 66 (1992).

[22] T. S. Hill. Nucl. Instrum. Meth. **A418**, 32 (1998).

[23] C. Bebek et al. Nucl. Instrum. Meth. **A302**, 261 (1991).

[24] K. Kinoshita. Nucl. Instrum. Meth. **A276**, 242 (1989).

[25] B. Barish et al. (CLEO). Phys. Rev. Lett. **76**, 1570 (1996).

[26] R. Wang (1994). University of Minnesota Ph.D. Thesis.

[27] J. P. Alexander et al. (CLEO). Phys. Rev. Lett. **86**, 2737 (2001).

[28] D. E. Jaffe et al. (CLEO). Phys. Rev. Lett. **86**, 5000 (2001).

[29] S. Anderson and R. Poling. CBX 01-51.

[30] E. Barberio and Z. Was. Comput. Phys. Commun. **79**, 291 (1994).

[31] T. Meyer. Various CLEO collaboration talks and personal communication.

[32] F. D. Fazio and M. Neubert .

[33] D. Scora and N. Isgur. Phys. Rev. **D52**, 2783 (1995). hep-ph/9503486.

[34] A. Bornheim et al. (CLEO). Phys. Rev. Lett. **88**, 231803 (2002). hep-ex/0202019.

[35] B. Gittleman, C. O'Grady, and M. Sapper. CBX 91-82.

[36] B. Gittelman. CBX 93-115.

[37] D. Cronin-Hennessy and M. Palmer. Various CLEO collaboration talks and personal communication.

[38] B. Heltsley. CBX 93-108.

[39] C. Stepaniak, R. Poling, A. Smith, and K. Gao. CBX 03-28.

[40] G. C. Fox and S. Wolfram. Nucl. Phys. **B149**, 413 (1979).

[41] D. Abbaneo et al. (The LEP Electroweak Working Group). `Report No. CERN-EP/2001-50`.

[42] B. Heltsley. CBX 95-35.

[43] D. Cronin-Hennessy, S. Roberts, and E. Thorndike. CBX 01-01.

[44] J. E. Duboscq et al. (CLEO). Phys. Rev. Lett. **76**, 3898 (1996).

[45] M. Athanas et al. (CLEO). Phys. Rev. Lett. **79**, 2208 (1997). `hep-ex/9705019`.

[46] J. L. Goity and W. Roberts. Phys. Rev. **D51**, 3459 (1995). `hep-ph/9406236`.

[47] V. Boisvert et al. CBX 03-03.

[48] D. Atwood and W. J. Marciano. Phys. Rev. D **D41**, 1736 (1990).

[49] B. Aubert et al. (BABAR). Phys. Rev. **D67**, 031101 (2003). `hep-ex/0208018`.

[50] K. Abe et al. (Belle). Phys. Lett. **B547**, 181 (2002). `hep-ex/0208033`.

[51] H. Albrecht et al. (ARGUS). Phys. Lett. **B318**, 397 (1993).

[52] I. I. Y. Bigi, B. Blok, M. A. Shifman, and A. I. Vainshtein. Phys. Lett. **B323**, 408 (1994). `hep-ph/9311339`.

[53] L. Gibbons et al. (CLEO). Phys. Rev. **D56**, 3783 (1997). `hep-ex/9703006`.

[54] D. E. Groom et al. (Particle Data Group). Eur. Phys. J. **C15**, 1 (2000).

[55] T. E. Coan et al. (CLEO). Phys. Rev. Lett. **80**, 1150 (1998). `hep-ex/9710028`.

[56] A. H. Mahmood et al. Phys. Rev. **D67**, 072001 (2003). `hep-ex/0212051`.

[57] M. Gremm and A. Kapustin. Phys. Rev. **D55**, 6924 (1997). `hep-ph/9603448`.

[58] M. Battaglia et al. ECONF **C0304052**, WG102 (2003). `hep-ph/0210319`.